A Dissertation

entitled

Mechanical Properties of Bio- nanocomposites and Cellular Behavior under Mechanical Stimulation

by

Ashkan Aryaei

Submitted to the Graduate Faculty as partial fulfillment of the requirements for the

Doctor of Philosophy Degree in Mechanical Engineering

_____

Dr. A.Champa Jayasuriya, Committee Chair

_____

Dr. Ahalapitiya H. Jayatissa, Committee Member

_____

Dr. Sorin Cioc, Committee Member

_____

Dr. Matthew Franchetti, Committee Member

_____

Dr. Mehdi Pourazady, Committee Member

_____

Dr. Patricia R. Komuniecki, Dean

College of Graduate Studies

The University of Toledo

May 2014

An Abstract of

Mechanical Properties of Bio- nanocomposites and Cellular Behavior under Mechanical Stimulation

by

Ashkan Aryaei

Submitted to the Graduate Faculty as partial fulfillment of the requirements for the Doctor of Philosophy Degree in Mechanical Engineering

The University of Toledo

May 2014

Bio-nanocomposites have recently attracted much interest in the field of bioengineering due to their exceptional chemical, mechanical and biological properties. On one hand, biopolymers such as chitosan have low mechanical properties which have to be improved by diverse methods in order to utilize them for medical applications. On the other hand, biocompatibility of the final material is critical for tissue engineering. Thus, fabricating and designing bio-nanocomposites with biocompatibility, biodegradability and improved mechanical properties are critical for next generation of implantable bone tissue biomaterials.

Measurement of cell mechanical properties is also a timely and important topic in mechanical and bioengineering viewpoints. Previous studies have indicated there are some differences between healthy and cancerous cells which can be led to diagnosis of cancers.

One of the main purposes of this dissertation is to improve the mechanical properties of chitosan using different methods of fabrication such as formation of cross-linking and addition of nanoparticles and tubes as reinforcement into chitosan matrix. In

this study, Tripolyphosphate was used to cross-link between amino group in chitosan and phosphate groups of tripolyphosphate molecules. Micro- and nano- mechanical measurements showed that cross-linking chitosan would improve elastic modulus in both macro and nano scales. Atomic force microscopy based nanoindentation indicated that cross-linking decreased ductility of samples. In addition, surface morphology and material behavior under the applied loads were explored. A new method of measuring cell mechanical properties was introduced and the elastic modulus of two different cell lines at different cell regions was estimated using Hertz model. This novel method did not require any specific substrate treatment or cell fixation. The elastic modulus was measured at cell nucleus and cytoskeleton parts in human amniotic fluid stem cells and murine osteoblasts.

An attempt was made to improve the mechanical and material properties of chitosan by adding zinc oxide and carbon nanotubes. It was found that certain amount of zinc oxide and carbon nanotube are beneficial for improvement of chitosan mechanical properties. Addition of zinc oxide nanoparticles into chitosan increased sample's elastic modulus and hardness. However, adding a higher percentage of zinc oxide was seen to be harmful for osteoblasts. Moreover, this study demonstrated that carbon nanotubes as reinforcement in chitosan matrix could increase the elastic modulus, mechanical strength and viscosity.

The cell proliferation and attachment on different substrates coated with graphene were also investigation. Graphene was selected for this study because of its superior electrical and mechanical properties. Graphene coated substrates were exposed to

osteoblasts for two time points to investigate the effect of graphene and its substrate on cell proliferation and attachment. Graphene layers fabricated on different substrates by chemical vapor deposition were used. Cell attachment study exhibited that a higher rate of cell attachment on the substrates could be achieved with coating of a nanometer layer of graphene.

In addition, the effect of mechanical stimulation on cell attachment and proliferation was investigated. Oscillatory shear stress was produced using an orbital shaker. Different time points and speeds were applied to understand the cell response. In addition, the effect of time gap between cell seeding and applying shear stress was also explored. It was observed that the time gap and optimum magnitude of shear stress increased the rate of proliferation and attachment of osteoblasts.

To my parents …

Acknowledgement

I would like to express the deepest appreciation to my advisors, Dr. A. Champa Jayasuriya and Dr. Ahalapitiya H. Jayatissa for their continuous support of my Ph.D. study and research, for their patience, motivation, enthusiasm, and immense knowledge. Without their help, I could not have finished this work.

I would also like to thank the rest of my dissertation committee members, Dr. M. Franchetti, Dr. S. Cioc and Dr. M. Pourazady for spending their valuable time to review my dissertation.

I gratefully acknowledge the funding sources that made my Ph.D. work possible. This research was supported by National Science Foundation (NSF, grant numbers 0652024 and 0928440) and the National Institute of Health (NIH, grant numbers R03DE019508 and R01DE023356).

I am grateful for my lab mates and friends in both engineering collage and health science campus for their support and collaboration during my studies. Last but not the least, I would like to thank my parents and my lovely wife for all of their support and encouragement.

Table of Contents

List of Figures

List of Abbreviations

AFM .....Atomic Force Microscope

CS .....Chitosan

EDX .....Energy Dispersive X-ray

FTIR .....Fourier Transform Infrared Spectroscopy

hAFS.....Human Amniotic Fluid Stem

MEM .....Minimum Essential Medium
MWCNT .....Multi-Walled Carbon NanoTube

NP .....Nano particle

OB6.....Murine Osteoblasts

PBS .....Phosphate Buffered Saline
Pen Strep.....Penicillin-Streptomycin

SEM.....Scanning Electron Microscope
SWCNT.....Single-Walled Carbon NanoTube

TPP.....Tripolyphosphate

XRD.....X-Ray Diffraction

ZnO.....Zinc Oxide

List of Symbols

τ.....Maximum shear stress
α .....Tip opening angle
ρ.....Density
f .....Frequency of rotation
p.....Probability
h_{max} .....Maximum indentation depth
h_c .....Contact depth
H_N.....Nanohardness
A_c .....Cross sectional area
S .....Contact stiffness
E .....Elastic modulus
υ.....Poisson ratio
δ.....Indentation depth

Chapter 1

Introduction, Background and Research Motivation

1.1 Biomaterials and nanocomposites

Thousands of surgical procedures are performed every day to replace or repair tissue that has been damaged through disease or trauma. The developing field of tissue engineering aims to regenerate damaged tissues by combining cells from the body with highly porous scaffold biomaterials usually associated with some growth factors, which act as templates for tissue regeneration, to guide the growth of new tissue[1]. (Figure 1-1).

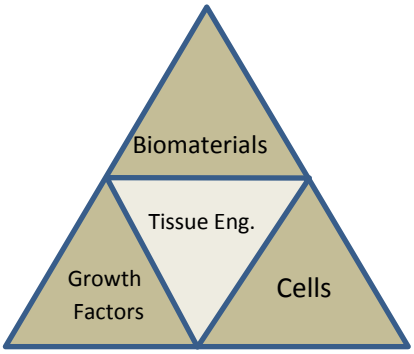

Figure 1-1: Tissue engineering triangle consists of biomaterials, growth factors and cell.

Treatment typically focuses on transplanting tissue from one site to another in the same patient (an autograft) or from one individual to another (a transplant or allograft). While these treatments have been revolutionary and lifesaving, major problems exist with both techniques. Harvesting autografts is expensive, painful, constrained by anatomical limitations and associated with donor site morbidity due to infection and hematoma. Similarly, allografts and transplants also have serious constraints due to problems with accessing enough tissue for all of the patients who require them and the fact that there are risks of rejection by the patient's immune system and the possibility of introducing infection or disease from the donor to the patient. Alternatively, the field of tissue engineering aims to regenerate damaged tissues, instead of replacing them, by developing biological substitutes that restore, maintain or improve tissue function [2].

The field of tissue engineering is highly multidisciplinary and draws on experts from clinical medicine, mechanical engineering, materials science, genetics, and related disciplines from both engineering and the life sciences.

Scaffolds essentially act as a template for tissue formation and are typically seeded with cells and occasionally growth factors, or subjected to biophysical stimuli in the form of a bioreactor; which is a device or system which applies different types of mechanical or chemical stimuli to cells. These cell-seeded scaffolds are either cultured *in vitro* to synthesize tissues which can then be implanted into an injured site, or are implanted directly into the injured site, using the body's own systems, where regeneration of tissues or organs is induced *in vivo*. This combination of cells, signals and scaffold is often referred to as a tissue engineering triad.

Numerous scaffolds produced from a variety of biomaterials and manufactured using a plethora of fabrication techniques have been used in the field in attempts to regenerate different tissues and organs in the body. A number of key considerations such as biocompatibility and mechanical properties have to be investigated. The full desired properties of scaffolds are shown in Figure 1-2.

The very first criterion of any scaffold for tissue engineering is that it must be biocompatible [3]; cells must adhere, function normally and migrate onto the surface and eventually through the scaffold and begin to proliferate before laying down new matrix.

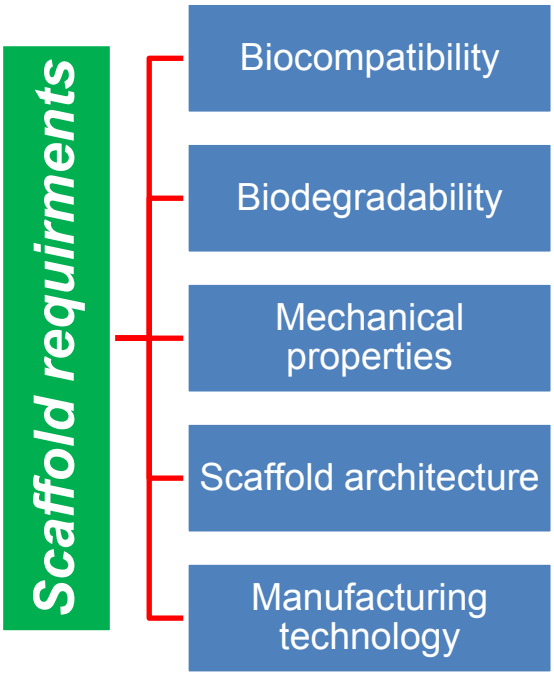

Figure 1-2: Tree diagram of scaffold requirements.

Ideally, the scaffold should have mechanical properties consistent with the anatomical site into which it is to be implanted and, from a practical perspective, it must be strong enough to allow surgical handling during implantation. While this is important in all tissues, it provides some challenges for cardiovascular and orthopedic applications specifically. Producing scaffolds with adequate mechanical properties is one of the great challenges in attempting to engineer bone or cartilage. For these tissues, the implanted scaffold must have sufficient mechanical integrity to function from the time of implantation to the completion of the remodeling process. One of the most useful methods for enhancing polymers mechanical properties is to incorporate nano particles or nanofibers in them. This idea is well developed in other fields of science but it is relatively new in bioengineering and medicine. In addition, by manipulating drugs and other materials at the nanometer scale, the fundamental properties and bioactivity of materials can be altered [4]. These tools can permit control over the characteristics of drugs or agents such as solubility, blood pool retention times, controlled release over short or long durations, environmentally triggered controlled release or highly specific site-targeted delivery. Furthermore, by using nanometer-sized particles, the increased functional surface area per unit volume can be exploited in various ways.

The new tools are not necessarily intuitive and bring with them new challenges and hurdles. Nanometer-sized structures do not behave in the same predictive ways that single, small-molecule interactions occur. Nanoconstructs, especially multifunctional ones, are complex three-dimensional objects with critical dependence on position, size, shape and charge of interrelated components [5]. Although the development of nanoparticles seems to have great potential for several biomedical fields, there has been

only little progress in the attainment of effective results in current human therapy. However, it must be said that the use of nanoparticles also raises the need of a comprehensive understanding of their secondary effects and cytotoxicity once they enter the body. The large surface area of nanoparticles makes them very reactive in the cellular environment. Their dimensions enable them to penetrate through the lungs, skin or intestinal tract and they might deposit in several organs causing adverse biological reactions. Moreover, the fact that these particles are able to penetrate the cell membrane and reach the cell nucleus might raise some concern about possible unknown risks attributed to the particle nature.

The first main part of this study is about the mechanical and cytotoxicity properties of chitosan polymer after cross-linking and adding zinc oxide nanoparticles. Various methods of material characterization and measuring were applied to investigate the properties of new-fabricated films. In the second part of this dissertation, the mechanical properties and behavior of two kinds of cells under the nanoindentation test using Hertz theory will be described.

1.2 Chitin and its derivatives

Chitin, (poly (β-(1-4)-N-acetyl-D-glucosamine)), is a natural polysaccharide of major importance, first identified in 1884. This biopolymer is synthesized by an enormous number of living organisms; considering the amount of chitin produced annually in the world, it is the most abundant polymer after cellulose. Chitin is highly hydrophobic and insoluble in water and most organic solvents. The most important derivative of chitin is

chitosan, obtained by partial deacetylation of chitin in the solid state under alkaline conditions. Figure 1-3 shows the chemical structure of chitin and chitosan.

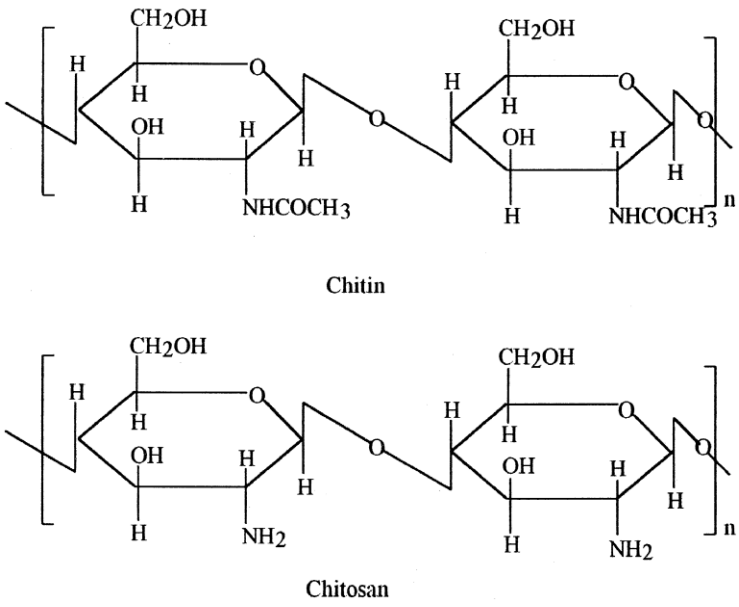

Figure 1-3: Chemical structure of chitin and chitosan [6]

Chitin and chitosan inherently have poor mechanical properties [7]. For instance, its elastic modulus is significantly lower than human bone elastic modulus. Therefore, chitin can be used as bone substitute for bone repair and reconstruction only if its mechanical properties improve.

1.3 Improvement of chitosan mechanical properties by cross-linking

In order to successfully use chitosan in the bone tissue regeneration applications, the mechanical properties of chitosan must be improved. Recently, we have fabricated the

chitosan based microparticles to apply in bone tissue regeneration [8]. The structural integrity of the chitosan microparticles was improved by forming cross-links between the amine groups of the chitosan and phosphate groups of the sodium tripolyphosphate (TPP). TPP was selected to make the cross-links in the microparticles because it is a non-toxic compound. This is preferable to other toxic chemical crosslinkers such as glutaraldehyde [9]. It was difficult to determine the mechanical properties of chitosan based microparticles due to their particle form. To overcome this issue, we fabricated chitosan films using the same chitosan solvents and cross-linking chemistry as the chitosan microparticles prepared previously [10]. Although shape is an important factor that affects the elastic modulus results, here we showed cross-linking can increase the elastic modulus of chitosan in different scales. As a film, we were able to obtain the nano and micro mechanical properties of cross-linked chitosan films and uncross-linked chitosan films. Introducing different types of additives into chitosan films will change the mechanical properties of those films. Wang et al. [11] used montmorillonite nanoparticles to improve the mechanical properties of chitosan including the elastic modulus. Caner et al. [12] ran a comparative study to determine the effects of different acids and plasticizers on the mechanical properties of chitosan films. Creating cross-links between an external material and chitosan can improve the chemical and biological properties of chitosan. However, there are a few studies that show the mechanical properties of cross-linked chitosan films [13]. To the best of our knowledge, there is no comparative study that shows the effects of creating cross-link on micro and nano mechanical properties such as hardness and elastic modulus of chitosan films.

1.4 Cells and the importance of their mechanical properties

The mechanical properties of cells have attracted interest from the very beginning of cell biologic studies. The mechanical properties of cells are closely related to their behavior and function and are largely determined by the cytoskeleton. Disease not only causes biological and functional alterations but also results in abnormalities in the physical and structural characteristics of cells. Cell mechanical properties and cell adhesion are important issues in cancer research, especially in metastasis. To form a metastatic tumor, a cancerous cell detaches from the primary tumor, moves to another location in the body and there continues to proliferate to form another tumor. Researchers have shown that cancerous cells being softer than healthy cells allow them to cross epithelia and migrate in the body via the cardiovascular or lymphatic system [14, 15]. Modifications in the adhesion properties at the origin of the detachment of the cancerous cell from the tumor are also a critical point.

Indeed, cell mechanical properties have been found to affect substantially several important factors of cell function, such as the shape, deformability, motility, division, and adhesion. Several methods, including magnetic twisting cytometry, laser-tracking microrheology, magnetic tweezers, the optical stretcher, and various cell indenters, have been used for the study of cell mechanical properties in adherent cells. Depending on the cell type and the method of measuring, the resistance of single cells to elastic deformation, as quantified by an effective elastic modulus ranges from 10^2 to 10^5 Pa (Figure 1-4).

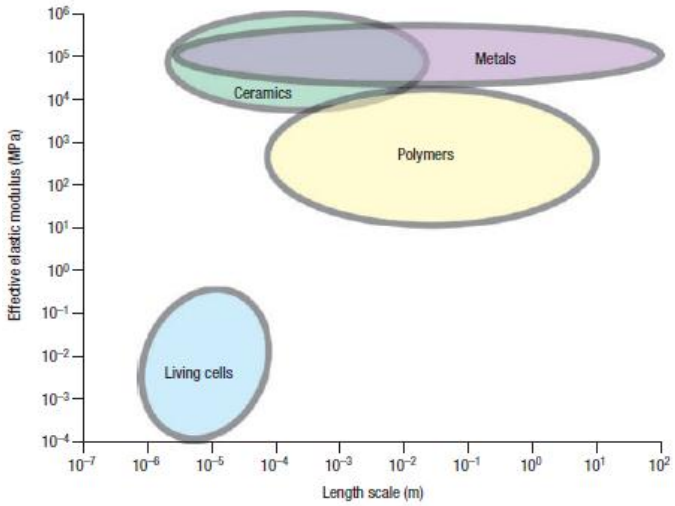

Figure 1-4: Approximate range of values for the elastic modulus of biological cells [16]

It is known that the mechanical properties of individual cells can determine the structural integrity of whole tissues arising from the mechanical interactions between cells and the surrounding extracellular matrix (ECM). On the other hand, mechanical loads exerted at the tissue level are transmitted to individual cells and can influence their physiological functions.

The most popular method of measuring cell mechanical properties is Atomic Force Microscopy (AFM). This instrument was first described in 1986 and became commercially available in 1989.

AFM can provide three-dimensional images of surface topography of biological specimens in ambient liquid or gas environments. Unlike other techniques, AFM can use samples with just minor preparation, e.g. staining, coating etc., over a large range of temperatures and in repetitive studies [17, 18]. The high resolution (in the nanometer range) allows topographical imaging of samples such as DNA molecules, protein

adsorption or crystal growth, and living cells adsorbed on biomaterials. In addition to topographical measurements, AFM is also capable of complementary techniques that provide information on other surface properties, e.g. stiffness, hardness, friction, or elasticity [19].

The key element of the AFM is the cantilever (Figure 1-5). It consists of one or more beams of silicon or silicon nitride of 100–500 μm in length and 0.5–5 μm in thickness. At the end of the cantilever, a sharp tip is mounted to sense the force between the sample and tip. For normal topographic imaging, the tip is brought into continuous or intermittent contact with the sample as it raster scans over the surface. An optical system is then used to measure the changes of the laser beam reflected from the gold-coated back of the cantilever onto a position-sensitive photodiode, which can measure changes in the position of the incident laser as small as 1 nm. The instrument is available in several operating modes that can be chosen depending on the sample, environment, and measurement requirements.

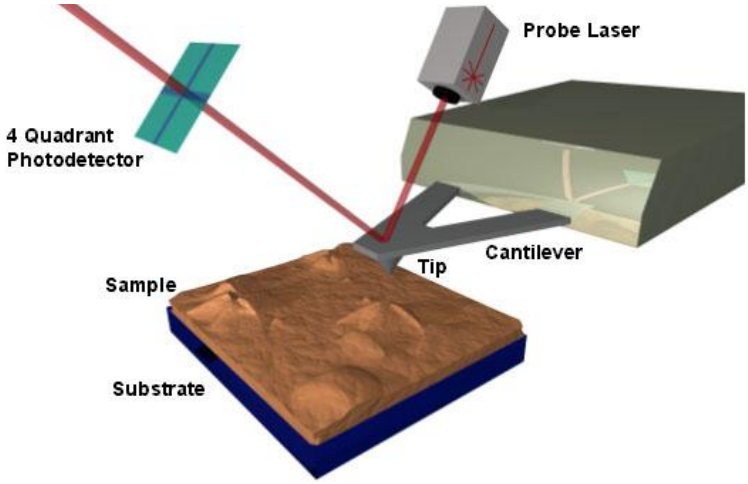

Figure 1-5: A schematic configuration of AFM.

Basically, an AFM works in two modes. Although both primary forms of AFM imaging, i.e. tapping and contact mode, have been used in cell elastography, contact mode is easier and more convenient to use in compare to tapping mode, as long as it is more conducive to switching back and forth between imaging and "force mode" in which nanoindentation is used to obtain quantitative stiffness measurements, while it can also give high-resolution images with cell viability sustained for several hours [20].

Nevertheless, as one powerful method of questioning, the future holds tremendous potential for AFM elastography of living cells to provide novel biomechanical markers that will enhance the detection, diagnosis, and treatment of disease.

1.5 Zinc oxide/ chitosan nanocomposite

As stated earlier, improving mechanical properties of chitosan is one of the current major goals in biomedical engineering. As of now, different additives were tried to enhance the mechanical, cell attachment and anti-bacterial effects of chitosan and its derivatives. One idea is to add biocompatible nanoparticles to reach this goal.

Zinc oxide (ZnO) nanostructures have a wide range of applications in the rubber, sensor and cosmetic industries [21]. Recent studies focused on potential applications of nano-scale ZnO incorporated in biopolymers to use as bandages for wound dressing and treat various human diseases such as cancer. Biodegradation of ZnO in the body releases Zn^{2+} cations (daily requirement for humans) and O^{2-} anions [22]. ZnO nanoparticles (NPs) also exhibit antibacterial activity. Bacterial contamination is frequently present in traumatic wounds and bone defects, including combat injuries [23]. Therefore, antibacterial activity of the material is a crucial factor in treating bone defects and other

types of bacterial infection related diseases. According to the published results, nano-sized ZnO is a more effective antimicrobial agent than bulk ZnO [24].

Various investigations have introduced toxic effects of pure ZnO in diverse forms such as nanoparticles and nanowires [25, 26]. The appearance and extent of nanostructures ZnO cytotoxicity play an important role in the application of ZnO NPs in the treatment of human diseases. While some studies have shown severe cytotoxicity of ZnO nanostructures, other studies have not claimed remarkable cell toxic effect because of changes in cell density or amount of ZnO NPs [27]. Consequently, in order to use ZnO nanostructures in tissue engineering and regenerative medicine, these nanostructures need to be incorporated with a carrier polymer or other type of material. On the other hand, numerous studies have reported that the mechanical and electrical properties of different polymers have improved when ZnO nanoparticles are incorporated into the polymeric matrices [28].

At neutral pH, chitosan showed antibacterial activity but in order to import higher antibacterial effect, one way is to incorporate ZnO NP into it. In addition, the complete investigation on the effects of ZnO NPs incorporated into chitosan films has not yet been done and it is essential to examine further the toxicity of ZnO under the actual environmental conditions.

In the first part of this dissertation, we improved the mechanical properties of chitosan biopolymer by two methods: 1- Chitosan was cross-linked with TPP and micro and nano mechanical properties was measured and compared with pure chitosan film. 2- Chitosan/zinc oxide and chitosan/carbon nanotube nanocomposites with different percentages of ZnO and CNT were fabricated and complete material characterization was

performed. Finally, the effect of ZnO nanoparticles and CNT on mechanical properties and cytotoxicity of chitosan films were evaluated.

In the next part of this dissertation, the mechanical properties of live cells were measured using nanoindentation.

In the last chapter, the effect of mechanical stimulation on osteoblast attachment and proliferation was investigated.

Statistical analysis was also done in most of the experiments to study the significant differences between selected groups. One-way analysis of variance (ANOVA) method was utilized by using SPSS and Excel softwares.

Chapter 2

Effect of Cross-linking in Micro and Nano Mechanical Properties of Chitosan

2.1 Abstract

The aim of this study was to determine the nano and micro mechanical properties for uncross-linked and cross-linked chitosan films. Specifically, we looked at nanoindentation hardness, microhardness, and elastic modulus. It is important to study the nano and micro scale mechanical properties of chitosan since chitosan has been widely used for biomedical applications. Using the solvent-cast method, the chitosan films were prepared at room temperature on the cleaned glass plates. The chitosan solution was prepared by dissolving chitosan in acetic acid 1% (v/v). Tripolyphosphate (TPP) was used to create the cross-links between amine groups in chitosan and phosphate groups in TPP. In this study, AFM was used to measure the nanoindentation hardness and surface topography of the uncross-linked and cross-linked chitosan films. Elastic modulus was then calculated from the nanoindentation results. The effective elastic modulus was determined by microhardness with some modifications to previous theories.

The microhardeness of the chitosan films was measured using Vicker's hardness meter under three different loads. Our results showed that the microhardness and elastic modulus for cross-linked chitosan films were higher than to the uncross-linked films. However, the cross-linked chitosan films showed increased brittleness when compared to uncross-linked films. By increasing the load magnitude, the microhardness was increased for both uncross-linked and cross-linked chitosan films.

2.2 Introduction

For several decades, chitosan has been extensively investigated for diverse applications; molecular separation, food packaging film, artificial skin, bone substitutes, and water engineering. Chitosan has become a popular material due to its relatively good mechanical properties, biocompatibility, biodegradability, multi-functional groups, and its solubility in aqueous medium [29]. Recently, chitosan research for biomedical applications has increased dramatically, specifically in the areas of bone and cartilage tissue engineering [30-32]. Tissue engineering applications have explored chitosan's many solid forms: flakes, powder, films, fibers, spongers and microparticles [33, 34].

Creating cross-links between an external material and chitosan can improve the chemical and biological properties of chitosan [35-37]. However, there are a few studies that show the mechanical properties of cross-linked chitosan films [13]. To the best of the author's knowledge, there is no comparative study that shows the effects of creating cross-link on micro and nano mechanical properties such as hardness and elastic modulus of chitosan films. Based on this understanding, hardness and elastic modulus of uncross-

linked and cross-linked chitosan films were investigated by nanoindentation and Vicker's hardness meter. First, nanohardness of uncross-linked and cross-linked chitosan films was measured. Next, based on the load-tip's deflection graph, elastic modulus was calculated [38]. Finally, after determining the microhardness for both cross-linked and uncross-linked chitosan films, a modified method was used to find the elastic modulus of chitosan films.

2.3 Materials and methods

2.3.1 Materials

Chitosan (85% deacetylated, medium molecular weight), acetic acid and TPP used to fabricate the thin films were purchased from Sigma-Aldrich. Thin glass plates (1 mm thick, FisherBrand) were used to make the chitosan thin films.

2.3.2 Chitosan film fabrication

2.3.2.1 Uncross-linked chitosan films

Chitosan (2% w/v) solution was prepared by adding 200 mg of chitosan to 10 ml of acetic acid 1% (v/v). The solution was stirred for 1 hour to get a homogeneous mixture and cast at room temperature into the clean glass plates purified with acetone. The films were dried over night to evaporate any trace of solvents, allowing us to obtain the uncross-linked thin films.

2.3.2.2 Cross-linked chitosan films

To obtain the cross-linked chitosan films, 80% (w/w) TPP solution was prepared by dissolving 1.6 gr of TPP in 100 ml of deionized water. The glass plate casted with the chitosan thin film was then placed in a container filled with TPP solution immediately after adding chitosan solution to the glass plate and covered. After 30 min of stirring the mixture, the glass plate was dried over night at room temperature.

2.3.3 Nanoindentation, nanohardness measurement and theory

Atomic Force Microscope (Veeco multimode with nano scope V controller) was used to find nanohardness and material behavior under loading and unloading conditions during the nanoindentation test. To obtain the best results, a J scanner was installed on AFM. Nano-indentation measurement was performed by using a diamond tip with spring constant of 216.8 N/m. The applied load was approximately 20,000 nN. To ensure accurate results, the test was performed 30 times for each case.

Currently, there is a common method used to find elastic modulus from nanoindentation [39, 40]. The key quantities to determine the mechanical properties from loading-unloading curve are defined as follows [38]. The maximum indentation depth $h_{\max}$ includes elastic and plastic deformation. The depth at which the applied force becomes zero on unloading is called h_f the depth h_c is the contact depth at which the cross section area A_c is taken to calculate hardness and indentation modulus. The nanohardness of the sample (H_N) is determined using the formula:

$$H_N = \frac{F_{\max}}{A_c(h_c)}, \tag{1}$$

where $F_{\max}$ is the maximum applied load and A_c is the cross sectional area corresponding to the depth h_c. The determination of the contact depth h_c is given by:

$$h_c = h_{\max} - 0.75\frac{F_{\max}}{S}, \tag{2}$$

where S is the contact stiffness:

$$S = \frac{dF}{dh}, \tag{3}$$

with $\frac{dF}{dh}$ being the slope of the unloading curve at the initial point of unloading. The reduced Young's indentation modulus E_r is a measure of the elastic properties of the tip sample system and can be calculated from the load-depth curves according to the formula:

$$E_r = \frac{1}{2}\sqrt{\frac{\pi}{A_c}}S \tag{4}$$

For elastically deformable indenters, the reduced modulus E_r can be generalized and is defined as:

$$\frac{1}{E_r} = \frac{1-\upsilon_s^2}{E_s} + \frac{1-\upsilon_t^2}{E_t}, \tag{5}$$

where E_s and υ_s are the indentation modulus and Poisson ratio of the sample, E_t and υ_t are the indentation modulus and Poisson ratio of the indenter tip. Since E_t is much higher than E_s the value of E_r will hardly differ from E_s.

For indentations in nano scale, the residual area was difficult to be measured with the traditional optical microscopy because of a too low resolution. The area as a function contact depth for a perfect indenter can be obtained as:

$$A_c(h_c) = 24.5h_c^2 \tag{6}$$

2.3.4 Microhardness measurement and theory

According to Vicker's indentor geometry (Figure 2-1), the indent's diagonal length can be obtained as:

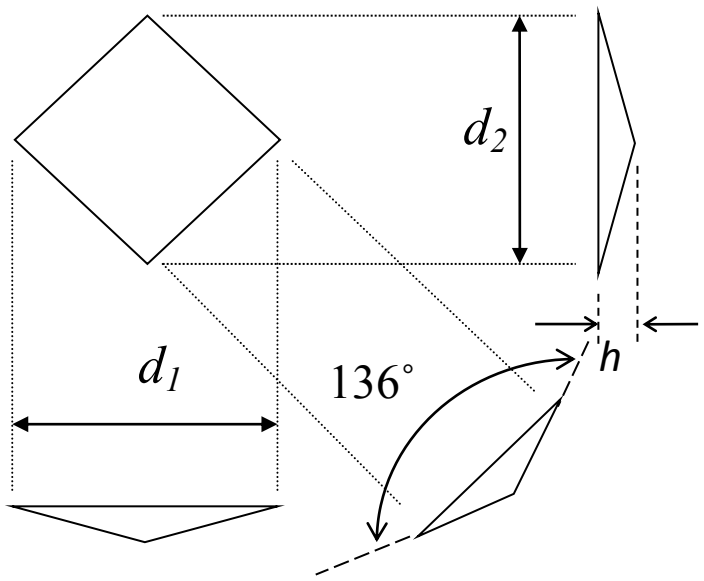

Figure 2-1: Geometry of Vicker's indent on surface

$$d = \sqrt{\frac{1.854F}{HV}}, \tag{7}$$

where F, HV are applied load and Vicker's hardness number, respectively.

Similarly, the projected area (A) and final depth (h_f) can be simply found as:

$$A = \frac{d^2}{2} \tag{8}$$

$$h_f = \frac{d}{2}\tan(22°) \tag{9}$$

Unfortunately, there was not enough information from microhardness test to find elastic modulus by using approximately similar theory like nanoindentation hardness test. As a result, there should be some assumptions based on the material behavior. First of all, it is necessary to determine S and $h_{\max}$. To find S, we need to find $h_{\max}$. $h_{\max}$ can be obtained by ratio of elastic part of deformation to plastic part of deformation which was obtained from AFM. Based on data from nanoindentation results, which will be presented later, $(h_{\max} - h_f)/h_f$ (the ratio of elastic elongation to plastic elongation) was determined to calculate the microhardness. According to the materials deformation theory, this assumption was applicable because after removing load from the surface only permanent or plastic depth was measured and $h_{\max}$ was the maximum depth (plastic and elastic depth). According to Figure 2-2 and using loading-unloading curves from AFM, S can be approximated as follow:

$$\frac{1}{S} = \frac{(h_{\max} - h_f)/3}{F_{\max}}, \tag{10}$$

where $F_{\max}$ is the applied load for the microhardness test. To determine the elastic modulus from microhardness, the same procedure similar to nanoindentation was applied.

In the presented theory, materials exhibit elasto-plastic behavior and loading curve does not overlap loading curve.

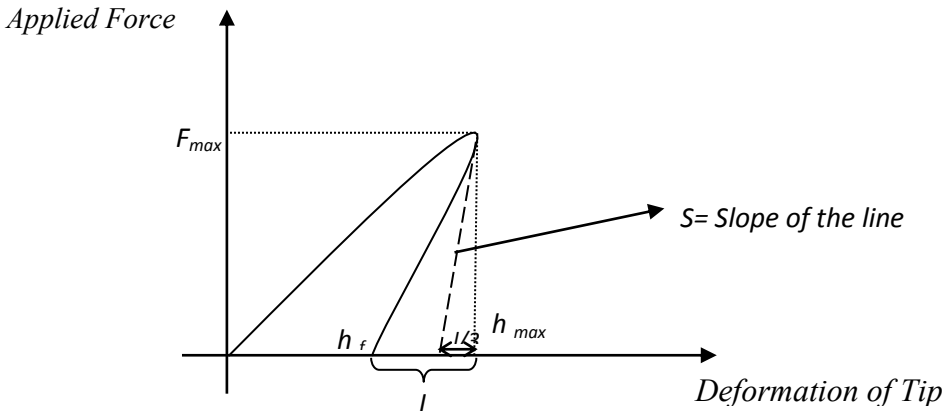

Figure 2-2: Schematic representation of material behavior during loading and unloading which was extended to microhardness tests.

2.4 Results

2.4.1 Nanoindentation hardness and elastic modulus

Capturing images from the different parts of the samples reveal more information about the effect of cross-links on chitosan films. An interesting finding shown in Figure 2-3 was the different surface roughness of the chitosan films. Figure 2-3(a) demonstrates the top view of surface for uncross-linked chitosan thin film. This figure shows the height range about 23 nm and comparatively flat and irregular surface. Conversely, based on Figure 2-3(b), the height range for cross-linked chitosan was approximately 3 μm which was significantly larger in comparison to the uncross-linked chitosan thin film. Figures 2-3(c) and 2-3(d) exhibit a 3D plot of the surface of each type of chitosan films. These topography images showed depressions and elevations on the surface of chitosan film

which was also reported by other researchers [41]. The imaged surfaces show that chitosan film was composed of irregular, bulbous structural elements. However, when dipped in TPP solution, the film became homogeneous, smoother and the bumps disappear.

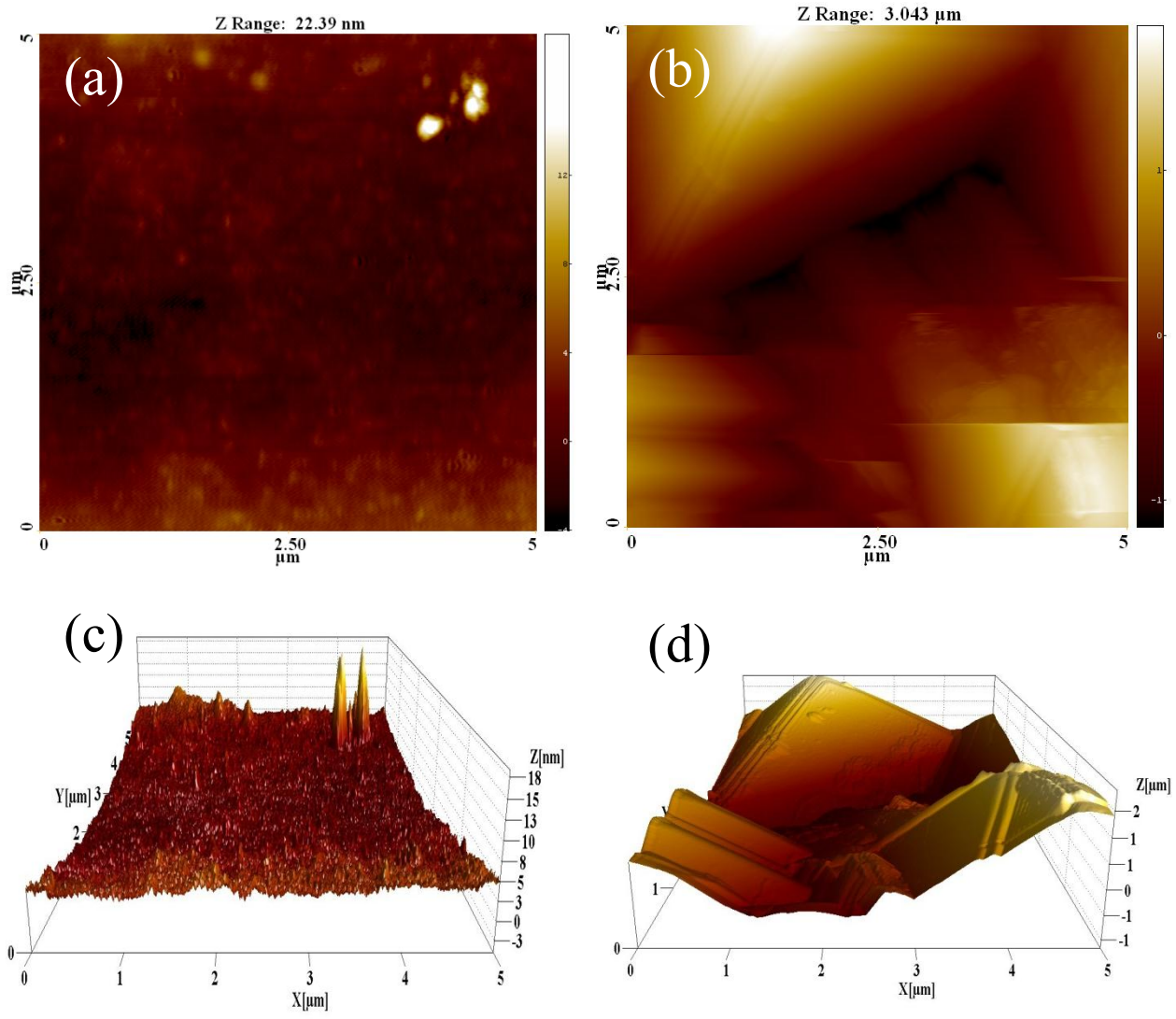

Figure 2-3: (a) AFM image from the surface of samples: uncross-linked chitosan top view, (b) Cross-linked chitosan top view, (c) 3D chitosan image, (d) 3D cross- linked chitosan image.

The nanoindentation test was repeated 30 times for each sample in order to obtain accurate results. Figure 2-4(a) and Figure 2-4(b) shows a top view of the indent effect on uncross-linked chitosan and cross-linked chitosan films, respectively. The distance between each indentation was 450 nm. Additionally, Figure 2-4(c) and Figure 2-4(d) show topological image of the indent on uncross-linked chitosan and cross-linked chitosan films, respectively.

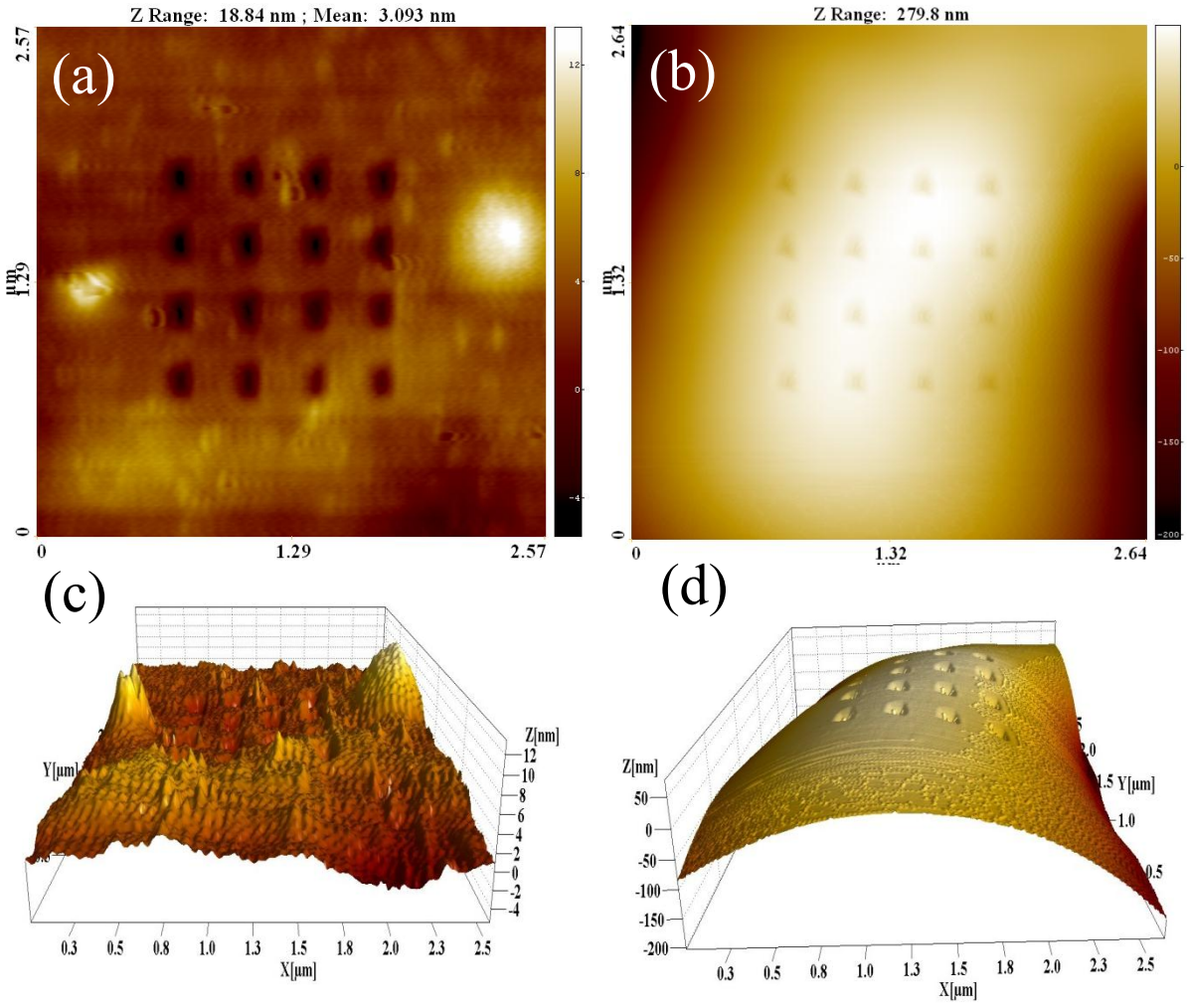

Figure 2-4: AFM image from the surface of samples after nanoindentation test: (a) chitosan top view, (b) cross- linked chitosan top view, (c) 3D chitosan image, (d) 3D Cross-linked chitosan image.

Data obtained from AFM was analyzed by SPIP (Scanning Probe Image Processor) commercial software to generate the specified parameters that were described in theory section. Figure 2-5(a) demonstrates the average hardness number for each case. As expected, the hardness increases for cross-linked chitosan films compared to the uncross-linked chitosan films. Hardness is 1200 MPa and 1550 MPa for uncross-linked chitosan films and cross-linked chitosan films, respectively. Similarly, by calculating the required parameters from the graph obtained by SPIP, average elastic modulus was calculated for both samples, as displayed in Figure 2-5(b). Elastic modulus was about 3.1 MPa and 6.3 MPa for uncross-linked chitosan and cross-linked chitosan, respectively.

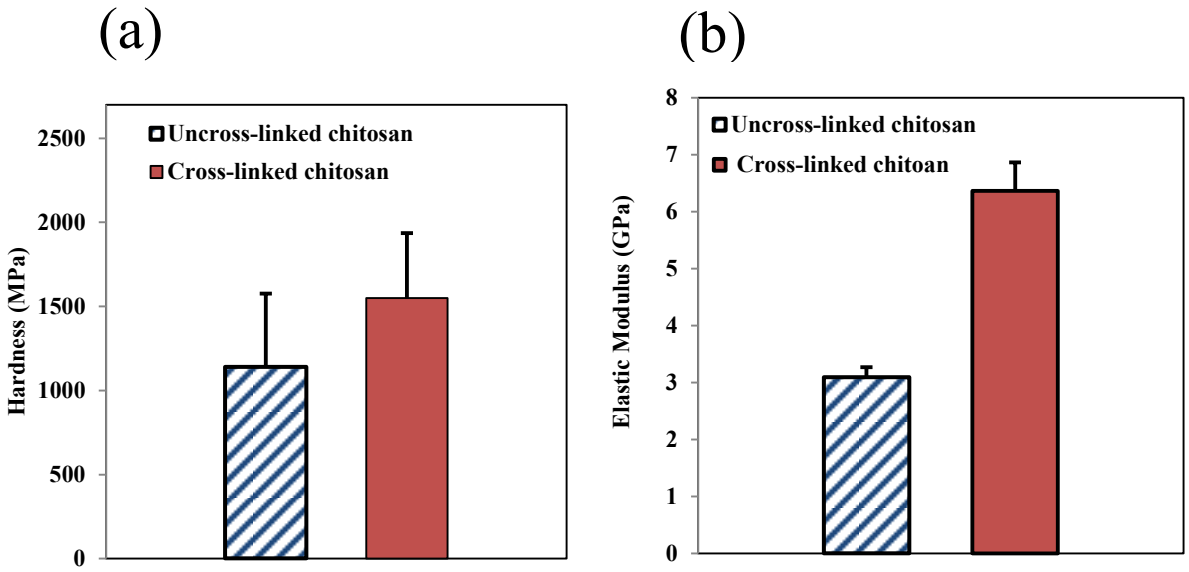

Figure 2-5: (a) Comparison for nanohardness and (b) elastic modulus between uncross-linked chitosan and cross-linked chitosan films.

2.4.2 Microhardness and elastic modulus

The modified theory explained previously was used to determine the deformation of the chitosan films. The deformation of material during the loading was derived for uncross-linked (Figure 2-6(a)) and cross-linked chitosan thin films (Figure 2-6(b)). Figure 2-6 was obtained by determining the ratio of elastic deformation into plastic deformation for uncross-linked chitosan and cross-linked chitosan films. According to nanoindentation results, $(h_{\max} - h_f)/h_f$ for uncross-linked and cross-linked chitosan films were around 2.1 and 1.3, respectively. As stated before, these fractions approximate the ratio of plastic deformation to total deformation. Figure 2-6(a) and Figure 2-6(b) show cross-linked chitosan films decrease in plastic deformation and increase in brittleness, as was observed from the nanoindentation test.

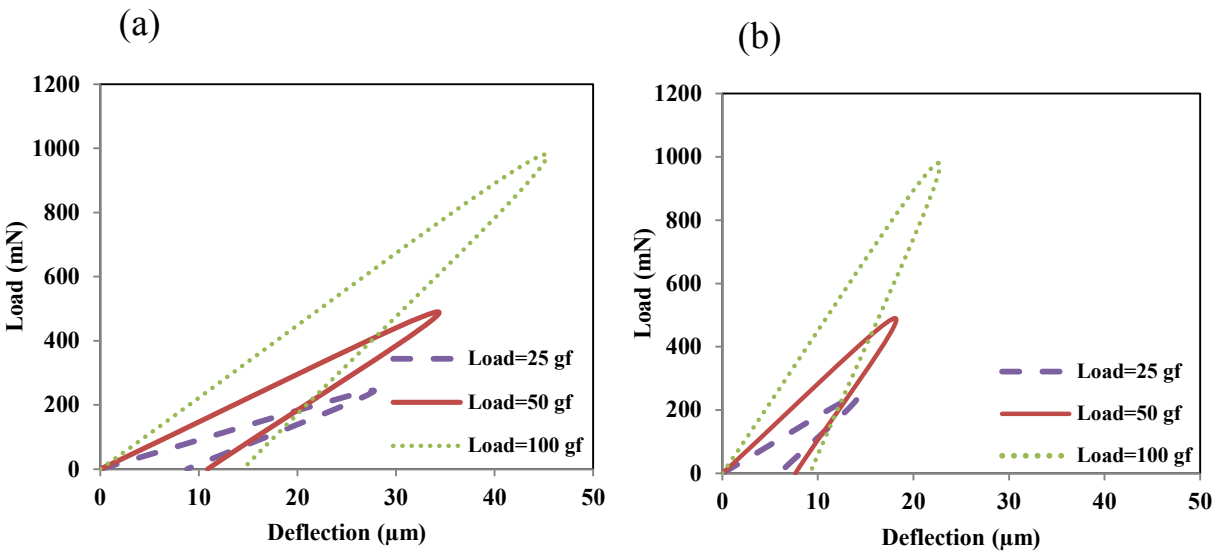

Figure 2-6: Suggested behavior during loading and unloading in microhardness test: (a) chitosan film and (b) cross-linked chitosan film.

Figure 2-7(a) shows the results for Vicker's microhardness test under three different loads for both types of chitosan films. Error bars were shown in this figure, however, for uncross-linked chitosan, error bars were so small and they can hardly be seen. Elastic modulus was determined for both types of chitosan films by applying the method of nanoindentation into microhardness. Figure 2-7(b) demonstrates the average value of elastic modulus for both types of chitosan films under three different loads. Average elastic moduli of uncross-linked and cross-linked chitosan films were approximately 1.5 GPa and 4.7 GPa, respectively.

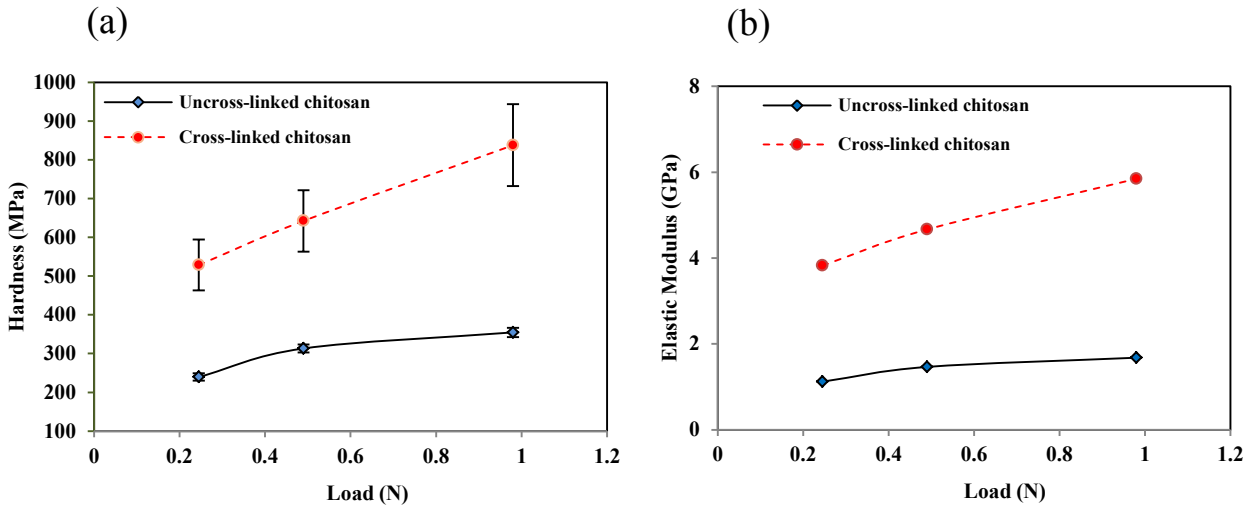

Figure 2-7: Variation of microhardness (a) and elastic modulus (b) versus applied load for uncross-linked and cross-linked chitosan films.

The elastic modulus found using microhardness measurements were less in value than those from the nanoindentation test. Similarly, creating cross-links in chitosan films at least doubled the elastic modulus as illustrated in Figure 2-8. Figure 2-8 summarizes the elastic moduli results from the different types of techniques used. One observation from

this data was that by increasing the load in microhardness test, the elastic modulus also increased for both chitosan samples. Furthermore, the nanoindentation test yielded a much higher elastic modulus when compared to any of the microhardness test results.

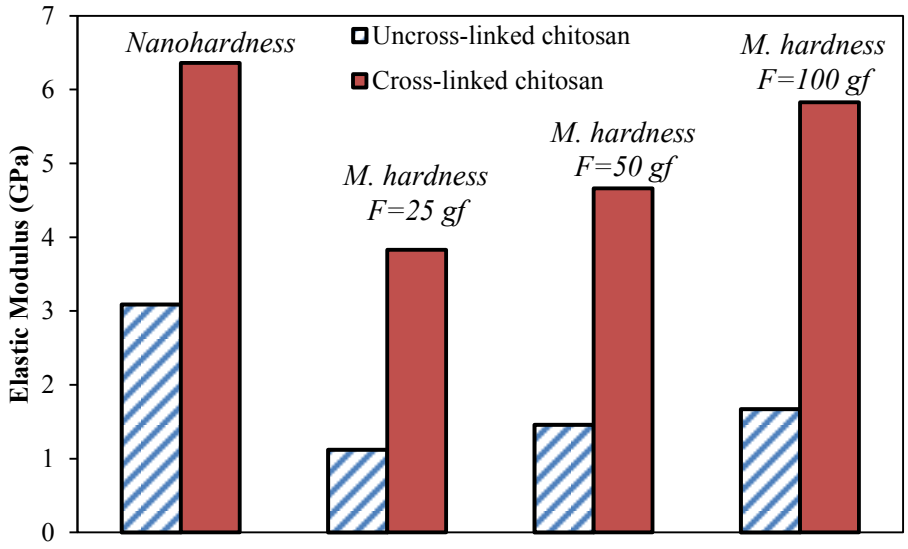

Figure 2-8: Comparison between the elastic modulus which was obtained in different types of chitosan films using microhardness test and nano-indentation hardness test.

2.5 Discussion

In this study, nano and micro mechanical properties of uncross-linked and cross-linked chitosan films were measured using experimental and theoretical modifications [42]. The nanomechanical properties were measured using AFM and microhardness was measured using Vicker's microhradness test for chitosan thin films. AFM is a commonly used method to obtain the nanomechanical properties of polymer thin films [43]. AFM can not only be used for imaging the topography of different surfaces but it is applicable for measuring the forces in nano scale [17].

Elastic modulus was measured using the nanoindentation method and the theoretical modification based on the ratio of plastic and elastic elongations of the chitosan films with the data from the microhardness test.

The elastic modulus values measured by nanoindentation were in agreement with the elastic modulus obtained using the microhardness and theoretical modifications for chitosan films (Figure 2-8).

Chitosan has recently been used for a wide variety of biomedical applications including tissue engineering scaffolds [44]. In order to apply chitosan based materials for bone tissue engineering it is necessary to improve the mechanical properties of these materials. We fabricated the micro-scale particles in our laboratory to research their role in bone regeneration [8, 45]. As stated earlier, the microparticles size and spherical shape made determining their mechanical properties difficult. Therefore, by making chitosan films, this study provided us with insight about the mechanical properties of chitosan materials.

Our results from nanoindentation and microhardness tests have shown that cross-linked chitosan films significantly improved the elastic modulus compared to uncross-linked chitosan films. The measured elastic modulus values for chitosan films were close to the reported values for human bone. Different numbers for elastic modulus of human bone were reported based on gender, age and bone diseases [46]. The reported elastic modulus number varied between 8.2 GPa to 26.6 GPa. Also, an average Vicker's microhardness of 100 μm-thick sections from bone sample at 25 g applied load was 50 kg/mm^2 (490 MPa) [33]. This value was relatively closer to our results of microhardness for cross-linked chitosan films (528 MPa) than microhardness of uncross-linked chitosan

films (239 MPa). This result suggested that creating cross-links in the chitosan films was beneficial because it improved the hardness and elastic modulus.

The average number for nanoindentation hardness was larger than microhardness for different material films [47, 48] which was in agreement with our results. This may be due to the micro dislocations which soften the sample and therefore affect the microhardness test. However, because of the micro order of dislocations, they did not affect the nanoindentation hardness.

By changing the load in microhardness, the films showed different characteristics. According to Figure 2-7, microhardness and elastic modulus increased as the applied load was increased. This usually happens for polymer thin films [49]. By increasing the load, the effect of the substrate is more obvious. By increasing the load, the indentor tip could feel the substrate and because the substrate was a hard material, the total value for hardness increases with increasing of the load.

Creating cross-links in the chitosan films showed the surface brittleness and smoothness (Figures 2-3(b) and 2-3(d)) which was larger in height compared to the uncross-linked chitosan films. In contrast, the uncross-linked chitosan film surface was rough and flat (Figures 2-3(a) and 2-3(c)). This showed that creating cross-links in chitosan film affected the surface roughness. Prior to adding TPP to chitosan, the maximum difference in altitude was about 300 times smaller than cross-linked chitosan sample. Exposing the chitosan sample to the TPP solution even for a short time could change the surface properties of chitosan film.

Brittleness of cross-linked chitosan was evident from the microhardness test. During the microhardness test, the chitosan with TPP treatment showed some cracks that

initiated from the corners of indents. This behavior is common for brittle materials [50]. In contrast, chitosan without the TPP treatment had more ductile surface and no cracks were observed during the tests, as seen in Figure 2-6. The chitosan sample without TPP had a larger material deflection at the same loads of the cross-linked chitosan. This showed the ductility of chitosan. For instance, Figure 2-6 demonstrates in loading condition of uncross-linked chitosan film for maximum applied load of 100 N, when load gradually increases into 80 N, the deflection of uncross-linked chitosan film below the indentor was about 35 μm, but for cross-linked chitosan film the deflection was about 15 μm in the same loading condition.

2.6 Conclusions

In this study, nano and micro mechanical properties of uncross-linked and cross-linked chitosan films were successfully obtained. We measured nanohardness, microhardness and elastic modulus of two types of chitosan films. A new modified method was applied to determine the elastic modulus from microhardness. Results show that cross-linked chitosan films using TPP improve the hardness and mechanical properties of chitosan films. Furthermore, the results show that cross-linked chitosan films are more brittle than uncross-linked chitosan films. Additionally, the new modified method is in agreement with common methods for determining the elastic modulus from hardness.

Chapter 3

ZnO Nanoparticles Effects on Mechanical and Biological Behavior of Chitosan

3.1 Abstract

The aim of this part is to develop novel chitosan/zinc oxide nanocomposite films for biomedical applications. The films were fabricated with 1, 5, 10 and 15% w/w of zinc Oxide (ZnO) nanoparticles (NPs) incorporated with chitosan (CS) using a simple method. The prepared nanocomposite films were characterized using AFM, FT Raman and X-Ray diffraction studies. In addition, nano and micro mechanical properties were obtained. The cell attachment and cytotoxicity of the prepared films at day two and five were evaluated *in vitro* using osteoblast (OBs) cells. As a result, it was found that the microhardness, nanohardness and its corresponding elastic modulus increased with the increasing of ZnO NPs percentage. However, the ductility of films decreased as the percentage of ZnO increased. Furthermore, it was observed that the OB cell viability decreased in films with higher than 5% ZnO NPs. This result suggests that although ZnO NPs can improve the mechanical properties of pure CS films for biomedical and bioengineering applications,

only a very low ZnO percentage can be applied because of the cytotoxicity effects of these particles.

3.2 Introduction

Chitosan (CS) has been used for many different biomedical applications such as drug delivery and tissue engineering due to its favorable biocompatible and biodegradable properties [51-55]. In large scale, CS is produced by deacetylation of chitin which is the primary structural element of shrimp shells and other sea crustaceans. CS is considered as a linear polysaccharide, composed of N-acetyl glucosamine and glucosamine. The ratio of glucosamine to N-acetyl glucosamine is called the degree of deacetylation which is varied from 30% to 95%. When the degree of deacetylation reaches about 50%, CS becomes soluble in aqueous acidic media. One of the main disadvantages of CS as a bone scaffold is its poor mechanical properties [56, 57]. Recently, some studies have investigated adding nanoparticles [58] and cross-linking to improve CS mechanical properties [59] but still more investigations need to be done to achieve acceptable mechanical properties. At neural pH, CS does not show any antibacterial activity and in order to import this activity, one way is to incorporate ZnO NP into it. In addition, the complete investigation on the effects of ZnO NPs incorporated into CS films has not yet been done and it is essential to examine further the toxicity of ZnO under the actual environmental conditions [60].

In the present study, we selected a CS biopolymer as the medium for the incorporation of ZnO NPs. The prepared films were characterized using AFM, X-ray diffraction (XRD) and FT Raman spectrum. We conducted nanohardness test using AFM

and elastic modulus was obtained from loading-unloading curve by applying Oliver-Pharr theory. In addition, microhardness test was done. Cell attachment and cytotoxicity were evaluated using Live/Dead cell assay. The purpose of this study was to: (i) characterize ZnO NPs and investigate its effects (1, 5, 10 and 15% w/w) on mechanical and material properties of CS polymer films incorporating ZnO NPs using diverse methods, and (ii) analyze the extent of ZnO NPs induced cytotoxicity in ZnO NP (1, 5, 10 and 15% w/w) incorporated CS polymer films.

3.3 Materials and methods

3.3.1 Materials and instruments

CS (85% deacetylated medium molecular weight) was purchased from Sigma-Aldrich. ZnO NPs were purchased from Alfa Aesar. A diamond tip mounted stainless steel cantilever (DNISP-MM) was purchased from Brucker. A Clark hardness test machine (CM-400AT) was used for determining microhardness while AFM (Veeco, multimode with nano scope V controller) with a J scanner was used for nanoindentation testing and imaging. Fluorescence images of the cells were taken using a fluorescence microscope (FSX-100, Olympus). 90% alpha minimum essential medium (α-MEM) plus 10% fetal bovine serum (FBS) and 1% penicillin-stereptomycin purchased from Gibco were used for cell culture. To prepare AFM samples, microscope slides with 1 mm thickness (Fisher Scientific) were used. An Invitrogen Live/Dead cell assay kit with Dulbecco's phosphate-buffered saline (DPBS) (Thermal scientific) was used. Gold coating was applied using a sputter coater (Denton vacuum model Desk II). The

morphology images of ZnO NPs were obtained using scanning electron microscopy (SEM) (Hitachi S3200) operating with an accelerating voltage of 20 kV under high vacuum. A conventional secondary electron scintillator detector was used with a tungsten filament. The ZnO NPs were coated with a gold layer (~5 nm) using a sputter coater. XRD patterns (Analytical X'Pert Pro MPD) of the film samples were obtained using Cu kα radiation under the voltage of 45 kV and current of 40 mA. Raman spectra of all groups were recorded by confocal Raman spectrometer (Jobin Yvon Horiba Confocal Raman Spectrometer) with He-Ne laser at 632 nm line excitation.

3.3.2 CS/ZnO NPs film fabrication

CS (2% w/v) solution was prepared by adding 200 mg CS to 10 mL acetic acid 1% (v/v). To fabricate ZnO NP incorporated CS films, 2, 10, 20 and 30 mg of ZnO were measured and separately added to the CS solutions. The solution was rigorously stirred for 1 h to get a homogeneous mixture and cast at room temperature onto clean glass plates, which were previously rinsed with deionized water and dried for 36 h under a hood. Film thickness was approximately between 200-400 μm.

3.3.3 Micro-mechanical and nano-mechanical properties of CS/ZnO films

The microhardness test was performed for the ZnO NPs containing CS films on the glass substrates using a Clark microhardness test machine. Three different loads, 25, 50 and 100 gram force (gf) were applied to the surface of the samples to obtain a Vicker's microhardness number by measuring the indent's diagonal length.

AFM was used to find nanohardness and material behavior under loading and unloading conditions during the nanoindentation test for ZnO NPs incorporated CS films on glass substrates. Nanoindentation measurements were performed by using a diamond tip with the spring constant of 216.8 N/m. This is relatively high spring constant for AFM tips. This tip was used to apply a large force. Applied load was approximately 20,000 nN. The following images were captured in tapping mode at a frequency of 3 Hz. The nanoindentation test was done at 20 different locations of each sample in order to collect accurate and repeatable data. The Scanning Probe Image Processor (SPIP) was used to measure the surface roughness of the films. The method of finding elastic modulus from nanoindentation test will be discussed in appendix A.

3.3.4 Cell culture and viability of osteoblasts (OB-6)

OB-6 murine cell vial (Dr. Lecka Czernik in the Department of Orthopedic Surgery at the University of Toledo kindly provided) which was used for propagation and further studies. OBs were plated on Petri dishes with 100 mm diameters and incubated at 37^{o}C in a humidified 5% CO_2/95% air atmosphere in an osteogenic medium. Cells were monitored and the medium was changed at every 2-3 days. When the dishes reached 80% confluent, the adherent OBs were harvested as follows: cells were washed twice with Hank's balanced salt solution, treated with 2 consecutive applications of trypsin/EDTA for 3-5 min each at room temperature and washed with the growth medium.

3.3.4.1 Cell attachment and spreading

Cellular experiments were performed using five different groups of films: CS (control, 0% ZnO NPs), 1% ZnO+CS, 5% ZnO+CS, 10% ZnO+CS and 15% ZnO+CS. Cell attachment and viability were studied as described below. For each cellular experiment, four replicates were used per group. All types of films were sterilized under UV light for 20 min before starting cellular experiments. Five different types of sterilized films on glass substrates were placed in 24-well plates and seeded with OBs with 35,000 cells per well.

3.3.4.2 Cell viability and cytotoxicity

Attachment and viability of OBs on different films were studied using the Live/Dead cell assay (Molecular probes). At days two and five, the cells were washed with 500 µl DPBS. Also, 500 µl of Calcein-AM/Ethidium homodimer from Live/Dead assay was added to each well and the well plates were incubated for 45 min. The number of live and dead cells from 10 randomly selected images was measured by ImageJ software.

3.3.5 Statistics

The data points on the plots for nanomechanical and cell attachment studies represent the means and ± standard deviation. The nanomechanical and cell attachment data were analyzed using One-way analysis of variance (ANOVA) with the SPSS (V. 17) software and $p<0.05$ (p denotes the probability) was considered statistically significant.

3.4 Results and discussion

3.4.1 Material characterization

3.4.1.1 Morphology of ZnO NPs

The ZnO nanostructures can be in different forms such as fibers, particles, wires and nanorods. Examination of ZnO morphology is important to understand the nano-scale properties of ZnO. Therefore, the morphology of ZnO nanostructures was studied using SEM as shown in Figure 3-1. The average size of ZnO NPs was 30 nm (Figure 3-1) which is also reported by the manufacturer (0.024 μm-0.071 μm). The ZnO NPs in the range of 10–50 nm exhibits antibacterial properties [24, 61].

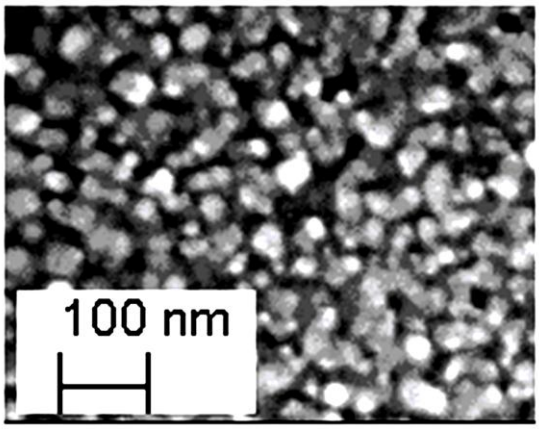

Figure 3-1: SEM image confirmed that ZnO nanostructures are formed as particles approximately 30 nm in diameter.

3.4.1.2 X-Ray diffraction analysis

There are different reported polymorphs structures for CS including “tendon-chitosan”, “annealed”, “noncrystalline”, etc. The tendon (hydrated) crystalline structure gives a reflection at 2θ=10 (or peaks around 8° and 12°) and the anhydrous (annealed)

crystalline gives one peak at 2θ=15° [62]. Figure 3-2 presents the XRD patterns of pure CS, CS/ZnO films and ZnO powder. The pure CS film showed characteristic wide peaks around 2θ=8.8°, 12.1° and 21.1°. The first two peaks corresponded to the hydrated crystalline structure, while the other peak around 2θ=21.1° indicated the existence of an amorphous structure. Such a pattern characterized CS crystal which referred to the "hydrate-amorphous" polymorph. Adding ZnO NP removed the crystalline structure of CS as shown in Figure 3-2. The peaks were more weak and wide as the ZnO NP percentage increased and this implied completely amorphous structure for higher percent of ZnO incorporated CS films. In the range of 2θ=5°-40°, three strong peaks appeared at 32°, 34.4° and 36.4° for ZnO NPs as shown in the figure. These angles corresponded to (100), (002) and (101), respectively [63]. Full width at half maximum (FWHM) of all peaks were small indicating high degree of crystallite orientations. Adding up to 15% ZnO NP did not induce any ZnO corresponded peaks into CS/ZnO films.

3.4.1.3 FT Raman spectrum

Figure 3-3 shows the Raman spectra of the pure CS, CS/ZnO films and ZnO powder. In the range of 200-1200 cm^{-1}, two intense wide bands were observed for pure CS and CS/ZnO films, One band at 300-400 cm^{-1} and the other one at 950-1050 cm^{-1} [64]. The peak in a vicinity of 950 cm^{-1} was assigned to the bond of carbon with oxygen, carbon and nitrogen of the biopolymer [65]. Due to the high transparency of the films, pure CS and CS/ZnO films were coated on silicon substrate for best laser reflection. Thus, strong peak of silicon (~531 cm^{-1}) was observed. The graph in the range of 500-600 cm^{-1} was removed in order to observe just the CS peaks. In addition, Raman study was performed

for ZnO NPs. ZnO NPs had strong peak at 439 cm^{-1} and two smaller peaks at 328 cm^{-1} and 1135 cm^{-1}. The first two peaks were from the zone-boundary phonons $3E_{2H} - E_{2L}$ and E_{2H} mode of ZnO crystal, respectively [66]. Raman spectrums of CS/ZnO films revealed the extra peak at 439 cm^{-1} due to the presence of ZnO NPs. In addition, the first CS peak at around 300 cm^{-1} became stronger and narrower.

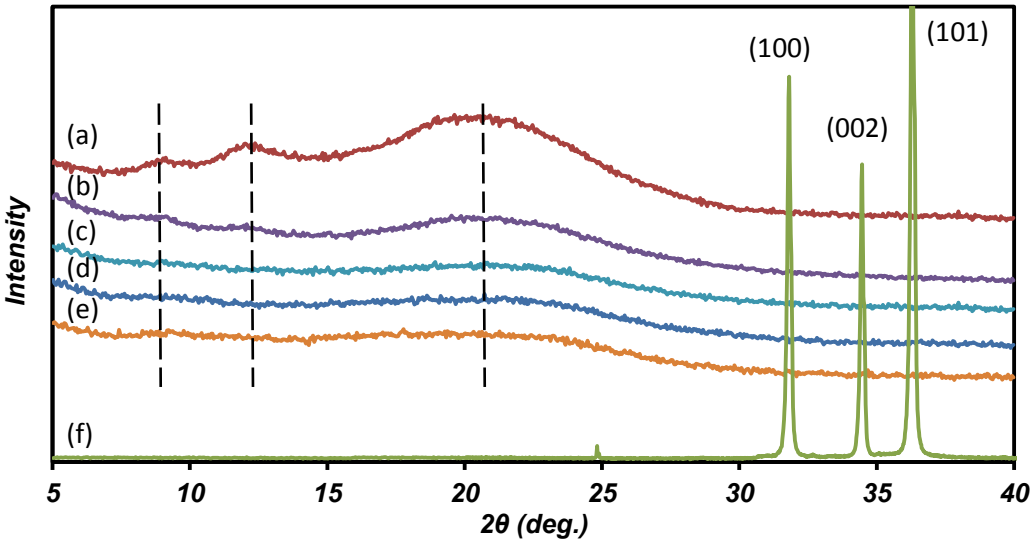

Figure 3-2: XRD patterns of (a) pure CS film, (b) 1% ZnO+CS film, (c) 5% ZnO+CS film, (d) 10% ZnO+CS film, (e) 15% ZnO+CS film and (f) ZnO powder.

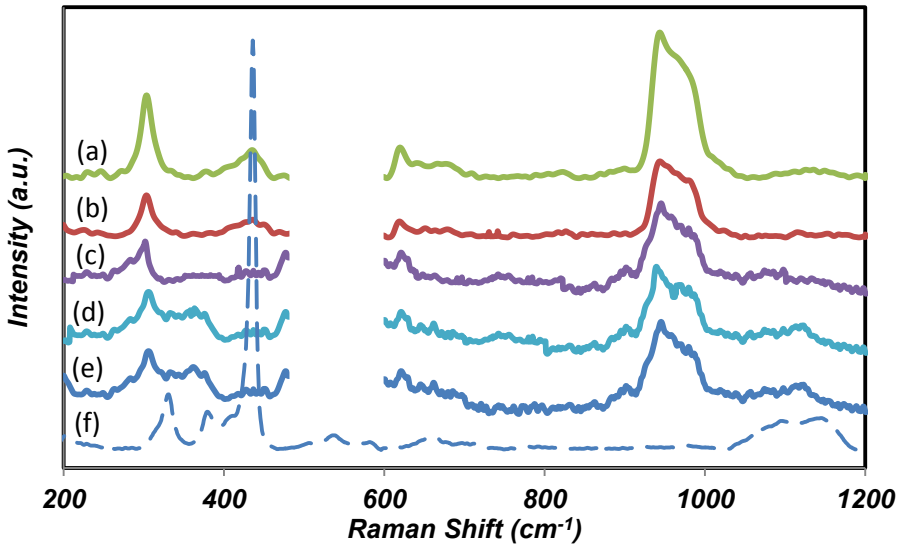

Figure 3-3: Raman spectra of (a) pure CS film, (b) 1% ZnO+CS film, (c) 5% ZnO+CS film, (d) 10% ZnO+CS film, (e) 15% ZnO+CS film and (f) ZnO powder.

3.4.2 Nanomechanical properties - nanoindentation

Information concerning surface roughness and topography of ZnO NP incorporated CS films cast upon glass substrates was obtained using AFM. Surface properties of substrates are important for cellular attachment and growth. Figure 3-4 shows the AFM top view image and three dimensional (3D) plot of the surface of the 1% (a,b), 5% (c,d), 10% (e,f) and 15% (g,h) ZnO NP incorporated CS films in the nanoindentation test. Adding different concentrations of ZnO NPs increased the surface roughness of CS films. The average surface roughness of the films containing ZnO NPs, 1, 5, 10 and 15% was 11.8, 15.8, 16.4, and 19.1 nm, respectively. The AFM images verified that the surface of CS films containing ZnO NPs is homogeneous. No big difference in surface topography was observed due to the low percentage of ZnO NPs. Interestingly, the surface roughness

increased due to the presence of ZnO NPs. This may be helpful for cell attachment [67]. Due to the effect of ZnO NP on CS film surface, nano metal based particles distributed uniformly on the CS film surface during the film coating process. As it is shown in Figure 3-4, the ZnO NPs were almost distributed homogenously and the AFM images revealed the ZnO NPs in the CS film.

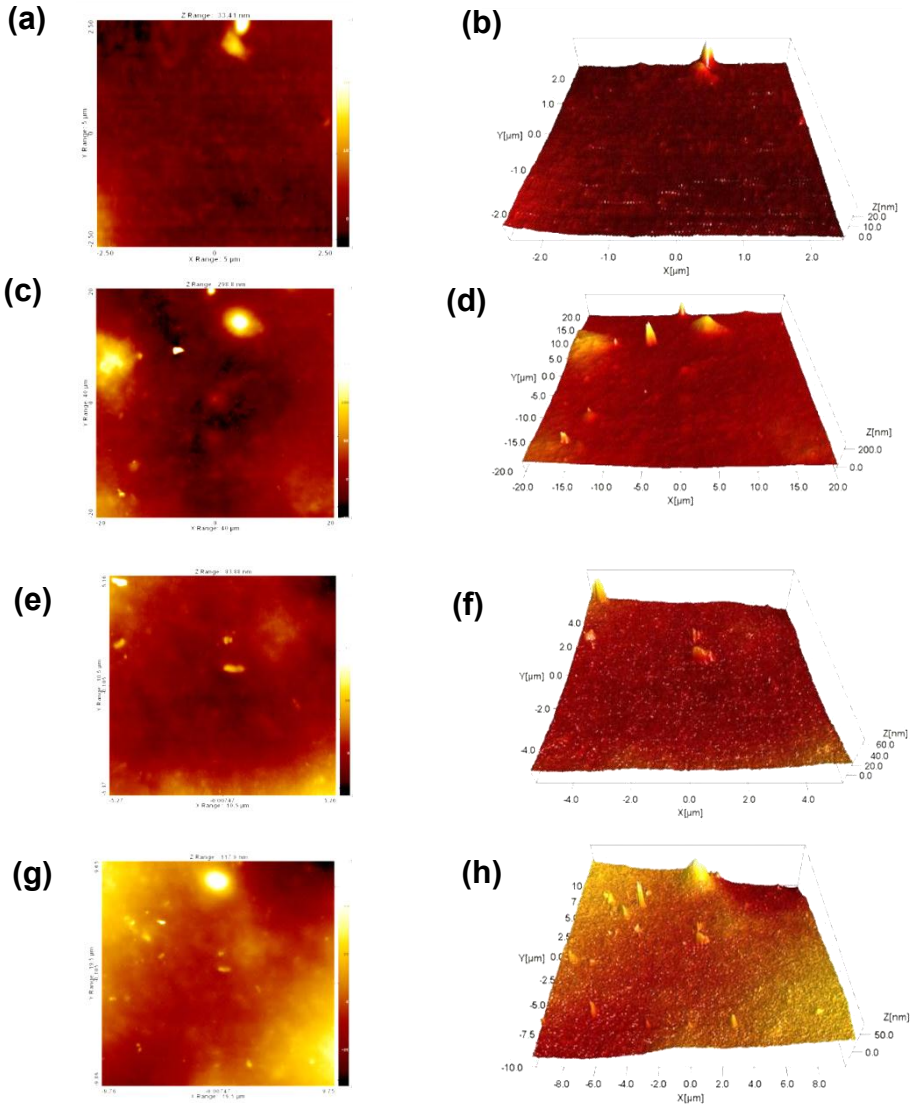

Figure 3-4: AFM image of top view and 3D view for surface of 1% ZnO+CS film (a) and (b), 5% ZnO+CS film (c) and (d), 10% ZnO+CS film (e) and (f), 15% ZnO+CS film (g) and (h).

Theoretical calculations for nanomechanical properties were based on previously published equations [68, 69]. In Oliver-Pharr model which will be described with more details in appendix A, the film was considered as an elastoplastic material. To find the elastic modulus of the samples, the required parameters were derived from Scanning Probe Image Processor (SPIP) software.

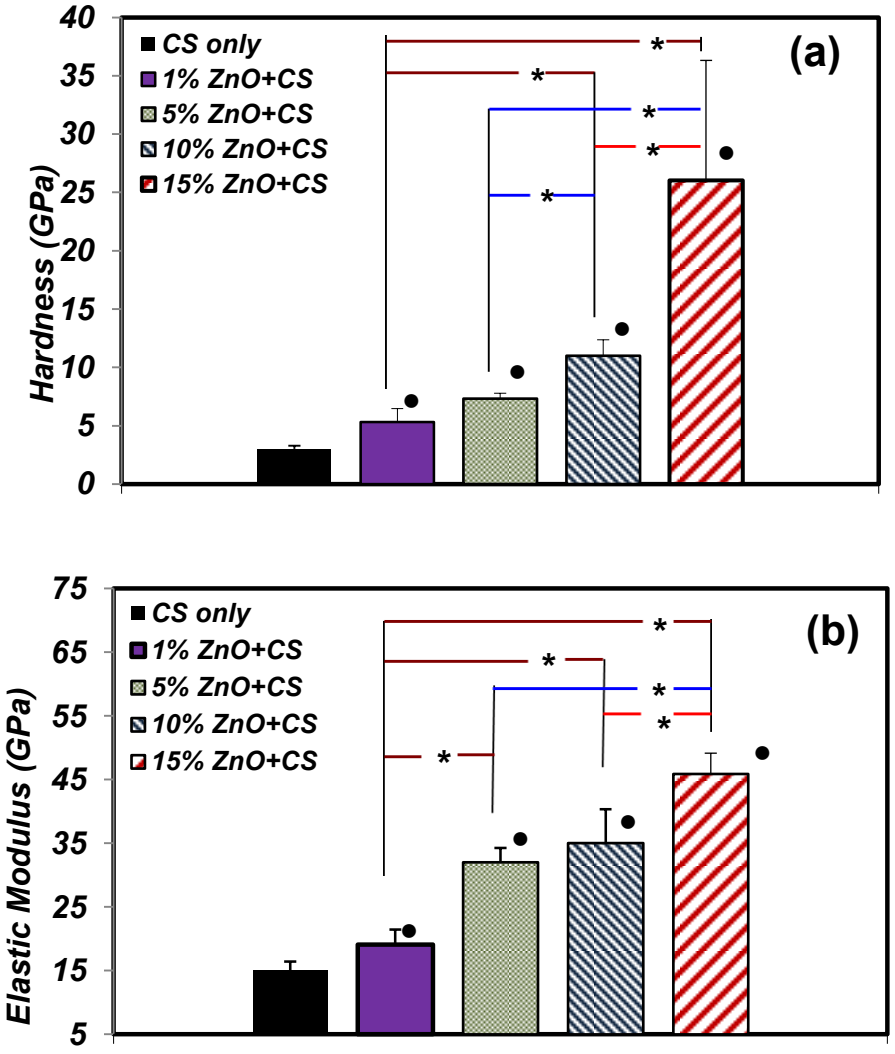

Figure 3-5: Nanohardness (a) and elastic modulus (b) for different amount of ZnO NPs incorporated CS films. * denotes significantly different in each CS film containing ZnO NP) and CS film. ● denotes significantly different data in

compare with CS film). Nanohardeness and elastic modulus increase with increasing numbers of ZnO NPs in the CS film.

Figure 3-5(a) demonstrates the average hardness values for all the pure CS and samples incorporating ZnO NPs. The average hardness of CS films increased with the increase in concentration of ZnO NPs. The average hardness of CS films containing 1, 5, 10 and 15% ZnO NPs were 5, 7, 11 and 26 GPa respectively. This value for pure CS film is 2.6 GPa. The 15% ZnO NP incorporated CS sample showed a significantly higher average hardness compared to all other ZnO NPs incorporated samples ($p<0.05$). Moreover, a significant difference between pure CS films and other groups was observed. In addition, the 10% ZnO NPs incorporated CS sample showed a significantly higher average hardness compared to 1% and 5% ZnO NPs incorporated samples ($p<0.05$). However, the hardness of 1% and 5% ZnO NPs incorporated samples did not exhibit any significant difference.

The elastic modulus of ZnO NPs incorporated CS films is shown in Figure 3-5(b). Similar to the hardness results in Figure 3-5(a), elastic modulus also increases with the increase of percentage of ZnO in the CS films. The elastic modulus of 1, 5, 10, and 15% ZnO NP incorporated CS films were 19, 32, 35, and 46 GPa, respectively. However, the elastic modulus for pure CS film is 15 GPa. The 15% ZnO NP incorporated CS film has the highest elastic modulus among all the other samples. The 10% ZnO NP incorporated sample showed higher elastic modulus in comparison to the 1% ZnO NP incorporated sample. The average of reported Young's modulus value for ZnO NP was between 210-340 GPa [70] which was significantly higher than CS. The hypothesis is the ZnO NPs

have filled into CS vacancies and increase the elastic modulus and hardness. This result was in agreement with the reported tensile tests for zinc oxide deposited in other polymers [71].

3.4.3 Micromechanical properties - microindentation

The deformation of material during loading was determined for different percentages of ZnO incorporated CS films. Based on Vicker's indenter geometry, the indent's diagonal length was obtained [72]. According to nanoindentation results and calculations, the ratio of elastic elongation to plastic elongation (Contact stiffness (S)) for 1, 5, 10 and 15% of ZnO NPs incorporated films were 1.1, 1.3, 1.3 and 1.4, respectively. Moreover, this ratio for pure CS film was 1.9. The loading-unloading curve for pure CS, 1, 5, 10 and 15% of ZnO NPs incorporated CS films at 50 gf load is shown in Figure 3-6. As it is demonstrated in this figure, CS with lower percentage of ZnO shows slightly softer material properties. This shows that adding ZnO NPs increased the brittleness of samples in micro and nano scales. These fractions approximate the ratio of plastic deformation to total deformation of the materials. Regarding to this figure, deformation related to maximum force increased with the films containing lower percentages of ZnO NPs. In other words, by increasing the percentage of ZnO a harder and more brittle film was formed. From another point of view, the effect of three different loads, 25, 50, and 100 gf, on the ZnO NP incorporated CS films were examined. Figure 3-7 demonstrates the suggested loading-unloading curve for 15% ZnO NP incorporated CS films. According to Figure 3-7, the slope of loading-unloading curve increased with higher loads. This behavior was almost the same for all other samples containing ZnO NPs.

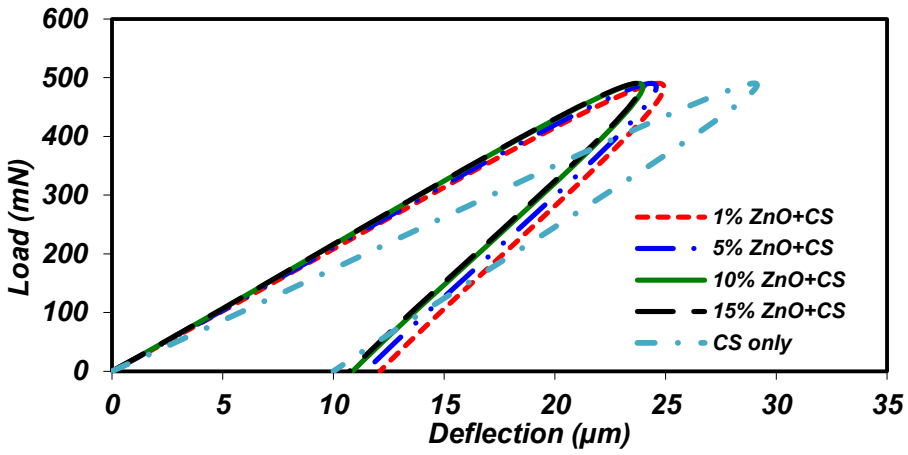

Figure 3-6: Loading- unloading curve in microhardness test for different amount of ZnO NP incorporated CS films at 50 gf load.

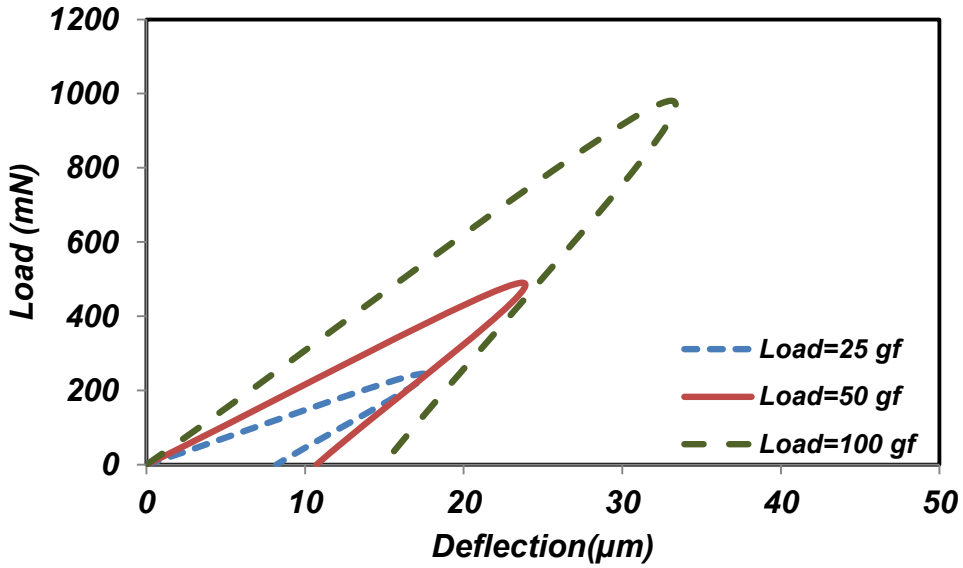

Figure 3-7: Loading and unloading curve in microhardness test for 15% of ZnO NP incorporated CS film with three different loads.

Figure 3-8 represents the results for Vicker's microhardness under three different loads for all different percentages of ZnO NP incorporated CS films and pure CS film. The microhardness values increased with the increase of ZnO NPs concentration in the CS films at the same load. The samples containing 10 and 15% ZnO NPs had approximately the same hardness values. The hardness values also increased with the increase of loads for each sample. The microhardness values of 1, 5, 10, and 15% NPs incorporated CS samples under the applied load of 1 N were 260, 290, 328, and 330 GPa, respectively. Because pure CS was softer than other CS/ZnO films, the effect of substrate was more obvious in this group of samples in higher applied loads. In Figure 3-8, the hardness of pure CS in 100 gf load was slightly higher than CS film with 1% ZnO. The applied load was high enough for indentor to feel the hard substrate.

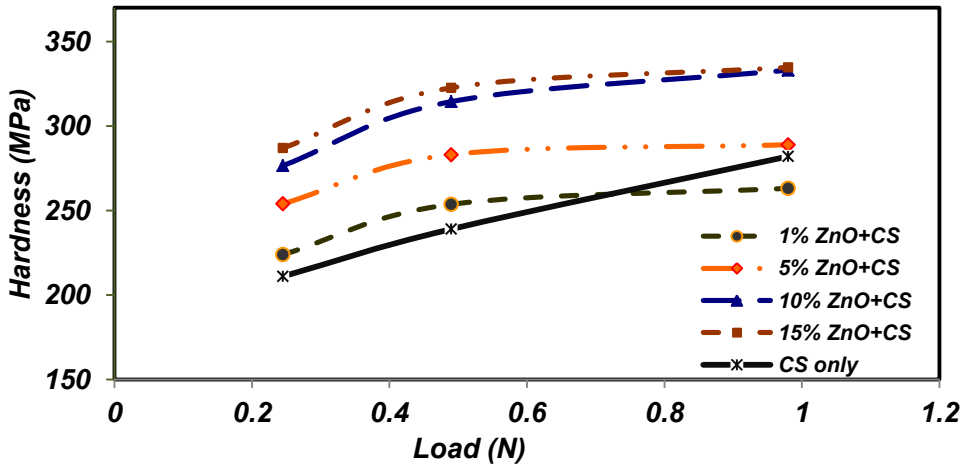

Figure 3-8: Microhardness versus applied load for different amount of ZnO NP incorporated CS films.

The hardness values from nanoindentation were higher compared to those derived from microindentation for all types of samples. One of the main differences between the nanoindentation and microhardness tests was that the applied force was smaller in nanoindentation compared to the microindentation measurement. Similar behavior was reported for different types of materials including metals, ceramics and polymers [50, 59].

3.4.4 Cell viability

In order to obtain indications of cell viability on ZnO NPs, murine OBs were seeded on 24 well plates containing ZnO NP/CS films at a density of 30,000 cells per well. Similar to the above mechanical property measurements, four different percentages of ZnO NPs, 1, 5, 10, and 15% were incorporated with CS films. Cell viability assay was performed using a Live/Dead cell assay (Molecular probes) after washing unattached cells with phosphate buffered saline (PBS) at day two and five (n=3). After treating with Live/Dead cell assay, live cells were stained with green and dead cells were stained with red. Figure 3-9 shows the fluorescence images of OBs for 0%, control (a), 1% (b), 5%, (c) 10% (d) and 15% (e) ZnO NPs incorporated CS films at day two. The OBs were attached to the control CS film along with all other ZnO NP incorporated films at day two. The films containing 10% ZnO NPs showed a few red cells compared to the control at day two (Figure 3-9(d)). More cells were dead in the sample containing 15% ZnO NPs (Figure 3-9(e)).

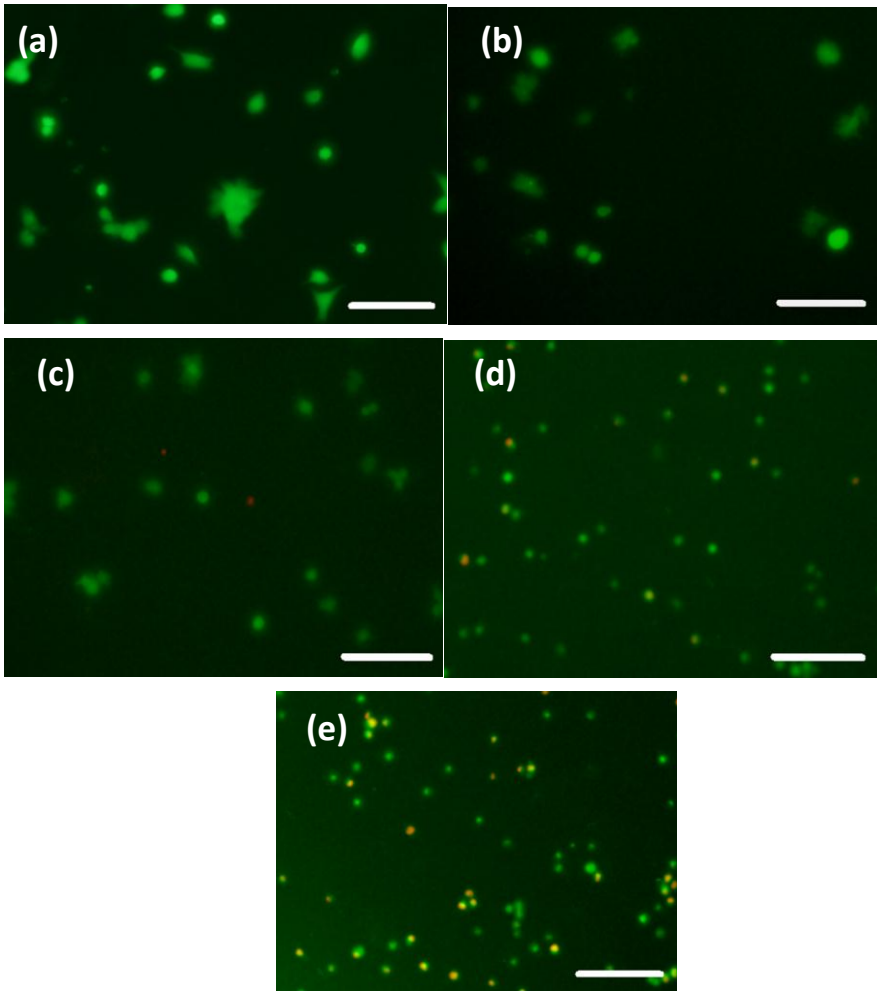

Figure 3-9: Fluorescence microscopy images for OB attached to different types of films treated with Live/Dead cell assay at day two: (a) CS, (b) 1% ZnO+CS film, (c) 5% ZnO+CS film, (d) 10% ZnO+CS film, (e) 15% ZnO+CS film. Scale bar is 150 µm.

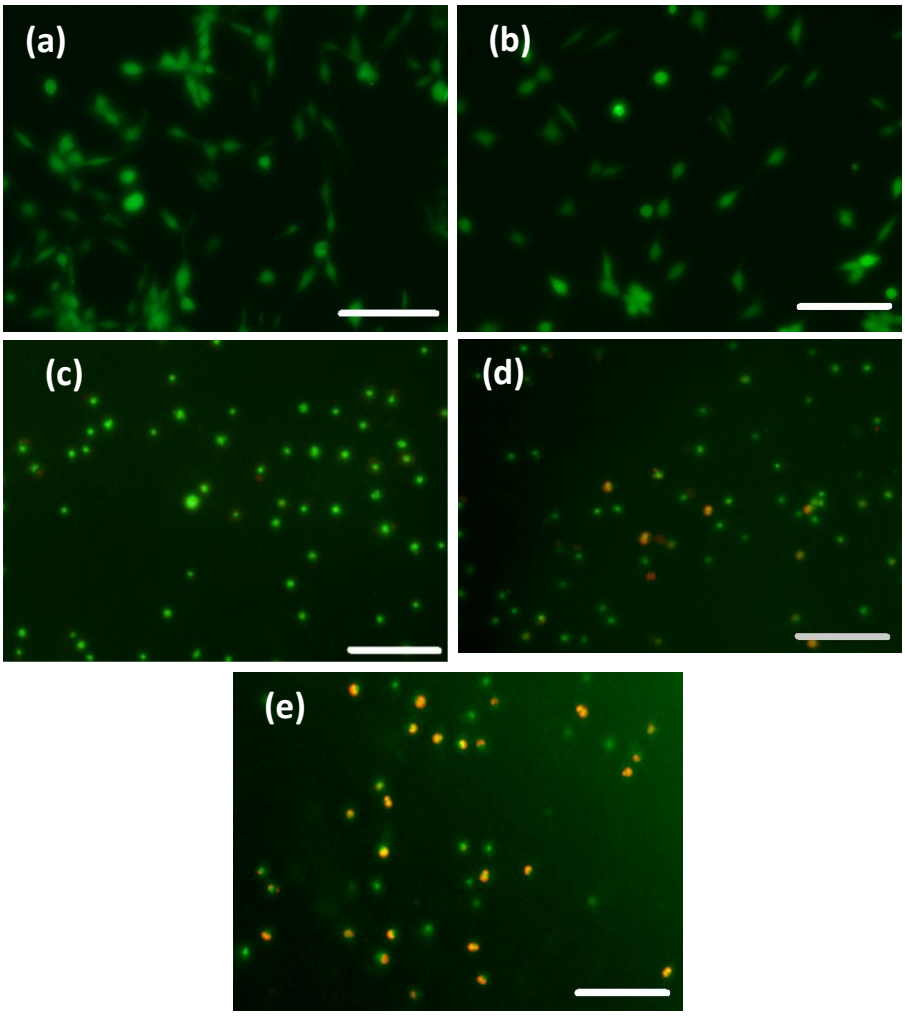

Figure 3-10: Fluorescence microscopy images for OB attached to different types of films treated with Live/Dead cell assay at day five: (a) CS, (b) 1% ZnO+CS film, (c) 5% ZnO+CS film, (d) 10% ZnO+CS film, (e) 15% ZnO+CS film. Scale bar is 150 µm.

Figure 3-10 shows the fluorescence images of OBs for 0%, control (a), 1% (b), 5%, (c) 10% (d) and 15% (e) ZnO NPs incorporated CS films at day five. The OB spread in control (Figure 3-10(a)) and in 1% ZnO NP incorporated sample (Figure 3-10(b)) with

high cell viability at day five. However, the samples containing higher amounts of ZnO NPs (5%, 10% and 15%) did not show evidence of cell spreading at day five. In addition, the number of dead cells increased with the increase of ZnO NP amount in the CS films (Figure 3-10(c), (d), (e)) at day five.

Figure 3-11 represents the cell attachment plot for all the groups, including CS (control) at days two and five. Cell attachment significantly increased for control films and 1% ZnO NP incorporated CS films at day five compared to day two. When we increased the amount of ZnO NPs to 10 and 15% in the CS films, the average number of cell attachment on those films was drastically reduced compared to the control. Even though the 5% ZnO NP incorporated CS film did not show significantly lower cell attachment compared to the control films at day two, approximately 50% lower cell attachment was observed at day five. The obtained result was in agreement with previous papers [73, 74].

This result suggested that cells are viable with CS film incorporated with lower amounts of ZnO NP (1% w/w). The cytotoxicity of cells was observed in higher percentages of ZnO NP (above 5% w/w) incorporated CS films; ZnO cytotoxicity was reported in many previous studies [26, 75-77]. It should be noted that in this investigation, ZnO NPs were used as received from the company (Sigma-Aldrich). We did not perform any surface modification treatment for the ZnO NPs, but cell viability of ZnO NP incorporated CS could potentially be improved if surface modified ZnO NPs were used. There were better micro and nanomechanical properties of the samples containing higher ZnO NPs. However, cell viability was poor in the higher ZnO NP containing CS films. Therefore, mechanical properties and cell viability should be

optimized when polymer/ZnO NP scaffolds or any other form is used for tissue regeneration applications. A recent study reported that when ZnO incorporated into hydroxyapatite/CS cement, bone regeneration is enhanced in osseous defects in rabbit tibia [78]. It is worthwhile to study cell viability with ZnO NPs incorporated in matrices less than 5% w/w as well.

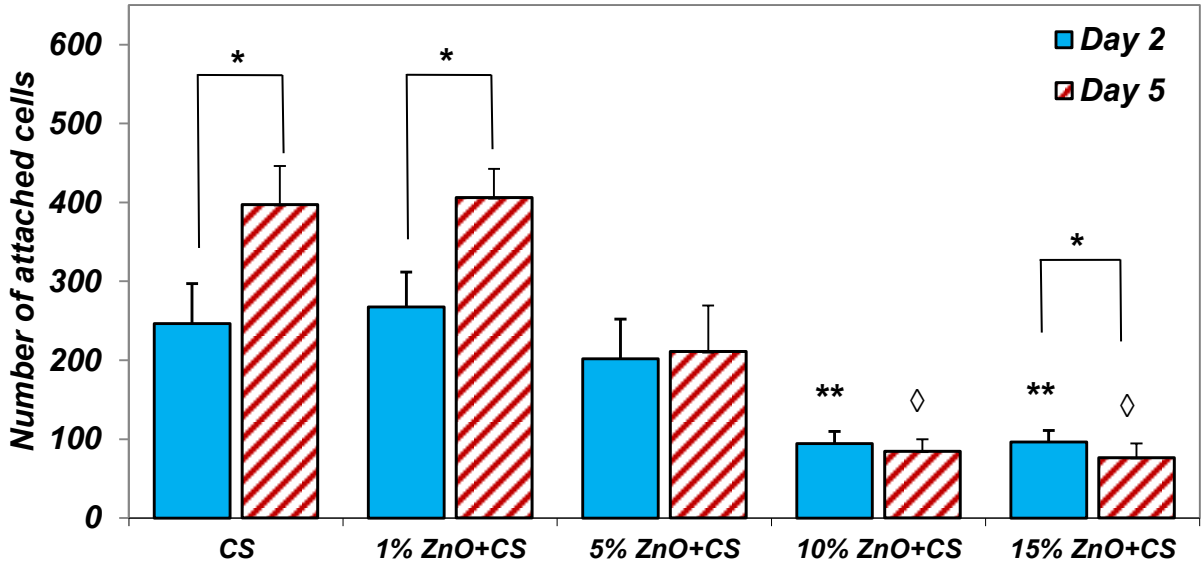

Figure 3-11: The quantitative results for OB attachment on the different amount of ZnO NP incorporated CS films. This result shows the effect of different amount of ZnO NPs for OB attachment. (* denotes statistically significant data for each group in different time points. ** and ◊ denote the statistical significance of cell attachment on different groups at day two and five compared to the CS control respectively.

3.5 Conclusions

In this study, we fabricated CS films with different percentages (1, 5, 10 and 15% w/w) of incorporated ZnO NPs upon glass substrates using a solvent cast method. We were able to obtain homogeneous and smooth ZnO NP incorporated CS films. SEM, XRD and FT Raman studies were used for material characterization [79]. We investigated micro and nanomechanical properties of ZnO NP incorporated films using microindentation and nanoindentation. On one hand, the nanohardness, microhardness and elastic modulus derived from nanoindentation increase as a function of the amount of ZnO NPs incorporated with CS films. On the other hand, we observed that cell viability decreases on the CS films with increasing numbers of ZnO NPs. It should be noted that ZnO NPs were used as received, without further purification. That being said, there may be possibilities to increase the cell viability using further purified ZnO NPs. In conclusion, incorporation of ZnO NPs into the polymer matrices for biomedical applications, mechanical properties and cell viability needs optimization according to our results.

Chapter 4

Mechanical and Biological Properties of Chitosan Carbon Nanotube Nanocomposite Films

4.1 Abstract

In this section, different concentrations of multi-walled carbon nanotube (MWCNT) were homogeneously dispersed throughout the chitosan (CS) matrix. A simple solvent-cast method was used to fabricate chitosan films with 0.1, 0.5, and 1% of MWCNT with the average diameter around 30 nm. The CS/MWCNT films were characterized for structural, viscous and mechanical properties with optical microscopy, wide-angle X-ray diffraction, Raman spectroscopy, tensile test machine, and microindentation testing machine. Murine osteoblasts were used to examine the cell viability and attachment of the nanocomposite films at two time points. In comparison to the pure chitosan film, the mechanical properties, including the tensile modulus and strength of the films were greatly improved by increasing the percentage of MWCNT. Furthermore, adding MWCNT up to 1% increased the viscosity of the chitosan solution by 15%. However, adding MWCNT decreased the samples ductility and transparency. In biological point of view, no toxic effect on osteoblasts was observed in the presence of different percentages

of MWCNT at day 3 and day 7. This investigation suggested MWCNT could be a promising candidate for improving chitosan mechanical properties without inducing remarkable cytotoxicity on bone cells.

4.2 Introduction

The need for optimized designs of tissue engineering scaffolds has resulted in the advancement of biomaterial composites with unexceptional properties [80, 81]. Following the discovery of carbon nanotube (CNT) in 1991 [82], these nanosized materials have quickly become a technological platform for researchers in diverse fields of science including materials and biomedical engineering. CNT is one of the most useful nanoscale agents for diverse material properties reinforcement due to its extraordinary mechanical, electrical and thermal properties [83-85]. CNT's have shown controversial and complex properties. On one hand, pristine CNT has displayed cytotoxicity on certain cell lines , which can be attributed to the usage of metal catalysts such as nickel during CNT fabrication [86]. On the other hand, CNT incorporated with biopolymers has shown great biocompatibility [87-89]. Despite a growing debate of the cytotoxicity nature of CNT, the published articles showing interest in this field have doubled in recent years [90]. Researchers are continually improving their knowledge on CNT effects on the biological surroundings by designing novel methods to use CNT in biomedical engineering. CNT has been used to enhance the mechanical properties of different forms of biomaterials such as hydrogels [91, 92] and conventional polymer solutions [93-95].

Chitosan (CS) is one of the natural polysaccharides derived from chitin with wide current and potential range of applications in biology, medicine and biotechnology [7]. It

has been widely used as the base material for bone tissue engineering, specifically for bone tissue scaffolds. In addition, diverse forms of CS such as microparticles, film and gel have been developed [53]. The CS/CNT combination was also previously used for biosensor applications [96] and recently proposed for CNT-based scaffolds fabrication [97]. Despite the great properties of CS such as biocompatibility and biodegradability, CS has demonstrated poor mechanical properties when CS does not cross-linked. In addition, CS solution can be used as aqueous injectable gel for inducing new bone formation, therefore the surgical implantation is not necessary [98-100]. Injectable chitosan gel supplemented with bone marrow proteins has been reported to drastically enhance new bone tissue formation due to more efficient cell delivery than a solid scaffold [99]. In this sense, investigating and improving the injectability and viscosity properties of CS solution is vital for potential usage of CS injectable gels. Among diverse nanomaterials, CNT is one of the promising candidates to improve CS scaffold and gel mechanical and injectability properties as well as the electrical and thermal properties [101-104].

To the best of author's knowledge, most of the related papers investigated either the material properties or cell compatibility of CS/CNT composites. Considering the high capability of CNTs, the targets of investigation for CS/CNT nanocomposite film were complete material characterization, mechanical properties, and cell biocompatibility. We selected multi-walled carbon nanotube (MWCNT) to reinforce CS matrix since MWCNT is proven to be more beneficial in biomedical engineering applications than single-walled carbon nanotube (SWCNT) is [105, 106].

The aim of this paper is to present the comprehensive investigation of CS/MWCNT nanocomposite films fabricated with a simple procedure. We used low CS concentration

as used to make microparticles and films in our laboratory [8, 59]. Moreover, lower CS concentration has been shown to be beneficial for CNT dispersion [107]. Four concentrations of CS/MWCNT films were fabricated and used in this study. We reported structural, optical, injectability and mechanical properties as well as cell cytotoxicity of the films.

4.3 Experimental section

4.3.1 Materials

CS of medium molecular weight (75-85% deacetylated) was purchased from Sigma-Aldrich. MWCNT was obtained from Alfa Aesar. MWCNT's mixture typically has nanotubes with 10-30 μm length and other carbon particulates as mentioned in the manufacturer catalog. As prepared MWCNT was gently washed with deionized water and filtered to remove any impurities.

4.3.2 CS/MWCNT nanocomposite film fabrication

To make MWCNT suspension, 25 mg of MWCNT was first suspended in 100 mL of 1% acetic acid (v/v) diluted with deionized water. MWCNT suspension was homogenized in ultrasonic bath (BRANSON 2510) for 90 min at 35°C. 2% CS solution was separately made by dissolving 400 mg of CS (w/v) into 20 mL of 1% acetic acid. Similar CS solutions have been widely used for bone tissue scaffold fabrication in different forms including injectable gel and exhibited great biocompatibility and degradability [108]. Using a magnetic stirrer, 2% CS solution was completely mixed for

60 min. By adding appropriate volume of MWCNT suspension into CS solution, CS/MWCNT mixtures with 0.1, 0.5 and 1% of MWCNT were fabricated. The final mixtures were also stirred for 60 min followed by sonication for 20 min to remove air bubbles. The injection tests were performed on these solutions. A part of each prepared solutions was placed in the glass vial to examine the homogeneity and stability after 3 days in a stationary position. To fabricate CS/MWCNT films, the solutions with different MWCNT percentages were casted into a clean microscope glass slides (7.5 cm x 2.5 cm x 1 mm) and dried at room temperature. Dried uniform thin films with an average thickness of 0.06 mm (measured by caliper) were easily removed from the glass slides by initially peeling off the edges using a sharp tip. The films came off in one piece without any particular treatment.

4.3.3 Injection and tensile test

To calculate the effect of MWCNT on the viscosity of CS, CS/MWCNT solutions were injected from a 10 mL syringe with the needle gauge of 19 G. Injection tests were performed at room temperature with the injection speed of 100 mm/min using an ADMET universal testing machine (expert 2611) with customized grips. Assuming Newtonian fluid passing through a narrow tube, the Hagen-Poiseuille equation can describe the relation of viscosity and applied force during the injection test [109]:

$$Q_i = \frac{\Delta P_i \pi D_n^4}{128 \mu_p L_n}$$

In this equation, Q_i is fluid flow rate running through the syringe, D_n is the needle length, μ_p is the fluid viscosity, ΔP_i is the pressure drop and L_n is the length of needle.

The geometric parameters were easily obtained from measuring instruments or from the manufacturer's manual and available standards.

Tensile tests were carried out using the same machine at room temperature with a gauge length of 50 mm and crosshead speed of 25 mm/min. Each test was done at least 3 times and the reported values here are the average of the obtained data.

4.3.4 Raman spectra and X-ray diffraction (XRD)

Raman spectra of the films were obtained at room temperature with a Jobin Yvon Horiba confocal Raman spectrometer in backscattering geometry with the laser excitation of 632.8 nm at a power level of 1.7 mV. XRD patterns of the films were obtained by PANanalytical X'Pert Pro MPD using Cu kα radiation under a voltage of 45 kV and current of 40 mA.

4.3.5 Scanning Electron microscopy (SEM), optical microscopy, transmittance spectroscopy and microhardness test

SEM images were obtained using Hitachi S4800 operating with an accelerating voltage of 10 kV under high vacuum. The obtained images were quantitatively analyzed using ImageJ software. The optical and fluorescence microscopy images of CS/MWCNT films were taken by a FSX-100 Olympus microscope. The transmittance tests of CS/MWCNT films on glass substrate were performed by an ultraviolet-visible (UV-VIS-NIR) spectrometer. Microhardness tests were conducted using a Clark CM-400AT hardness test machine at 10 gf load.

4.3.6 pH measurement and film-cell interaction study

To track the effect of MWCNT on the films pH level, two phosphate buffered saline (PBS) solutions with the molarity of 10 mM and adjusted pH of 7.4 and 5 were prepared. CS/MWCNT films were cut into small pieces (2 cm x 2 cm) and placed in the glass vial filled with 12 mL of the PBS. The vials were kept in incubator at 37 °C. pH values were measured every week for 22 weeks by using a Mettler Toledo S20-K pH meter kit.

Murine osteoblast cell line (OB6) was used for propagation and further studies. Cells were plated on a petri dish with 100 mm diameter. Two time points (day 3 and day 7) were selected to examine the cytotoxicity and cell attachment of CS/MWCNT films. Films were cut into small pieces (1 cm x 1 cm), sterilized under UV light for 10 min before adding original cell suspension. Four types of sterilized films were placed in 24-well plates and seeded with OBs with the concentration of 25000 cells per well. Well plates were incubated at 37°C in a humidified 5% CO_2/95% air atmosphere in an osteogenic medium. Cell culture media was changed every 2-3 days.

To prepare cell culture medium, alpha minimum essential medium (α-MEM) containing 10% fetal bovine serum (FBS) and 1% penicillin-streptomycin (Pen Strep) were purchased from Gibco. An Invitrogen Live/Dead cell assay kit with Dulbecco's phosphate buffered saline (DPBS) (Thermal Scientific) was used to identify live and dead cells.

4.4 Result and discussion

4.4.1 Structure and morphology

As presented in supporting information section, characterization of the fibers using SEM showed the MWCNT structure and morphology (Figure 4-1(a)). MWCNT adhered together and formed bulk shape containing various numbers of individual MWCNT [110]. Images were used to analyze MWCNT size distribution (Figure 4-1(b)). In terms of the diameters, bare MWCNT were measured to be ~ 31.48±16 nm.

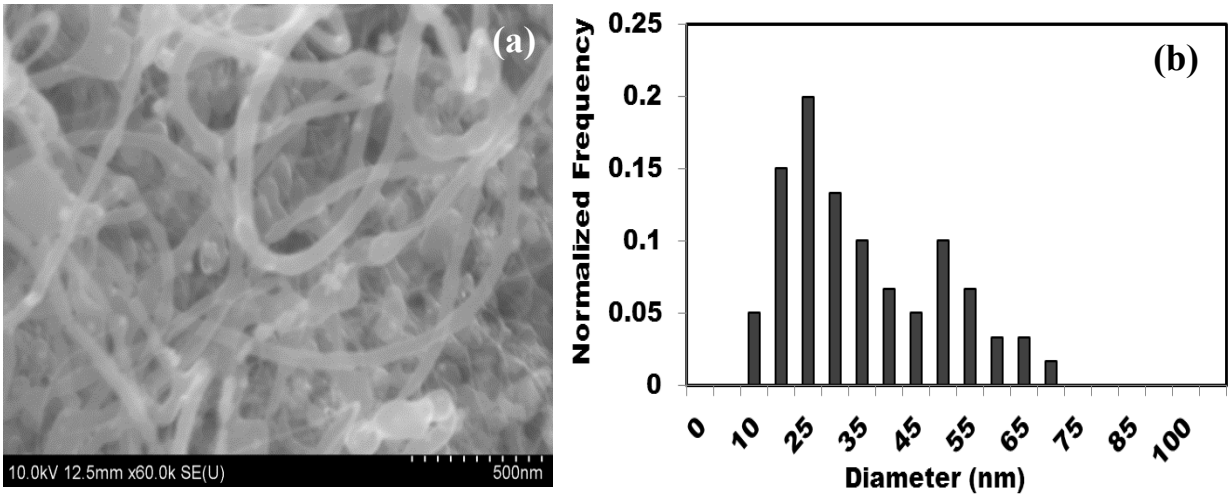

Figure 4-1: (a) SEM image of MWCNT. (b) Diameter size distribution of individual MWCNT.

MWCNT has poor wetting properties in water such that it aggregated and precipitated in a stationary position. As shown in Figure 4-2, MWCNT powder that was suspended into 1% acetic acid and sonicated for 1 h, mostly settled down after 20 min in a stationary position [111].

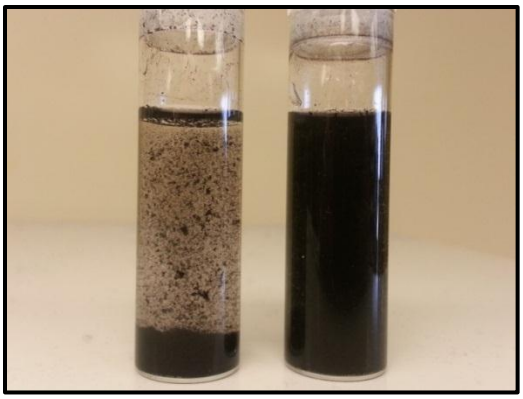

Figure 4-2: MWCNT suspended in 1% acetic acid immediately after sonication and 20 min after sonication.

CS/MWCNT mixtures displayed different appearance. As shown in Figure 4-3(a), after adding, mixing and sonication of MWCNT into CS solution, the dispersion and solubility of MWCNT were significantly improved. This image was taken after 3 days of placing solutions in a stationary position.

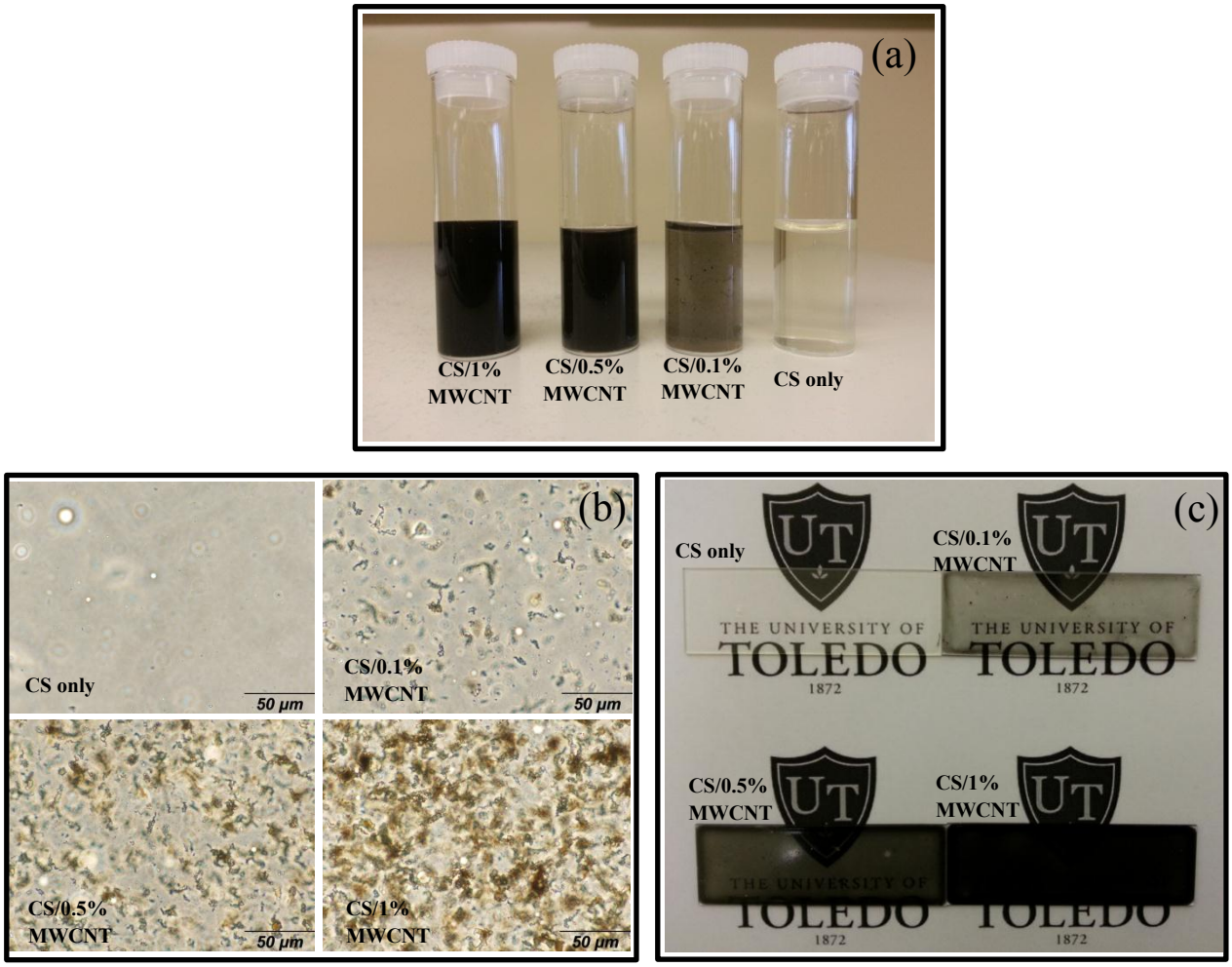

Figure 4-3: (a) CS/MWCNT nanocomposite films with different percentages of MWCNT after 3 days in a stationary position. (b) Optical microscopy images and (c) normal camera images of CS/MWCNT films with different concentrations of MWCNT.

It also showed that the MWCNT and CS interaction improved the dispersion of MWCNT. Generally, MWCNT's floated on water, thus it was difficult to obtain a

uniform solution of MWCNT spreading over on the water or 1% acetic acid. This is due to the large aspect ratio of MWCNT as well as the water surface tension. The higher percentage of MWCNT dispersed in CS solution, the darker black color of final mixture. The ultimate composition was completely stable and no degradation, separation or floccule was observed after one month of visual tracking.

The deposition of MWCNT in the CS matrix was examined using optical microscopy as shown in Figure 4-3(b). Deposited MWCNT absorbed the light and seen as the black particles on the image. By increasing the percentage of MWCNT in CS films, the number of black spots showing aggregated MWCNT increased. However, this figure demonstrates that MWCNT's were uniformly distributed in CS matrix. The level of distribution was acceptable compared with other previous similar works [112, 113]. The small isotropic aggregations were unavoidable because the sonication process did not induce enough energy to overcome depletion and nanotube van der Waals attraction between MWCNT or their bundles [114]. In addition, the high-resolution camera photographs of CS/MWCNT films with various MWCNT loadings provided direct evidence for evaluating the homogeneity of films (Figure 4-3(c)). This image gives an insight of how the fabricated films look like. CS film with 1% MWCNT was almost completely opaque, which was verified by later transmittance measurement.

4.4.2 XRD and optical properties

Generally, seven polymorph models have been suggested for CS [112, 115]. CS has three peaks correspond to two crystal structures [116]. XRD pattern of the samples is demonstrated in Figure 4-4. Two former characteristic peaks around $2\theta=8.5^{\circ}$ and 11.5°

indicated a hydrated (tendon) crystalline, whereas the latter peak at 19˚ showed an amorphous structure of CS. The broadening of the peaks was due to the amorphous nature of polymers [117]. For all CS/MWCNT films, nearly the same XRD graphs were obtained showing the same crystalline structure. MWCNT including a strong peak at 2θ=25˚ corresponds to (002) crystal plane [118, 119]. This figure displays the incorporation of small percentages of MWCNT into CS films did not affect the crystalline structure of CS films because all four samples had approximately same peaks.

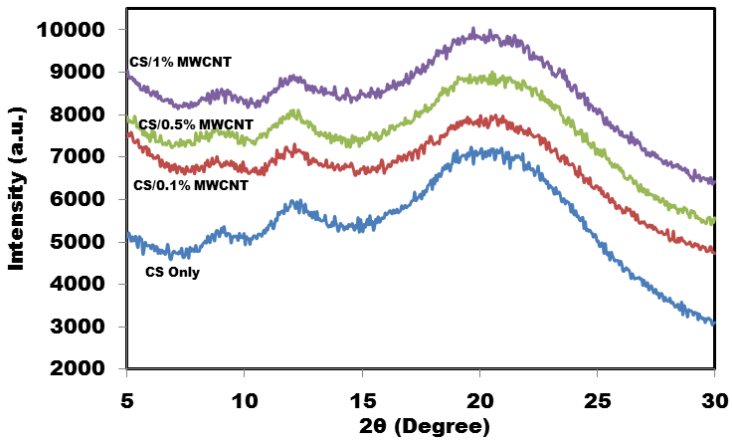

Figure 4-4: XRD patterns of CS/MWCNT films with different concentrations of MWCNT.

The optical properties and dispersion quality of CS/MWCNT films were also examined by UV/VIS transmittance measurements (Figure 4-5(a)). At wavelengths higher than 450 nm, adding up to 1% MWCNT can decrease the transmittance value to 40%. Based on Lamber-Beer's law, absorbance can be easily calculated from the graph. As shown in Figure 4-5(b), a linear relation was observed between the percentage of MWCNT and absorbance which is in agreement with other works [120, 121].

Furthermore, the linear fashion is usually attributed to the rich dispersion of CNT [122]. Small error in linear behavior is negligible and can be explained as the effect of glass substrate used as a film support.

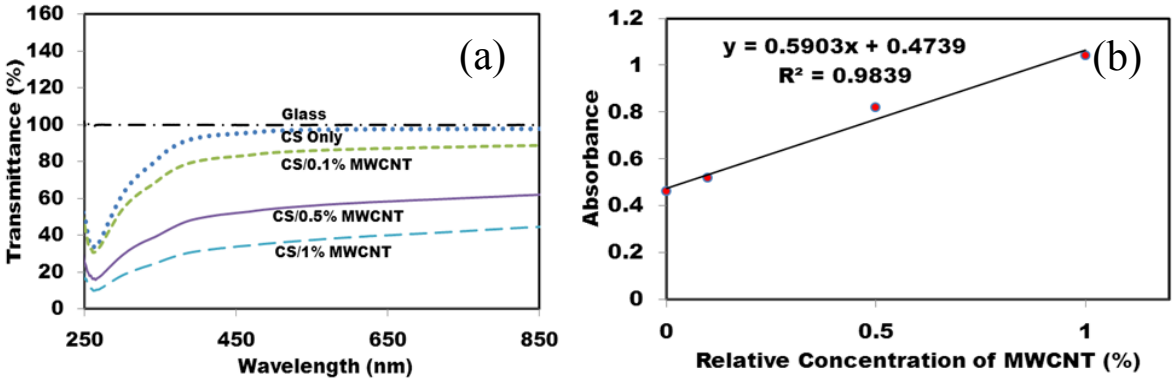

Figure 4-5: (a) Transmittance curves for CS films with different concentrations of MWCNT. (b) Absorbance of CS/MWCNT films as a function of relative concentration of MWCNTs.

4.4.3 Raman spectra analysis

Raman spectra demonstrated the differences between CS and CS/MWCNT composite films. A major application of Raman spectroscopy is to recognize specific groups where relatively large molecules are involved. Raman spectrometry of the films is shown in Figure 4-6. For pure CS and CS/MWCNT films a portion of graph ranging from 480-700 cm^{-1} was eliminated due to the large peak of silicon substrate. Silicon was used as an opaque substrate for the best laser reflection and Raman spectra results. Normal CS Raman bands were observed at 100, 280 and 935 cm^{-1} [64]. A later peak corresponded to a C—O—C band. The first and second peaks indicated lattice vibration and δ(C—C) band stretching, respectively.

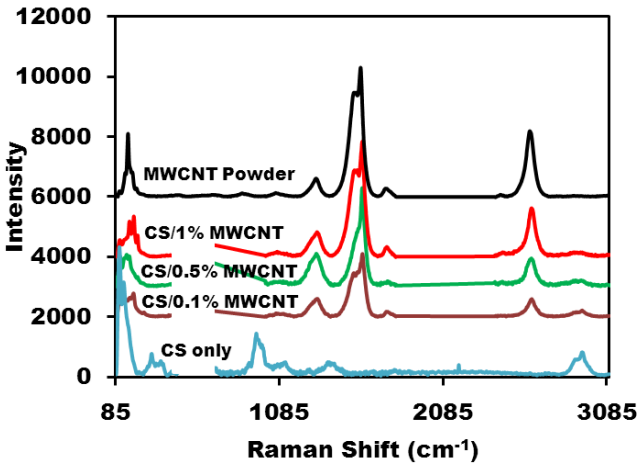

Figure 4-6: Raman spectra of CS films with different MWCNT concentrations and MWCNT powder.

It also displayed a broadening peak at 1100 cm^{-1} which corresponded to υ(C─C) band. Another typical intense band was due to υ(C═O) stretching at 1355 cm^{-1}. Finally, a peak at 2850 cm^{-1} corresponded to a C─CH_3 band [123, 124]. Furthermore, MWCNT powder Raman spectra revealed a number of main peaks. A low energy mode observed at Raman shift between 100-200 cm^{-1} is considered a "radial breathing modes" (RBM) where all atoms vibrate radially in phase [122, 125]. D and G band peaks at Raman shift were between 1200-1340 cm^{-1}. The last peak corresponded to G' (D^*) band at Raman shift between 2450-2650 cm^{-1} [126, 127]. CS/MWCNT films with different percentages of MWCNT had approximately the same peaks and peak ratios as MWCNT powder. However, all peaks of MWCNT shifted to higher wavelengths upon blending with CS, showing strong interactions between CNT and CS. This was due to an increase of the energy of CS coated MWCNTs [128]. The hydrophobic and π─π interactions between

the CS (─C═OCH_3) and (C═C) bands increased the required vibrational energy which resulted in upshift of Raman peaks [129].

4.4.4 pH measurement of films

Since pH is a critical and important factor in physiological applications, we measured the pH level of samples in two PBS solutions with the initial pH values of 7.4 (Figure 4-7(a)) and 5 (Figure 4-7(b)). CS is a pH-responsive polymer because of the existing amino groups. As shown in Figure 4-7, the pH changed rapidly during the early weeks and finally leveled off to about 7 and 6.8 for the initial pH of 7.4 and 5, respectively. Samples in both PBS solutions swelled after a few days and they completely disappeared after 5-6 weeks showing the degradability of the films in normal pHs. MWCNTs settled down at the bottom of the plastic vials. With the initial pH value of 7.4, the pH changing fluctuation was less than one. This fluctuation was even smaller for CS/1% MWCNT at early weeks. For all samples with the initial pH value of 5, the pHs almost reached their final value after six weeks. An increase in pH demonstrated a decrease in hydrogen ion concentration. Adding MWCNT did not show significant effect on pH changing of CS films. Moreover, films with different percentages of MWCNT balanced the final pH value which is useful for biomedical engineering applications. Different parameters such as temperature have shown to affect the pH of CS [130]. For this paper, the experiments were done at 37°C since we are mostly interested in biomedical applications of the films.

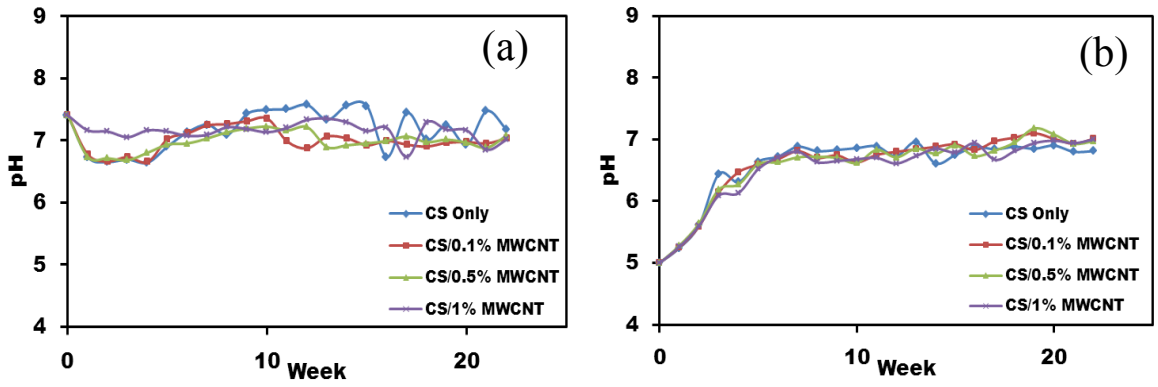

Figure 4-7: pH value changing of CS/MWCNT films with (a) initial pH value of 7.4, (b) initial pH value of 5.

4.4.5 Injectability and viscosity

For potential clinical application as injectable biomaterial, an acceptable injectability and viscosity is necessary. In this part of the experiments, relatively low injection speed was applied in order to allow the fluid to exhibit Newtonian flow. Based on Hagen-poiseuille equation [109, 131], viscosity of the fluid can be obtained by injection test. Figure 4-8(a) shows the injection test results for different concentrations of MWCNT dispersed into CS matrix. Normally, the force exerted to the syringe plunger during the injection process is dissipated in the following ways: (1) prevailing the resistance force of the syringe plunger. (2) transferring energy to the liquid, and (3) extruding the liquid through the needle [132]. After the applied force reached the required value to overcome the sum of the forces, the graph demonstrated a constant value, which was used to calculate the fluid viscosity.

Figure 4-8(b) presents the effect of MWCNT percentage on the solution viscosity. Adding 1% MWCNT into CS solution increased the viscosity by 15%. Based on Figure 4-8, adding up to 0.1% MWCNT did not have a remarkable effect on the ultimate magnitude of applied force and subsequently the viscosity. However, by increasing the percentage of MWCNT, the required injection force was also increased showing higher viscosity of the samples. This can be explained as the effect of interaction between CS/MWCNT solution and the syringe wall. Carbon nanosized particles and tubes are prone to attach to the syringe and needle walls due to the Van der Waals interaction forces.

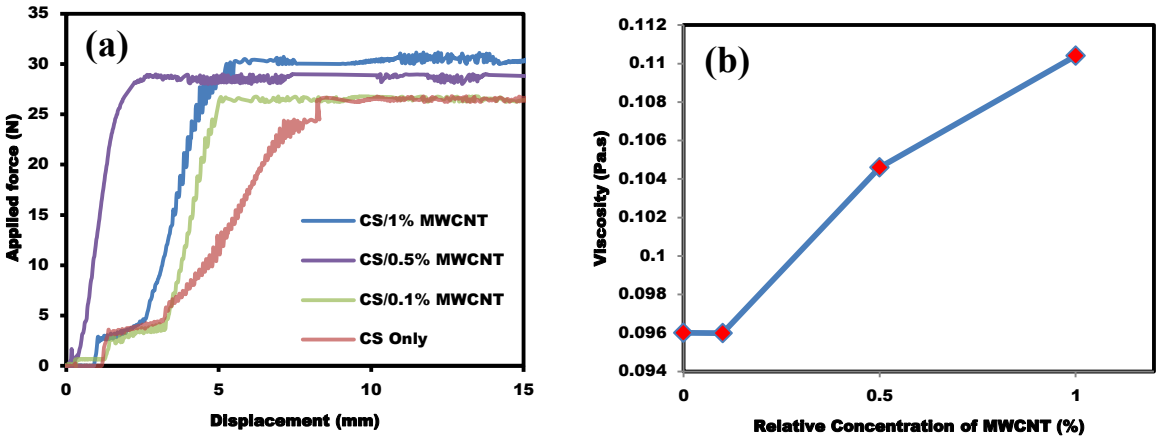

Figure 4-8: (a) typical injection curves obtained for CS/MWCNT pastes with different percentages of MWCNT. (b) Relationship between viscosity and MWCNT concentration.

4.4.6 Tensile and microhardness tests

To investigate the effects of incorporating MWCNT on the mechanical properties of CS films, tensile test was done at room temperature. Typical stress-strain curves for

CS/MWCNT films are shown in Figure 4-9(a). As shown in this figure, the presence of MWCNT in CS matrix significantly enhanced the mechanical properties. All four samples showed mostly brittle behavior since yield strength and ultimate strength were not clearly distinguished.

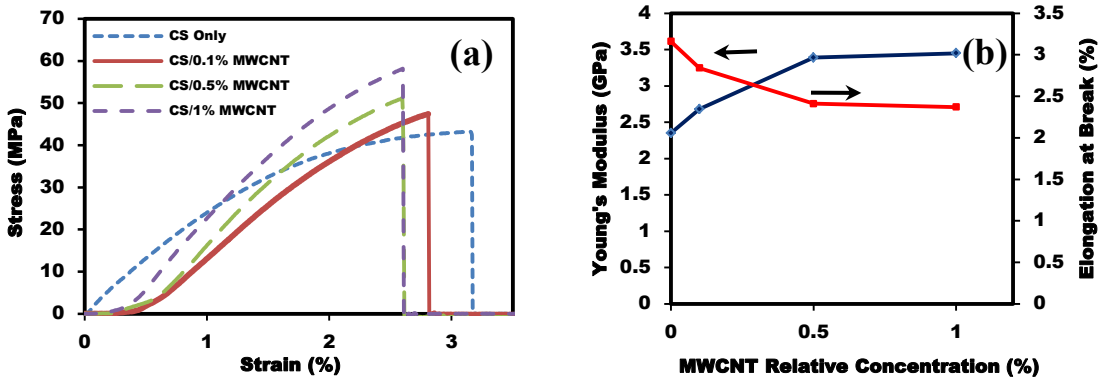

Figure 4-9: (a) Tensile test of CS/MWCNT films. (b) The effect of MWCNT concentration on Young's modulus and ductility of samples.

As shown in Figure 4-9(b) the elastic modulus and tensile strength of the CS film increased with the increase of MWCNT loading. For instance, by adding 1% MWCNT into the CS matrix, the elastic modulus and tensile strength increased by about 47% and 33%, respectively. However, as shown in Figure 4-9(b), by increasing the percentage of MWCNT in CS films, the elasticity and elongation at break decreased. As an example, CS films with 1% MWCNT had 33% more rigidity (i.e. less elongation) in comparison with neat CS films. Another interesting point perceived from this figure is adding 0.1% MWCNT induced drastic improvement in mechanical properties of CS films. However, due to the MWCNT aggregation at higher percentage, with further MWCNT

concentration increase, elastic modulus and tensile strength only increased slightly. This observation is in agreement with other similar studies [112, 133]. Noted in the referred article, higher CS concentration resulted in films with more flexibility (i.e. higher percentage of elongation at break) and lower elastic modulus.

Improving mechanical properties of CS films in the presence of MWCNT can be attributed to the interaction of MWCNT as the reinforced fibers and CS as the matrix. Due to the strong interactions between CS and MWCNT, higher energy was needed to overcome the molecular bonding energy and subsequently, elastic modulus and tensile strength increased. Nevertheless, after reaching certain energy, nanocracks started initiating at the MWCNT and CS boundary, finally resulting in the failure of films in tensile test at lower elongation. Moreover, with increasing the percentage of MWCNT, the statistical chance of having nanocracks at the boundary of MWCNT and CS increased. In this way, further increase of MWCNT did not demonstrate significant improvement in tensile strength and elastic modulus.

Microhardness tests were performed at the lowest possible load and the maximum indentation depth was 10% of the total film thickness to minimize the substrate effect [134]. Ten different locations were examined and the average value of hardness at 10 gf is shown in Figure 4-10.

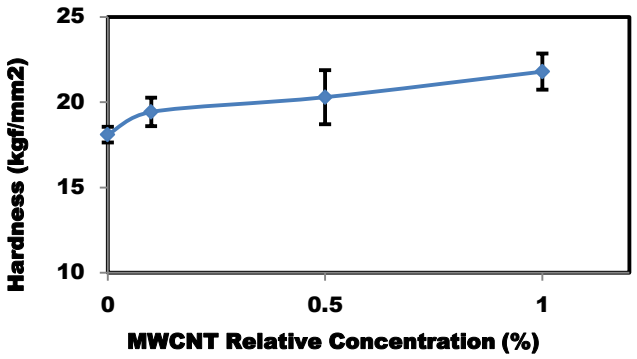

Figure 4-10: microhardness of CS/MWCNT films at 10gf load as a function of MWCNT concentration.

Dispersing MWCNT into CS matrix hardened the CS film surface. Carbon and its derivative such as CNTs are one of the most rigid and hard materials [135], and adding small percentage of MWCNT can induce hardness to the CS films. In another point of view, having harder material means lower deformability and elasticity, which is in agreement with tensile test. For example, adding just 1% MWCNT, can increase the surface hardness up to 20%.

4.4.7 CS/MWCNT film cytotoxicity

To evaluate cell proliferation and film cytotoxicity, Live/Dead cell assay was employed to investigate the cell viability of the CS/MWCNT films. This assay has the benefit of simultaneous detection of live and dead cells. Green fluorescence from calcein dye binded to the active esterase in healthy cells, and red fluorescence from EthD-1 interconnected to nucleic acids of damaged membranes of dead cells. Two time points (i.e. day 3 and day 7) were selected to study cell behavior as stated earlier.

Osteoblasts were used to examine the film-induced cytotoxicity. Overall, osteoblasts adhered strongly to CS/MWCNT films and showed normal morphology over 3 and 7 days, indicating nontoxic effects of MWCNT to the osteoblasts. After 3 days of cell seeding, as observed from Figure 4-11(a), cells proliferated and attached to the all kinds of film surfaces and the viability percentage was high, showing cell-friendly property of the films. At this time point, majority of cells were not completely elongated and did not demonstrate well-distributed morphology. Some parts of the figures are not clear and vivid due to the rugged and scaly morphology of the films in micrometer scale. Moreover, the approximate circular shape of cells altered to elongated structure after 7 days and they started proliferating (Figure 4-11(b)).

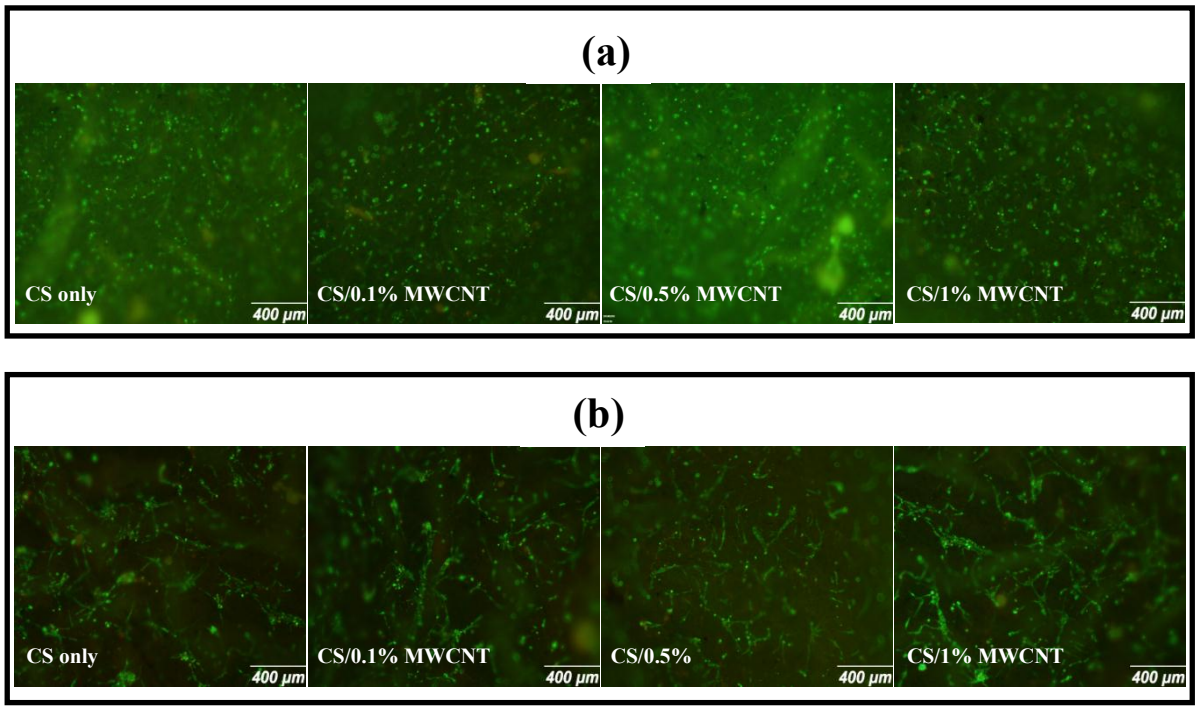

Figure 4-11: Fluorescence microscopy images of osteoblasts (a) after 3 days and (b) after 7 days treated with Live/Dead assay.

Maximum diameter of a single elongated cell was 75 µm, and they aggregated and created big cell colonies as shown in this figure. Randomly aligned cells were observed in most of the samples. This can be attributed to the surface swelling on the samples. Swelling of the surface was not perfectly uniform and resulted trapping cells in the surface micro grooves and elongating them in the specific direction. The fraction of dead cells to the total number of attached cells was negligible. This confirmed that MWCNT is not toxic for osteoblasts as reported in literature [136].

4.5 Conclusions

This research investigated the structural, optical, mechanical, and biological properties of CS/MWCNT nanocomposite films. By applying a simple fabricating method, we obtained homogeneous dispersion of MWCNT in the CS matrix. Adding low percentages of as-prepared MWCNT had significant effects on optical, mechanical properties and bonding energy of molecules. For instance, adding just 1 wt% of MWCNT to CS matrix can enhance the tensile elastic modulus and tensile strength by about 47% and 33%, respectively. In addition, the added amount of MWCNT, using two different initial pH values, was demonstrated to not highly affect the polymer crystal structure and pH level of samples. We have also studied the ability of osteoblasts to attach and proliferate on the CS/MWCNT at two selected time points. No cell toxicity effects were observed at days 3 and 7. In summary, we showed that the CS/MWCNT nanocomposite films with improved mechanical and bioactive properties are well suited as a novel biomaterial. MWCNT incorporated into CS film increased the viscosity of CS solution, which may be useful for injecting low viscous CS pastes.

Chapter 5

Measuring Mechanical Properties of Human Amniotic Fluid Stem Cells Using Nanoindentation

5.1 Abstract

The aim of this study was to obtain nano mechanical properties of living cells focusing on human Amniotic Fluid Stem (hAFS) cell using nanoindentation techniques. We modified the conventional method of AFM in aqueous environment for cell imaging and indentation to avoid inherent difficulties. Moreover, we determined the elastic modulus of murine osteoblast (OB6) cells and hAFS cells at the nucleus and cytoskeleton using force-displacement curves and Hertz theory. Since OB6 cell line has been widely used, it was selected to validate and compare the obtained results with the previous research works. As a result, we were able to capture high resolution images through utilization of the tapping mode without adding protein or using fixation methods. The maximum depth of indentation was kept below 15% of the cell thickness to minimize the effect of substrate hardness. Nanostructural details on the surface of cells were visualized by AFM and fluorescence microscopy. The cytoskeletal fibers presented remarkable

increase in elastic modulus as compared with the nucleus. Furthermore, our results showed that the elastic modulus of hAFS cell edge part (31.6 kPa) was lower than OB6 cell edge (42.2 kPa). In addition, the elastic modulus of nucleus was 13.9 kPa for hAFS cell and 26.9 kPa for OB6 cells. Differences in cell elastic modulus possibly resulted from the type and number of actin cytoskeleton organization in these two cell types.

5.2 Introduction

Finding mechanical properties of biological samples, especially living cells, has been of great interest to researchers. Analysis of cellular mechanical properties can lead us to discover new methods of identifying various forms of cancers [14, 15, 137] and other diseases [138]. In tissue engineering, probing the elasticity and adhesion of live cells can provide physical insight into the mechanical and chemical properties of biomaterials and scaffold materials [139]. Many methods including magnetic twisting cytometry, traction force microscopy, micro pipette aspiration, optical trap, optical stretcher, micro and nano needle insertion and AFM have been used to find the mechanical properties of cells [16, 140]. Compared to the other methods, AFM indentation has become the principal technique in measuring the cell mechanical properties of surface layers and especially cells with high spatial precision [19, 141]. Although there are some limitations in using AFM for the measurement of cell mechanics such as lateral drag of the cell by the tip, the calibration [142] and not ideally sharp probes [143], this method is the most widely used.

The elastic modulus of a living cell is usually calculated by producing force-displacement curves with data from indentation tests. The common analysis models for cell indentation are based on the Hertz theory [144, 145]. This model is based on

perfectly elastic behavior of cells during indentation [146]. In the application to the AFM measurements, the generally considered indenter's geometries are the conical and spherical ones. Although nanoindentation is widely used to investigate the stem cell mechanical properties [147], but these properties for some new types of stem cells have not yet been fully discovered.

In last few decades, main advancement has been facilitated by the discovery of stem cells, capable of converting to various cell lineages. Stem cells have been isolated from embryonic, fetal, and adult tissues and more recently, also from umbilical cord, placenta and amniotic fluid. Among the source of stem cells that have been studied, human Amniotic Fluid Stem (hAFS) cells have arisen as an attractive source of stem cells since 2007 [148], as its procurement does not raise the ethical concerns associated with the use of human embryonic stem cells [149-151]. In addition, hAFS cells have the advantage of being primitive cells with little known antigenicity and great expansion capabilities. These cells can be induced to differentiate into cells that represent each germ layer, such as adipogenic, osteogenic, myogenic, endothelial, neuronal, hepatic, and chondrogenic lineages [152, 153]. hAFS cells are becoming an important source of cells for regenerative medicine and tissue engineering. In this way, it is necessary to characterize its mechanical properties. In other words, although hAFS cells have many properties that support their clinical usefulness [154], little is known about the mechanical properties.

In this study, the aim was to determine the mechanical properties of hAFS cells and compare it to murine osteoblast (OB6) cells as a reference using AFM imaging and indentation with the Hertz model. Specifically, we chose OB6 cells as a reference cell source since our laboratory focuses on OBs for the bone regeneration studies. The OB6

cells are well known cells with the previously known mechanical properties [147, 155] to verify the result of current technique and discuss the possible source of differences with other papers. Both nucleus and cytoskeleton play an important role in cell deformation and mechanical properties. Thus, indentation was done at nucleus and cytoskeleton regions of the cells. The tapping mode was used for cell imaging in physiological aqueous environment without using fluid cell or any other specific equipment. In addition, this physiological aqueous environment provided advantage of tapping mode without requiring adhesive proteins to attach cells on the substrate. In addition, images obtained from AFM were compared with fluorescence microscopy images to verify the viability of cells used for AFM studies. Generally, there were two aims in this paper. First, a new and simple technique of imaging and indenting for living cells in tapping mode was introduced. Secondly, the elastic modulus for hAFS cells, as an attractive new stem cell source, was determined using the above technique and validated using OB6 cells.

5.3 Materials and methods

5.3.1 Materials

The hAFS cells (passage 21) were kindly provided by Wake Forest Institute for Regenerative Medicine (Winston-Salem, NC, USA). Chang media containing 66% alpha minimum essential medium (α-MEM) (GIBCO), 18% Chang Medium B (Irvine Scientific), 2% Chang Medium C (Irvine Scientific), 15% Fetal Bovine Serum (FBS) (GIBCO), and 1% Pen Strep (GIBCO) were used to prepare cell culture medium. OB6

cell vials were received from Dr. Lecka Czernik at the University of Toledo. 90% α-MEM plus 10% FBS and 1% penicillin-stereptomycin were used to culture the cells. A LIVE/DEAD cell assay kit (Invitrogen) was used to identify cell viability and morphology. To prepare AFM samples, microscope slides with 1 mm thickness (Fisher Scientific) were used.

For consistency, we applied the same preparation procedures for both types of cells. Small pieces of microscope slides (1 cm X 1 cm) were cleaned with ethyl alcohol and deionized water and kept under UV light for 90 min. Approximately 10,000 cells were counted by a hemocytometer after trypsinization from the original plate and plated into 35 mm petri dish filled with small pieces of sterilized microscope slides. The petri dish was incubated (37^0C, 5% CO_2) for 36 h before experiment.

5.3.2 Instruments

AFM indentation testing and imaging were performed with a commercial instrument Veeco Multimode with nanoscope V Controller with J scanner. The maximum Z range for this scanner was about 6 μm which is usually higher than the maximum height of cells [156-158]. The NanoScope software V6.13 was used to control imaging and testing parameters. In this experiment, cantilevers B and D from probe SNL-10 (Bruker Co.) were used with a spring constant of 0.12 N/m and 0.06 N/m, respectively. The tip half-opening angle was assumed to be 25° from the specifications of the manufacturer. This sharpened probe is suitable for performing experiments in both air and fluid while applied load is in a range of a few nanonewtons for better resolution [143, 159]. Fluorescence microscopy (Olympus, FSX100) was used to obtain cell images when cells

were treated as the LIVE/DEAD cell as previously described in detail [10]. Data was statistically analyzed with one-way ANOVA. $p < 0.05$ was considered as statistically significant.

5.3.3 AFM imaging and indentation test

To perform the AFM test, a small piece of microscope slide covered by cells was attached to a conductive metal plate on top of the AFM scanner. In order to minimize the viscosity effects, low scanning speed of 1 Hz was used for imaging [160, 161]. By indenting slowly enough, the viscous contributions will be very small [162]. Then, the force measurements will only be demonstrated by the elastic behavior of cell. In the first series of experiments, we tried to apply AFM contact mode in air and fluid using fluid cell to obtain better resolution. However, due to the lack of strong adhesion between cells and microscope slides, the cells were detached and the test could not be conducted completely as expected [163]. Furthermore, air bubbles were a problem as they sit on the cantilever when fluid cell is used as expected from literature [164]. Figure 5-1 was captured in air using the contact mode. After some tip tracing-retracing movement, cells were detached from the glass substrate due to the low adhesion forces.

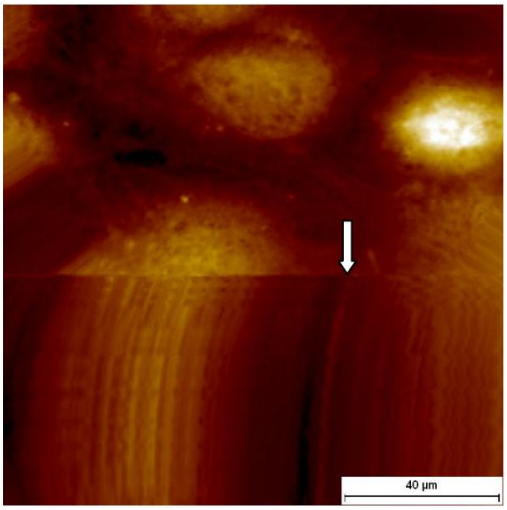

Figure 5-1: Detachment of OB6 cells observed during imaging with the AFM contact mode. The arrow shows cell detachment line induced by the tip motion.

In the next step, as schematically shown in Figure 5-2, the culture medium was injected on the cell surface by using small syringe needle. A drop of culture medium covered the entire cell and cantilever. By applying this modified technique, cells were attached to the glass due to the adhesion force between the small drops of the culture medium and glass surface. Cell attachment to the surface is vital for cell survival and growth [165, 166]. Therefore, all parts of the experiment were completed within 1-2 h before cells started to die and detach from the small pieces of the glass slides [17, 167, 168]. By using a force mode modulus, an indentation with low applied loads was done on the surface of the cell to obtain its elastic modulus with the Hertz model. The AFM indentation experiment required monitoring the deflection of the cantilever probe as it indents the cell surface. The resulting interaction force bends the cantilever, which is detected by the motion of laser spot reflected off the back of cantilever onto a four-quadrant photodetector. For each kind of cell, the indentation test was done for at least 20

times. Before plotting a force indentation curve, the sensitivity of the AFM cantilever should be calculated. Thus, we indented a glass substrate using a same tip. Glass is comparatively hard enough to be considered as a rigid substrate.

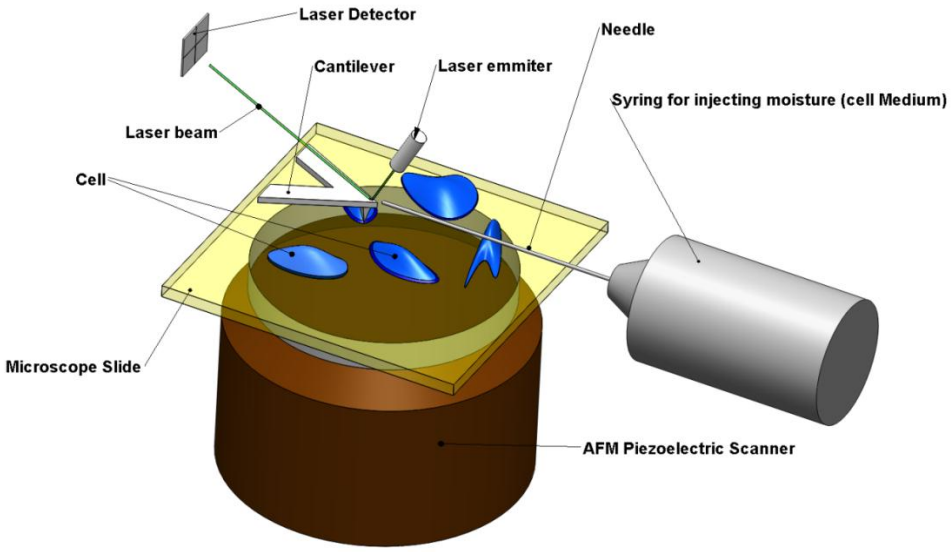

Figure 5-2: Test setup configuration for AFM imaging and indentation. During the imaging and indentation, the moisture was continuously injected to the surface.

5.3.4 Analysis of data

A simple model of quantifying the elastic response of materials is based on the Hertz model which has been frequently used in previous cell study works [169-171]. The Hertz model predicts the samples elastic modulus with the assumption of perfectly elastic behavior and indenter shape of a rigid sphere or cone. Regarding to the conical shape of

the tip used in this set of experiment, the equation relating force and depth for indentation with a cone is given by:

$$F = \frac{2}{\pi} tg\alpha \frac{E}{1-\upsilon^2} \delta^2 \quad (1)$$

In this equation, F is the load exerted by AFM tip, E is the Young's modulus of the cell, α is the half opening angle of cantilever tip and υ is the Poisson's ratio. Usually, $\upsilon = 0.5$ is assumed for cells and other perfect elastic materials [172]. Thus, cells are considered as an incompressible material.

5.4 Results and discussion

5.4.1 Cell imaging and characterization

Figure 5-3 shows fluorescence microscopy images of hAFS and OB6 cells. Live and healthy cells were stained as green. Investigation of the hAFS cells morphology showed distinct regions. hAFS cells were well-elongated in one direction as expected [173, 174] and the length of cells were normally longer than 200 μm. hAFS cell area was significantly larger in compare with OB6 cell.

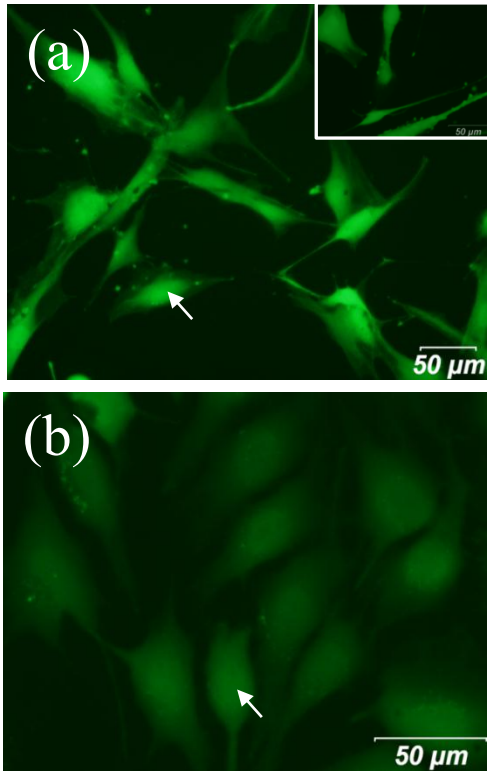

Figure 5-3: (a) Morphology of hAFS cell, (b) OB6 cells, treated with LIVE/DEAD cell assay. Arrows show the cells nuclei. Different parts of cells such as filaments, microtubes and nucleus are visible.

Microtubules and filamentous structures spread out over hundreds of micrometers prevented the capture the image of a whole hAFS cell because the maximum length that can be covered by AFM scanner was 100 µm (Figure 5-4(a)). In addition, the cell nucleus has been identified with an asterisk (*) in this figure. Figure 5-4(b) demonstrates the height distribution of the cell along a line that is shown in Figure 5-4(a). By comparing the height profile of two cells (*a* and *b*) shown in Figure 5-4(a), it was clear that by increasing the distance from the nucleus, the cytoskeletal height of the cell decreases. Detailed cytoskeletal fiber height is shown in the sub-figure of Figure 5-4(b). These

cytoskeletal filaments play an important role in measuring the mechanical properties of cells [158]. There were less than 10 filaments in a certain direction. According to this graph the approximate fiber height was around 50 nm. Generally, the nucleus portion of the cell constitutes its highest part [175]. The approximate height of the hAFS cell nucleus was between 1 to 2.7 µm obtained by AFM.

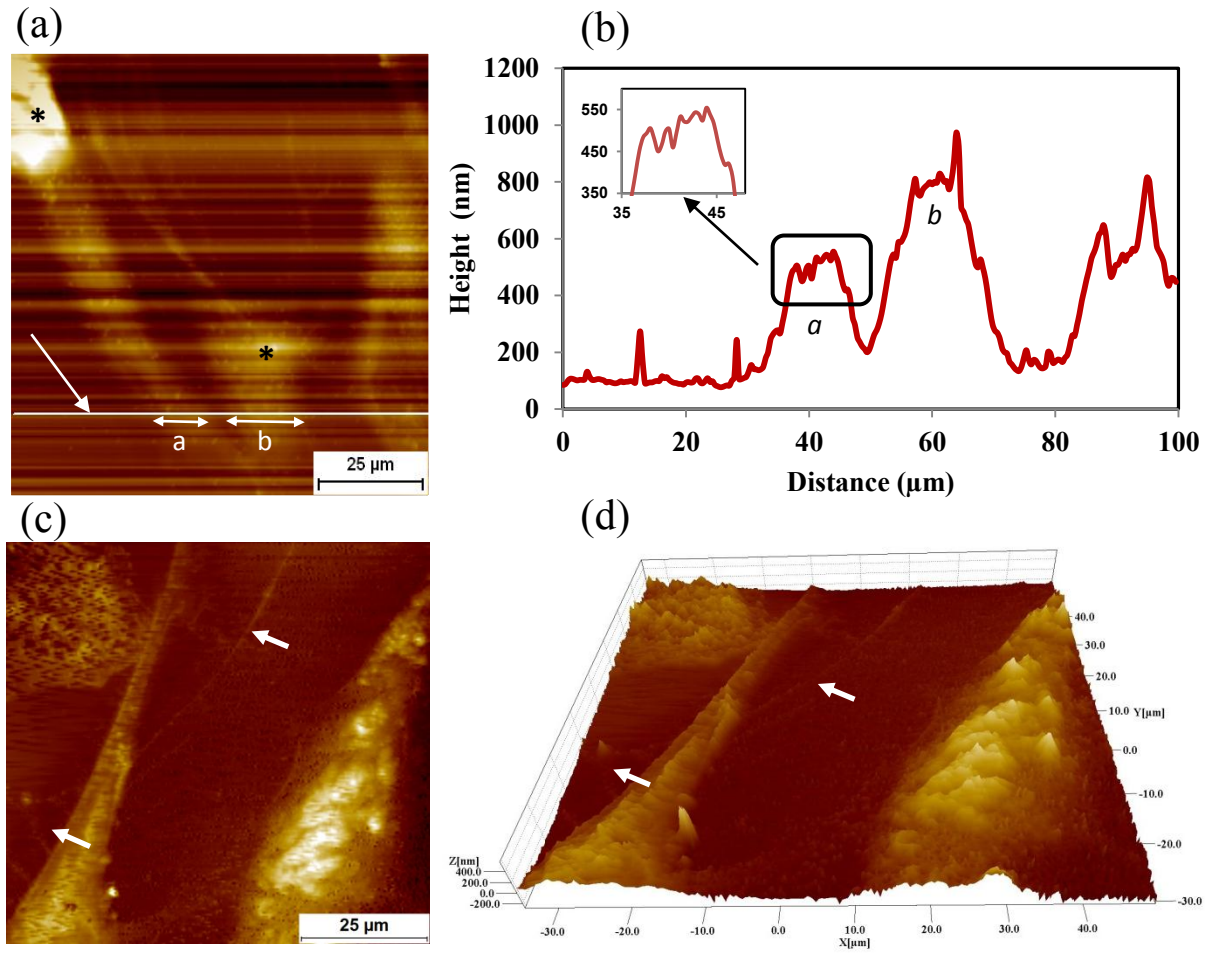

Figure 5-4: (a) structural morphology of hAFS cells plated upon glass slides after 36 hours, (b) Height profile of the cell cytoskeleton throughout the indicated line, (c) cytoskeleton structure of hAFS cell, (d) 3D image of hAFS cell. In two last figures, the discrete actin filaments are shown by arrows.

Two elongated hAFS cells are shown in Figure 5-4(c) obtained from AFM. Actin filaments and nucleus are visible in this figure. Thin and long actin filaments were also separately formed as indicated by arrows in this figure. In Figure 5-4(d), the three-dimensional image of Figure 5-4(c) is presented. The average height for the nuclei was estimated around 1.3 μm for this cell which was the maximum thickness and height in the cell. In addition, the morphology of cells obtained with AFM imaging was consistent with fluorescence microscopy images asserting cells were alive during the AFM test and the morphology has not been changed.

In tapping mode, taking good images is usually more difficult than contact mode [176]. Although no external adhesive proteins or fixation methods were used to adhere cells to the glass, cells did not detach through AFM tapping mode. This was due to the injection of culture medium during the experiment. In this method, cell and tip were occupied by the big drop of cell culture medium which reduced the effect of capillary forces [177]. The same method was applied for OB6 cells. Figure 5-5 demonstrates the cytoskeleton height of OB6 cells in two paths within the same cell. Path 1 was selected closer to the cell nucleus in compare with path 2. The average cell height in this path was larger than path 2 which means that as we get closer to the cell nucleus, the cell height increases and nucleus part was the highest cell part in both kinds of cell. The height of OB6 nucleus varied from 1.5 to 3.5 μm. OB6 cells had more actin filaments than hAFS cells. For OB6 cells, filaments had less height compared to hAFS cells and were more scattered. In other words, the filaments of one OB6 cell were distributed over approximately 25 nm while in hAFS cells the cell filaments were distributed over 10 nm.

The data obtained in this part is in agreement with Simon et al. (2003, 2004) papers, despite the fact that they used human bone marrow stromal cells.

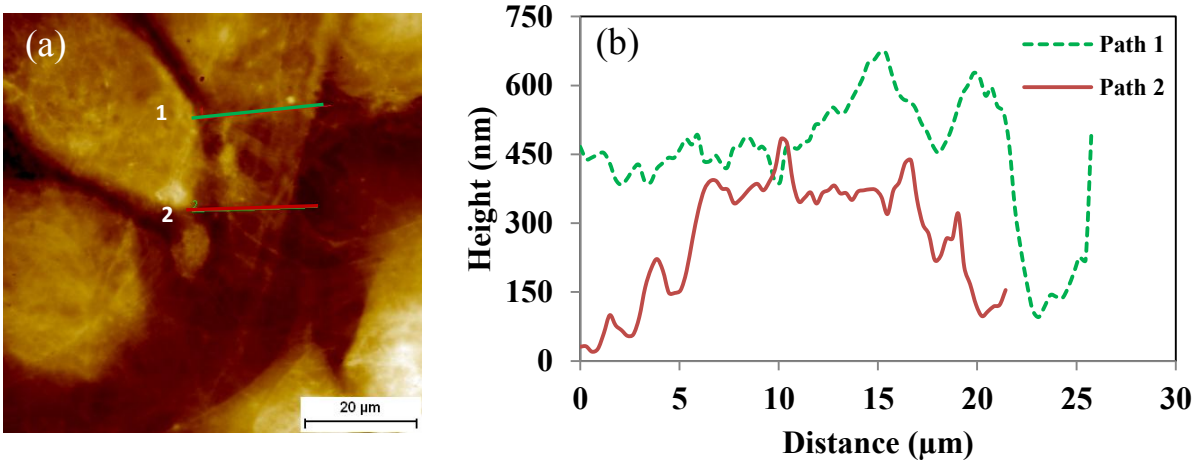

Figure 5-5: (a) Structural morphology structure of OB6 cells plated on glass slides after 36 hours, (b) height profile of cell cytoskeleton along two indicated path lines.

5.4.2 Cell mechanical properties

Cells are soft and considered as the elastic materials under small loads and AFM indentation of live cells does not present evidence of cell plastic deformations. This is the main reason that usually very low force (~nN) is applied to the cell surface in order to obtain elastic modulus. A concern during the cell indentation experiment is to minimize the effect of glass substrate on force-displacement curves. To compensate for this, indentation depths are tried to be equal or less than 15% of the cell height [178, 179]. In addition, we performed indentation tests at nucleus and cytoskeleton of cells. Based on our findings, at the nucleus, cells were thicker than the other parts. Another property of engaging indentation upon the nucleus is that the cytoskeletal structure is more

homogeneous than the other parts of cell [180]. Figure 5-6(a) shows a schematic force-indentation curve of the nanoindentation experiment. As expected from the literature [181, 182], adhesion jump occurred in both kinds of cells due to the adhesion. For hAFS cells this jump is higher than OB6 cells.

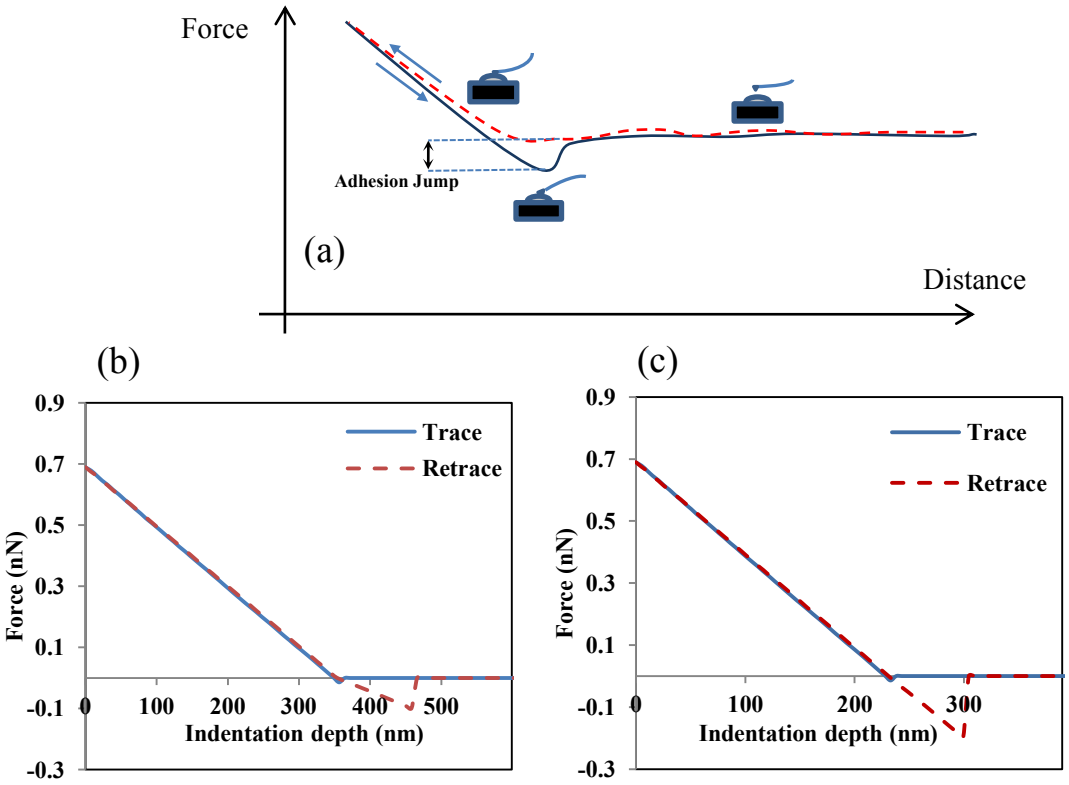

Figure 5-6: (a) Schematic figure of force-indentation curve, typical force-indentation curve for (b) hAFS cell and (c) OB6 cell.

Furthermore, Figure 5-6(b) and 5-6(c) demonstrate a typical force-indentation curve for hAFS and OB6 cell nucleus indentation, respectively. At almost similar loads, indentation depth for hAFS cells was greater than OB6 cells (approximately 1.6 times) and led to the lower elastic modulus based on the Hertz equation. Loading-unloading

curves almost overlapped. This observation is in agreement with previous works [167, 169, 183, 184].

All applied forces were between 0.6-0.9 nN depending on the cantilever used. The narrow load range is due to the small changes in sensitivity and spring constant of the AFM tip during the indentation test and the two different tip spring constants. Comparison between elastic modulus of hAFS cells at nucleus and cytoskeleton revealed Young's modulus at edges consisting actin filaments and microtubes were almost double than the nucleus. It has been well established that the actin fibers promote overall cellular elasticity [180, 185].

Final results of elastic modulus are shown in Figure 5-7. Cell population properties were well described by log-normal and Gaussian distributions. Both functions predicted approximately same value for elastic modulus of each case. Based on Gaussian fit, average elastic modulus of hAFS cells was 32.9±3.66 kPa at the cytoskeleton region and 13.9±2.25 kPa at the cell nucleus. Additionally, the average elastic modulus of OB6 was 26.9±3.41 kPa at nucleus region and 42.8±3.44 kPa for cytoskeleton. These values were in range of elastic modulus previously reported for cells [16]. Based in the presented results, significant difference ($p<0.05$) was observed in the elastic modulus of nucleus and cytoskeleton for both kinds of cells.

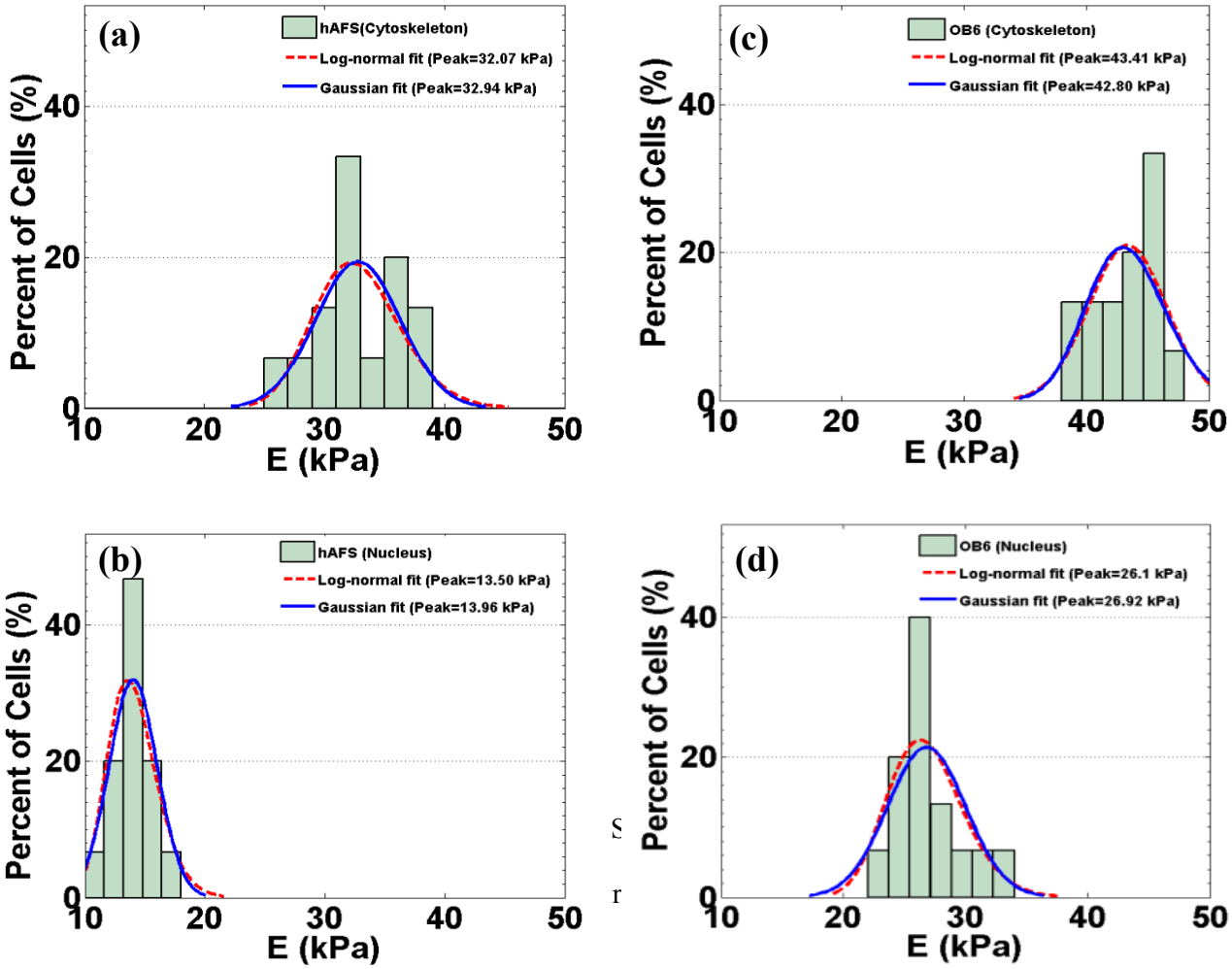

Figure 5-7: Young's modulus distribution of hAFS cells (a) at cytoskeleton region, (b) at nucleus region, and for OB6 cells (c) at cytoskeleton region, (d) at nucleus.

Although some papers reported the same range values of elastic modulus for cells [186, 187], some of the previously published investigations showed significantly lower elastic modulus [147, 188, 189]. For instance, the average reported value for murine osteoblast cells is 14 kPa at cell nucleus [155] which shows a significant difference with the present results. This discrepancy reflects intrinsic differences among both cell lines and experimental setup. The main reason can be attributed to variations in methodology.

For instance, the spring constant of the cantilever and the applied force [50, 59] impress the obtained Young's modulus value. Furthermore, the method of testing has remarkable effects [190]. It has been demonstrated that [191] culture conditions has a great influence on elastic properties of cells and composition of the growth medium can activate or deactivate certain proteins which subsequently promote focal adhesions and actin stress fiber formation that effect the overall cell elasticity. Moreover, it has been shown that stress relaxation (i.e. viscoelastic properties) of cells before AFM indentation has a great effect on the elastic modulus and a modified Hertz model (Thin-layer model) can be applied to describe the behavior [192]. The other factors are the indentation depth [193, 194] and AFM tip size/shape [195]. Elastic modulus obtained based on small indentation depths is described as the regions rich in actin filaments while for large indentation depths, the modulus represents the stiffness of a whole cell which is usually lower than actin filaments network. In addition, using different shape and size of AFM tips has a significant effect on elastic modulus. Using sharpen AFM tip in this study would be another source of difference with some other published papers. Nanosized tips can sense actin filaments, mitochondrion and microtubules with higher elastic modulus of the cell average while with using microsized tips touch the bigger area containing different parts of cells and the obtained elastic modulus is the average of the cells part under neat of the tip.

5.5 Conclusions

The goal of this paper was to find the elastic modulus of hAFS cells as a novel source of stem cells and compare its mechanical properties and cell morphology with OB6 cells

as one of the widely used cell lineage. In addition, we presented a new method for cell imaging and indention in an aqueous environment. In the new method, we tried to eliminate the inherent concerns of current method of cell imaging and indentation. Our results displayed that hAFS cells were well-elongated cells at the selected time point and their nucleus height were lower than OB6 cells. Moreover, OB6 cells demonstrated higher number of filaments in comparison with hAFS cells.

Using Hertz model, the elastic modulus of hAFS cells was reported to be double at the cytoskeleton part compared with nucleus region. Furthermore, the highest elastic modulus was obtained for OB6 cytoskeleton and the lowest one was for hAFS cell nucleus. However, there are several parameters that can affect the elastic modulus values and further investigations need to be done to verify the current results. Based on the presented results, the elastic modulus of hAFS cell is 32.9±3.66 kPa and 13.9±2.25 kPa for cytoskeleton and nucleus regions, respectively. Our results showed OB6 elastic modulus is 42.8±3.44 kPa at cytoskeleton region and 26.9±3.41 kPa at nucleus region.

Chapter 6

The Effect of Graphene Substrate on Cell Adhesion and Proliferation

6.1 Abstract

Understanding the effect of graphene substrate on graphene-cell interaction is important for considering graphene as a potential candidate for biomedical applications. In this paper, biocompatibility of few layers of graphene film transferred to different substrates was evaluated using osteoblasts. The substrates were oxidized silicon wafer (SiO_2/Si stack), soda lime glass and stainless steel. Chemical vapor deposition method was employed to synthesize graphene on copper substrate using methane and hydrogen as precursors. The quality and the thickness of graphene films on different substrates were estimated by Raman spectra, whereas the thickness of graphene film was confirmed by reflectance and transmittance spectroscopy. The study was also focused on cell attachment and morphology at two time points. The results show that graphene does not have any toxic effect on osteoblasts. The cell adhesion improves with graphene coated substrate than the substrate alone. It seems that graphene substrate properties play a

dominant role in cell adhesion. The results of this study suggest that a layer of graphene on bone implants will be beneficial for osteoblast attachment and proliferation.

6.2 Introduction

Graphene has become a promising and attractive material in different engineering fields due to its unique properties [196-198]. Graphene sheet is a single-atom thick layer of sp^2 bonded carbon atoms forming a hexagonal 2D lattice [199]. The topography of single layer graphene is simple. In addition, recent achievements in chemical vapor deposition (CVD) synthesis have let the graphene coated on different material substrates after the successful synthesis on copper foil by Ruoff research group in late 2009 [200]. Another advantage of CVD synthesis of graphene is that the pure form and large flakes of graphene are reachable which is vital for biological tests. The research on biomedical applications of graphene has seen dramatic progress and yet mostly in its beginning stage [201]. Since 2008, researchers have started investigating the potential biomedical applications of graphene [202] and a lot of interesting works have been carried out to explore the use of graphene and its derivatives such as graphene oxide in biomedical applications [203]. These applications range from drug/gene delivery [204, 205], biosensors [206] and biocompatibility to antibacterial effects [207].

Cell biocompatibility is an initial requirement for the use of graphene in biological applications [208]. Although most of the papers have reported that graphene has some positive effects on cell adhesion, proliferation and differentiation [209-211], some scientists have demonstrated that certain form and derivatives of graphene would induce significant cell toxicity [212-214] which is useful for anticancer activities. Cell adhesion

is a critical factor for other subsequent cell functions such as proliferation and formation of mineral deposits. Adhesion is greatly dependent on cell number, time, cell–material interface and surface topology [209].

Recently, the effects of some other parameters in graphene–cell interaction have been investigated [215-217]. It has been reported that an unusual behavior of human osteoblast was observed in the presence of graphene on SiO_2/Si substrate with the initial presence/absence of fetal bovine serum (FBS) [215]. It was also demonstrated that oxygen and hydrogen treatment influenced the attached cell size. The sizes were larger on the hydrogen treated graphene synthesized by CVD [216]. Ryoo et al. [217] showed that graphene improves gene efficiency, focal adhesion and proliferation of fibroblast cells. Although some few recent papers have investigated the effect of graphene on different scaffold materials [218, 219], the effect of graphene substrate has not yet been completely discovered.

Biomaterials ranging from soft to hard, polymer to metal are available for diverse applications [220]. One of the main challenges of using biomaterials is to improve cell attachment and proliferation. A layer of graphene with its outstanding mechanical properties coated on a biomaterial as a substrate can be a promising candidate for cell adhesion and proliferation enhancement. This novel idea is appropriate in bone tissue engineering and other related fields. Next generation of bone implants with graphene coated layers would have better cell attachment properties which could drastically decrease the bone healing time.

In this research, three different substrates, namely soda lime glass, silicon wafer and stainless steel were selected to study the cell attachment and proliferation of osteoblasts.

Graphene film was synthesized on copper foil by CVD method and subsequently transferred to the substrates [221]. Cell attachment and proliferation study were done at day 2 and day 5. Our results showed that graphene substrate greatly affected the behavior of osteoblasts and improved cell attachment in selected time points.

6.3 Experimental details

6.3.1 Synthesis and transfer of graphene films to desired substrates

For all three substrates same graphene layer deposition procedure was applied. All the chemicals used to fabricate the graphene layer on substrates were reagent grade from Alfa Aesar and used without further purification. Methane (CH_4) and Hydrogen (H_2) gasses for the synthesis of graphene films on a copper foil were received from Air gas. Synthesis of graphene by CVD was carried out on a copper foil (25 μm thick, 99.9995 %, Alfa Aesar) in an alumina tube furnace system under the flow of CH_4 and H_2. The foil was treated with acetic acid under the ambient condition slightly above the room temperature (40°C) before it was subjected into the furnace. Copper foil was heated inside the tube furnace under 150 sccm flow rate of H_2 and Argon (Ar) (10% H_2, 90% Ar) mixture at 950°C for 1 h to allow the copper foil to anneal [222]. This step is necessary for the removal of any native oxide layer left on the surface after the heat treatment with acetic acid around 40°C for 10 min [223]. Graphene deposition was carried out by passing a mixture of CH_4 and Ar (5% CH_4, 95% Ar) for 15 min. The gas composition was changed to H_2 and Ar immediately after the coating process was completed and the system was allowed to return to the room temperature with the cooling

rate of 50°C/min. Transfer of graphene from copper to a desired substrate was carried out by a wet etching process. The details about the typical transfer processes employed in this work have been explained elsewhere [223]. Figure 6-1 shows the schematic representation of the entire process for silicon wafer substrate.

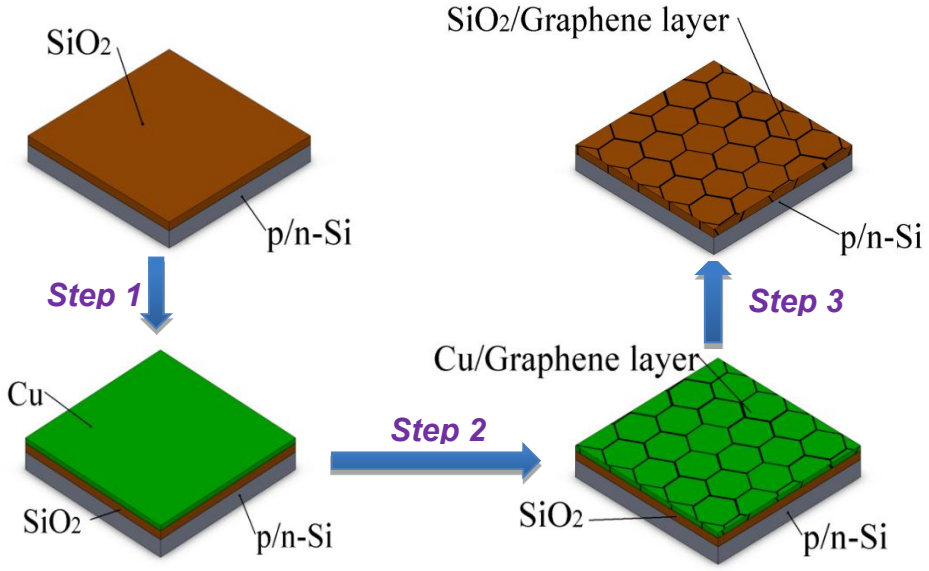

Figure 6-1: Schematic illustration of the synthesis of graphene by CVD method. Step 1: copper film was vapor deposited on Si/SiO2 substrate by metal evaporation, Step 2: Synthesis of graphene was carried out by CVD method, Step 3: removal of Cu was carried out by wet etching of Cu.

6.3.2 Cell culture, proliferation and staining

Soda lime glass, silicon and stainless steel (Grade 302, ASTM A666) substrates with and without graphene coated layers were washed and sterilized under the UV light before placing in the 24-well-plate. Cells with the density of 25,000 cells per well plate were plated on substrates and incubated at 37°C in 5% CO_2 in alpha minimum essential

medium (α-MEM) supplemented with 10% fetal bovine serum (FBS) and 1% penicillin-streptomycin (Pen strep), all purchased from Gibco. The morphology of the adhered cells was characterized by immunofluoresent staining of live cells (Calcein-AM, Invitrogen), dead cells (Ethidium homodimer, Invitrogen) and nuclei (4',6-diami-dino-2-phenylindole (DAPI), Invitrogen).

6.3.3 Instruments

The quality of the graphene films was examined by different optical methods, such as Raman spectroscopy, Scanning Electron Microscope (SEM), optical, and confocal microscopy, reflectance and transmission spectroscopy. The surface morphology was obtained using SEM (Hitachi, S-4800) operating at an accelerating voltage of 20 KV under high vacuum. High resolution images were captured using TCS SP5 multi-photon laser scanning/confocal microscope (Leica Microsystems). The Raman spectra of graphene films were obtained at room temperature with a Renishaw Invia Micro-Raman spectrometer in back scattering geometry with the laser excitation of 632.8 nm at a power level of 1.7 mV. The transmittance of the graphene films on soda lime glass was performed on a UV-VIS-NIR spectrophotometer. The fluorescence Olympus FSX-100 microscope was used to take microscopic images. For each group at each time point three samples were prepared and tested. In order to count cells, ten size-calibrated fluorescence images of Live/Dead stained cell from each substrate were obtained using microscope with a 4X lens. Captured images were analyzed and quantified by using ImageJ software. Statistical analysis was performed using one-way ANOVA and $p<0.05$ was considered as a significantly different data.

6.4 Results and discussion

6.4.1 Raman spectroscopy

The Raman spectroscopy was used to characterize the graphene films transferred to different substrates. Figure 6-2 shows typical Raman spectra of few layer graphene films synthesized in this laboratory on silicon wafer substrate. All other samples have shown approximately the same behavior.

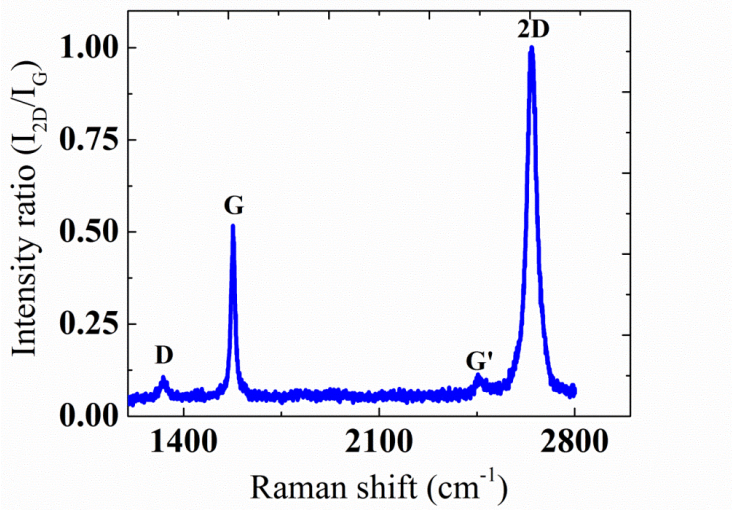

Figure 6-2: A typical as-measured Raman spectra of few-layer graphene synthesized by CVD method. The spectra are normalized to 2D band.

As reported by many researchers about quality graphene synthesis by CVD process, the spectra consist of Raman peaks corresponding to the D band (~1330 cm^{-1}), G band (~1580 cm^{-1}) and 2D band (~2660 cm^{-1}). The D band peak indicated the presence of some defects in the crystal. To investigate the uniformity of the layer, a 2 X 2 cm^2 area of graphene surface was divided into nearly 230 different grids to identify the uniformity of

the surface [222]. The Full Width at Half Maximum (FWHM) mapping revealed that the 2D band was centered ~ 40 cm^{-1} with more than 80% of the data within 35 ± 20 cm^{-1}, while I_{2D}/I_G ratio mapping was centered ~ 1.2 with more than 50% of the data within 1.1 ± 0.8. The mappings indicated that the film mostly consisted of few layer ranging from layers 1-5 [222]. For multilayer graphene, 2D band becomes less Raman active as compared to G band and the broadening of 2D band increases significantly [223]. The intensity of D band relative to G band (I_D/I_G) was found to increase with the increase in number of layers in graphene. Although the intensity ratio increased significantly (~ 0.16 to ~ 0.45), the change in FWHM was not significant (~ 30 cm^{-1} to ~ 35 cm^{-1}) in going from monolayer to bi- and tri-layer graphene for D band. However, the broadening of D band increased significantly after three layers. The intensity of D band seen in the Raman spectra for monolayer graphene was either comparable or relatively less than the intensities reported in the literature [200, 224, 225]. However, its unavoidable presence suggests that the band is Raman active for the graphene synthesized on copper substrate through CVD process. These defects could be associated with the grain boundaries in the copper foils where graphene was initially made. This band also indicated the vacancies and strained hexagonal and non-hexagonal distortions in the film that may have arisen during the process of transfer.

6.4.2 Transmittance spectroscopy

Optical analysis of thin films has always been a useful method to understand the quality of films, thickness, optical properties, and dielectric constants [223]. Figure 6-3 shows the transmittance of the light in the range 200 – 1100 nm for few graphene layers.

For layers 1-3, the transmittance (%) varied in between 85 – 95%. When the sample was equally divided into different grids for the transmittance measurements, the transmittance was found to vary between 78 – 97%, with more than 80% of the data lying within 80 – 90%. The slight decrease in the transmittance for monolayer graphene than theoretical value ($T = (1+0.5n\alpha)^{-2} \sim (1- n\alpha) \sim 97.7\%$; n is a number of layers, α is a fine structure constant) [226] can be attributed to the contamination and mechanical defects produced during the transfer process.

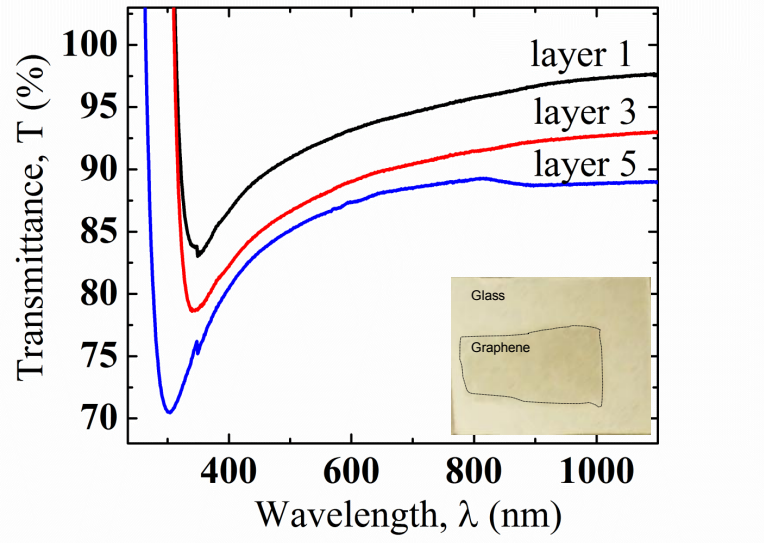

Figure 6-3: Transmittance spectra of graphene layers transferred to glass substrate. Figure in the inset is the comparison of glass with and without graphene layer.

The mechanical defects in graphene due to the process of transfer from copper foil to the desired substrate can be greatly reduced by synthesizing graphene from transfer-free procedure as explained in detail elsewhere [222]. The inserted figure in Figure 6-3 shows the difference in soda lime glass with and without graphene layer. The deposited graphene layer was successfully deposited on a large area of the glass substrate. Glass

coated with the few layer graphene was darker and more opaque due to the absorbance of the visible light by graphene layer.

6.4.3 Surface imaging and visual transparency

Few layer graphene films on silicon wafer and stainless steel substrates was characterized using SEM. Graphene layers completely covered a large area of the substrate. Transferred graphene layer to both substrates (Figure 6-4) exhibited nanoripples with high density and a number of observable wrinkles compared to graphene on glass slide as expected [219]. Also, the surface roughness of stainless steel was higher than silicon wafer and the grinding direction was visible in Figure 6-4(b).

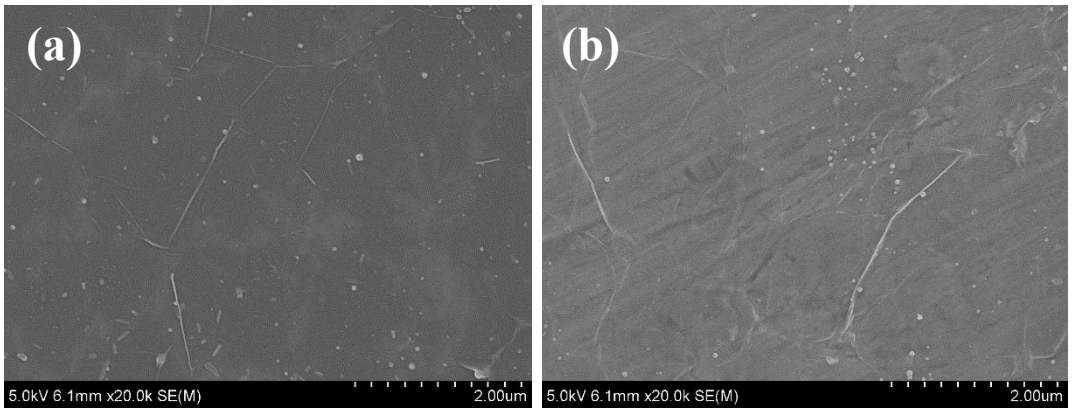

Figure 6-4: (a) High magnification image of graphene layer on silicon wafer surface, (b) High magnification image of graphene on stainless steel surface.

For both silicon wafer and stainless steel substrates, in addition to deposition of graphene layer, non-uniform nano-sized spherical structures were also seen on the graphene surface. These particles could be associated with the process of deposition method for graphene layer employed in this work. The EDX spectra confirmed the

particles as carbon atoms. Moreover, some cracks in the figure displays the defects probably produced during the transfer procedure of graphene.

The graphene layers immobilized on a glass substrate and seeded with osteoblasts were examined by bright-field microscope after two days (Figure 6-5). Graphene layer covered the entire area of soda lime glass slides except at the edges. Locally, CVD graphene layer consisted of many ripples and wrinkles in the micrometer scale [227].

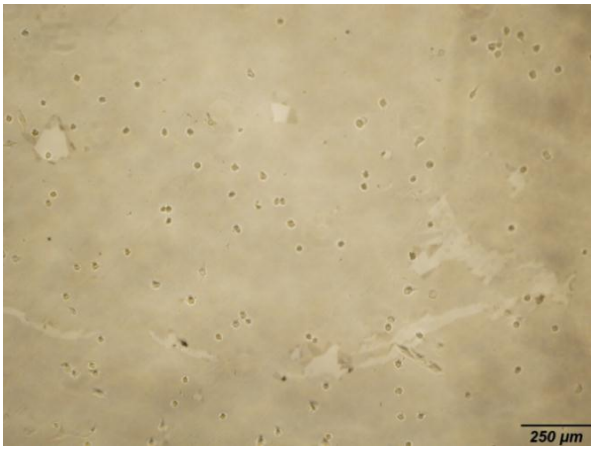

Figure 6-5: Bright-field microscopy image of graphene coated layer on glass substrate with cells at day 2.

6.4.4 Surface-cell interaction study

In this section, cell viability and attachment are discussed by image analysis on all three substrates with and without graphene coated layer. Few layers of graphene on plain cover soda lime glass, silicon wafer and stainless steel sheet were taken for surface-cell interaction study. Cells were cultured in osteogenic culture medium and two time points (day 2 and day 5) were selected to examine the cell viability, attachment and proliferation.

We analyzed parameters quantitatively related to cell morphology including cell morphology (size and shape) and number of attached cells. Generally, based on statistical data, the presence of graphene does not have significant effect on the shape of the cells in comparison with uncoated glass substrate. From Figure 6-6(a), there was no significant difference ($p>0.05$) in the number of attached cells between graphene coated and uncoated glass substrates demonstrating that cell growth was not affected by the presence of graphene on glass substrate at two time points. Furthermore, at day 2, the cell area was slightly bigger on the glass substrate (370±55 μm^2) than on the graphene coated glass (343±33 μm^2) as shown in Figure 6-9(a) and Figure 6-9(b). However as shown in Figure 6-6(b), at higher time points, the cell area in both samples was approximately the same (413.94±21.3 μm^2 and 422.74±65.3 μm^2 for glass and graphene coated glass, respectively).

After two days, we found that the osteoblasts homogeneously covered in both substrates and cells did not demonstrate the well elongated structure (Figure 6-6(c) and Figure 6-6(d)). At day 5, cells were more confluent than day 2. It can also be concluded from the images that more cells were attached on the graphene coated substrate (759.8±117.8) than on pure glass substrate (735.11±177.7) but the difference was not significant ($p>0.05$) (Figure 6-6(e) and Figure 6-6(f)). At day 5, cultured osteoblasts were homogeneously dispersed on the surfaces of graphene coated substrates and plain glass substrates on the surface and showed more distributed morphology in comparison with day 2.

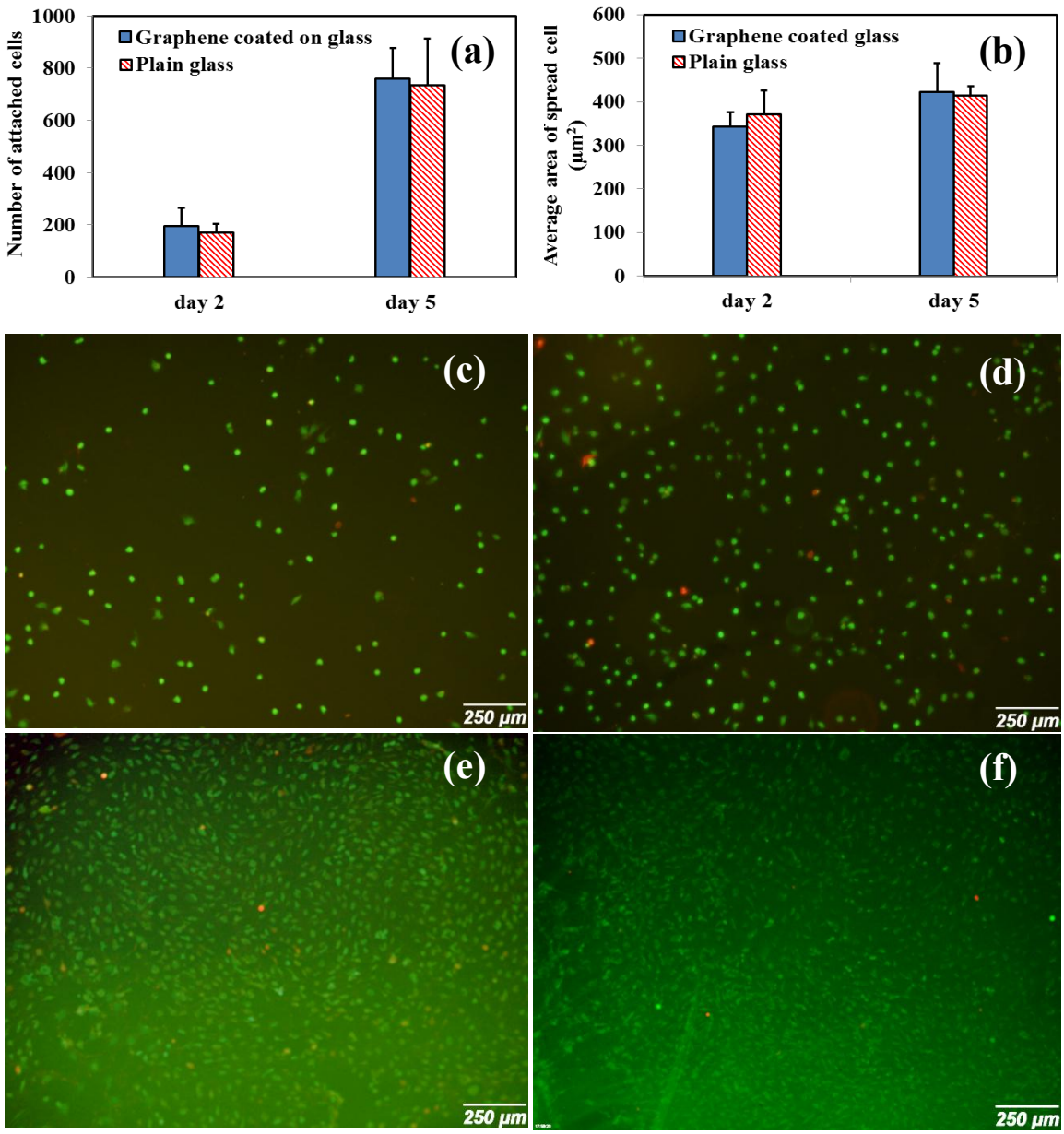

Figure 6-6: Cell attachment and proliferation on glass substrate with and without graphene coated layer at day 2 and day 5, (a) Number of attached cells at day 2 and day 5 for glass with and without graphene layer, (b) Average area of spread cell at day 2 and day 5 for glass with and without graphene layer, (c) Cell spreading on glass substrate at day 2, (d) Cell spreading on graphene coated glass

substrate at day 2, (e) Cell spreading on glass substrate at day 5, (f) Cell spreading on graphene coated glass substrate at day 5.

As shown in Figure 6-6, graphene layer exhibited low cytotoxicity. The survival rate is defined as the average ratio of live cells (Green) to dead cells (Red). Based on this definition, cell survival rate was more than 90% for graphene layer deposited on glass substrate and the pristine glass substrate. Theoretically, the survival rate is close to 100% for healthy cells. Any remarkable difference in the osteoblasts growth and attachment between graphene coated and pristine glass samples was not observed for both time points (day 2 and day 5). This statement was in agreement with the research work reported by Park et al. [211]. However, they demonstrated graphene coated glass samples showed higher percentage of cell attachment after two and three weeks for neural cells. We did not extend the time points to two or three weeks as the purpose of this work was to test the selectivity of different substrates under given time points. This result suggests that graphene does not hamper the normal growth of osteoblast and that the incorporation of this material on glass substrate would not affect the physiological conditions of the microenvironment at the selected time points.

In order to evaluate the biocompatibility of CVD grown graphene films on silicon substrate, two groups of samples were examined: silicon wafer with graphene layers and without graphene layers. 4',6-diamidino-2-phenylindole (DAPI) was used to stain cell nucleus at the boundary edge of silicon wafer and graphene coated silicon at day 2. As it is shown in Figure 6-7(a), higher number of cells was attached to the graphene coated layer in comparison with silicon wafer substrate. In other words, osteoblasts clearly

preferred graphene coated substrate than silicon wafer. This behavior was also confirmed by counting attached cells (Figure 6-7(b)). The number of cells for graphene coated silicon (326.11±60.7) was higher than pure silicon wafer (279.68±70.2) at day 2.

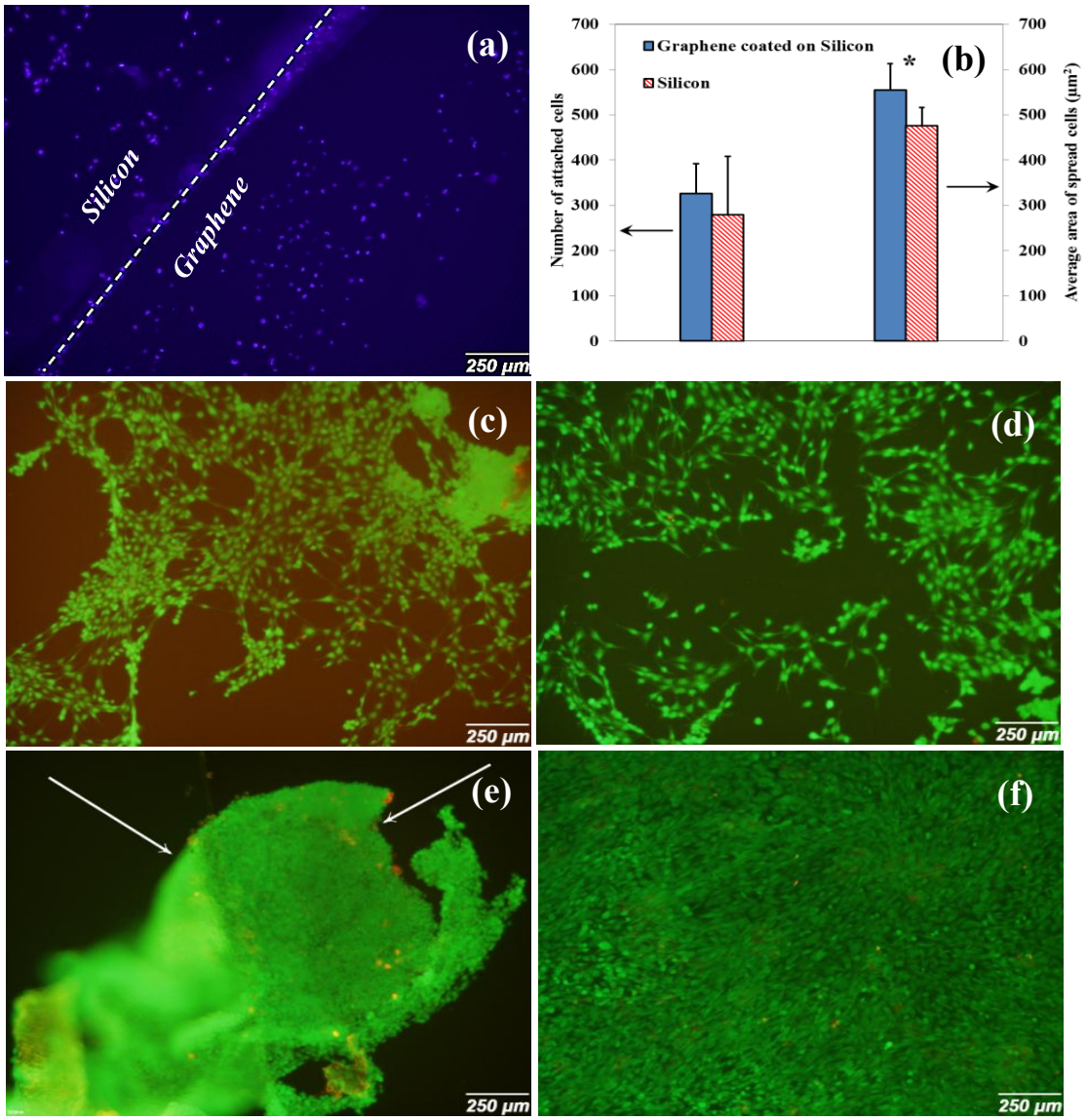

Figure 6-7: Cell attachment and proliferation on silicon wafer substrate with and without graphene coated layer at day 2 and day 5, (a) DAPI stained the cell nucleus at the border of graphene and silicon at day 2, (b) Number of attached cells and average area of spread cells at day 2 for silicon wafer with and without graphene layer, (c)

Cell spreading on silicon substrate at day 2, (d) Cell spreading on graphene coated silicon wafer substrate at day 2, (e) Cell spreading on silicon wafer substrate at day 5, (f) Cell spreading on graphene coated silicon wafer substrate at day 5. Arrows show the detachment of cell layer from the substrate.

Furthermore, the high magnification images (Figure 6-9(c) and Figure 6-9(d)) demonstrated that the average spread area of cells attached to the graphene coated substrate (475.21±69.6 μm^2) was significantly larger than silicon wafer (279.68±70.2 μm^2) at day 2. In addition, cells were uniformly distributed and covered the substrates (Figure 6-7(c) and Figure 6-7(d)). It has been proven that the cell morphology and structure described differentiation and proliferation [209]. It is worth noting that the elongated and well-distributed cell morphology on the surface showed filopodia extension and cellular propagation fronts. Cells attached to the silicon wafer had more circular and undeveloped morphology with smoother edges (Figure 6-9(c)). However, as observed in high magnification images (Figure 6-9(d)), cells attached to graphene coated substrate exhibited more spread nature. In the short time period, the attachment rates, was very similar to the pure silicon wafer with just a slightly higher value. This is in agreement with some previous works [217]. Although at short time points, silicon wafer samples exhibited acceptable cell attachment, there was a significant difference between the spread cell area in silicon with graphene layer and silicon wafer itself. At day 5, cells were confluent on both groups of samples, showing none of the groups had toxic effect (Figure 6-7(e) and Figure 6-7(f)). The cell viability indicated that the graphene layer was

cell-friendly and biocompatible. In addition, the spread area was bigger on graphene coated substrates than on the silicon wafer.

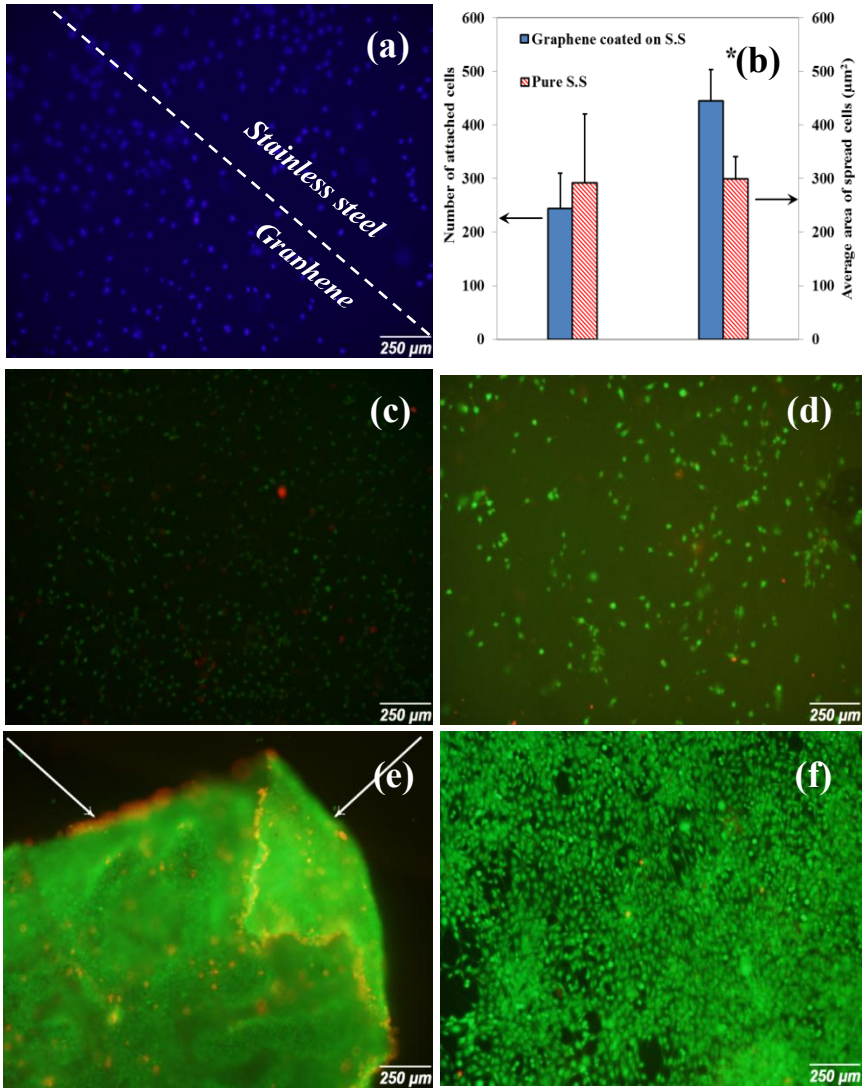

Figure 6-8: Cell attachment and proliferation on stainless steel substrate with and without graphene coated layer at day 2 and day 5, (a) DAPI stained the cell nucleus on stainless steel substrate at day 2, (b) Number of attached cells and average area of spread cells at day 2 for stainless steel with and without graphene layer, (c) Cell spreading on stainless steel substrate at day 2, (d) Cell spreading on graphene coated stainless steel substrate at day 2, (e) Cell spreading on stainless steel

substrate at day 5, (f) Cell spreading on graphene coated stainless steel substrate at day 5. Arrows show the detachment of the cell layer from the substrate.

It is worth noticing that the silicon might not be an ideal substrate based on poor cell attachment. However, it is clearly distinct from Figure 6-7 that a good number of cells proliferated on graphene coated silicon substrate. At day 5, we could not perform the quantitative analysis for silicon samples due to the detachment of cells from the substrate. In contrast, the graphene coated samples showed better cell adhesion and spreading.

Stainless steel has been used as a biocompatible material for a long time [228]. However, there are no papers regarding the effect of graphene coated stainless steel on cell behavior. In this paper, we evaluated the effect of graphene coated stainless steel on cell attachment and proliferation. DAPI cell nucleus straining showed no remarkable difference between the numbers of attached cells on stainless steel with and without graphene layer (Figure 6-8(a)). At day 2, pristine stainless steel substrate showed slightly higher attached cell number (292.2±128.08) in comparison with graphene coated substrate (244.11±65.9). On the other hand, the average spread cell area related to graphene coated stainless steel sample (444.85±58.63 μm^2) was significantly larger than the stainless steel substrate (300.23±40.59 μm^2) as shown in Figure 6-8(b). This result showed that graphene coated on stainless steel could also improve cell spreading in short time points. At day 2, attached cells on stainless steel substrate showed more circular morphology (Figure 6-9(c)) in comparison with the graphene coated stainless steel (Figure 6-9(d)). Osteoblasts uniformly covered over the graphene coated stainless steel

substrate and no evidence of graphene toxicity was observed (Figure 6-8(c) and Figure 6-8(d)).

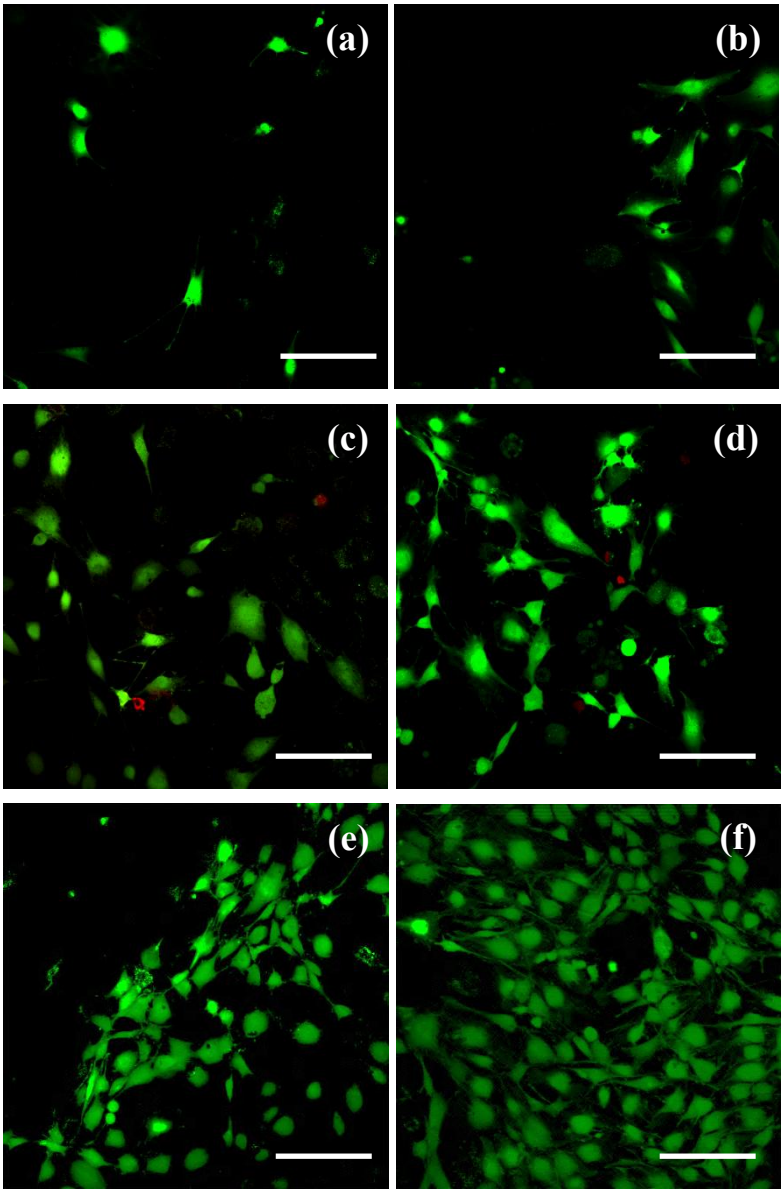

Figure 6-9: High magnification images to show cell morphology on different substrates at day 2, (a) Glass substrate without graphene coated layer, (b) Graphene coated glass substrate (c) Silicon wafer substrate without graphene layer, (d) Graphene

coated silicon wafer substrate, (e) Stainless steel without graphene coated layer, (f) Graphene coated Stainless steel substrate. Scale bar=200 μm.

As demonstrated in Figures 6-8(e) and 6-8(f), at day 5, graphene coated stainless steel samples showed a high number of spread cells while the cells on stainless steel substrate detached from the surface and quantitative analysis could not be performed. The observation confirmed that although stainless steel did not have cytotoxic properties, cell adhesion was poor in comparison with the graphene coated stainless steel samples.

Considering all three samples without graphene coated layer, silicon wafer and stainless steel substrate demonstrated best cell attachment and higher number of attached cells was found in comparison with the glass substrate. This observation can be interpreted as the effect of surface stiffness and roughness. Ponsonnet et al. [229] and Deligianni et al. [67, 230] showed that surface roughness affected the cell behavior. In this study, the cell viability on each substrate was not greatly affected by surface roughness of the substrate. Although stainless steel had higher surface roughness in comparison with silicon, the number of attached cells was almost equal in both samples. The reason probably is the surface roughness of the substrates (R_a (Roughness absolute value)= 0.11. 0.32 and 2.5 nm for glass, silicon and stainless steel respectively based on manufacturer specifications) did not involve a wide value range to induce observable differences in cell attachment [217].

Investigating cell spread area of three substrates revealed a difference between silicon wafer and other two substrates. An important factor which greatly influences the cell attachment and proliferation is substrate stiffness or elastic modulus. Cells can sense

lower lying layers down to several micrometers [231]. It has been demonstrated that substrate matrix elasticity can direct the stem cell lineage proliferation [232]. The specific behavior of osteoblasts on different graphene substrates has not yet been investigated. Because of the presence of few nanometer thickness graphene layers, cells could sense the stiffer underlying layers. The overall results approved that the stiffer substrate was more cell-friendly. However, no evidence was found to show that cells can sense the substrate elastic modulus more than few hundred kilopascals (kPa) [231, 233]. Another effect of graphene layers is that it can enhance vinculin protein for cell attachment [215]. Cell spread area on silicon wafer and stainless steel substrate with graphene coated layers showed significant difference in comparison with silicon wafer and stainless steel. Detaching cells from the silicon and stainless steel substrate without graphene layer is a strong evidence of strong attachment of cells in the presence of graphene layer.

The mechanism of how graphene can improve cell adhesion is still not understood. The differences in cell attachment rates may be attributed to absorption levels of various adhesion proteins such as vinculin and fibronectin on the different substrates [234]. In the presence of graphene molecules, these proteins were more effectively adsorbed on the substrate.

In addition, the ability of graphene to sustain stress could play a more important role in the context of providing just the right amount of local cytoskeleton tension. Graphene may allow for easy out-of-plane deformation leading to the formation of strong anchor points of the cytoskeleton [219].

Furthermore, the cell density is a considerable parameter in observing the attachment properties of substrate. Surface wettability may also affect the cell attachment due to the

fact that the initial phase of attachment involves the chemical linkages between surface and cells [235]. Basically, more detail studies are needed to fully uncover the interaction between cells and graphene layers of different substrates. It would also be interesting to compare the graphene layers produced by other methods, such as chemical reduction, mechanical and chemical exfoliation to understand the effect of graphene and its derivatives on cell attachment and proliferation. It would also be worth researching about cell attachments on different graphene/substrate stacks as the physical and chemical properties would greatly vary with the binding energy between the substrates and the graphene layers.

6.5 Conclusions

In this paper, we confirmed that CVD grown graphene did not have toxic effects on osteoblasts. Furthermore, it was demonstrated that graphene substrate greatly influenced the cell attachment behavior and morphology in the presence of graphene. Silicon wafer and stainless steel substrates with graphene layers showed great cell attachment at different time points. This result can be attributed to the effect of diverse parameters such as surface roughness, wettability, and material chemistry. However, more research is needed to investigate the effect of other material properties such as substrate hardness, high range elastic modulus, wettability and number of graphene layers. Our results indicated that graphene film could be potentially used to fabricate on diverse biomedical materials to improve osteoblast attachment and proliferation. Graphene layer fabricated on bone implant components would also decrease the healing time after surgery.

Chapter 7

The Effect of Mechanical Stimulation on Osteoblasts

7.1 Introduction

Shear stress is commonly considered as a critical factor affecting specific cell lines such as endothelial cell morphology and function [236, 237]. Cells elongate and orient with uniaxial steady flow direction, while unsheared cells have a randomly oriented cobblestone appearance [238]. Gradually increased steady shear stress reduces cell detachment [239]. Axial spreading of cells is increased by shear stress and mechanical stimulation, but transverse spreading is unaffected [240]. Previous studies showed that cells in steady shear constantly rearrange their positions with no net migration, but cells subjected to large spatial gradients of shear proliferate, change shape and actively migrate away from offending locations [241, 242]. Randomness of the oscillatory shear stress in turbulent flow may also be a factor, however, spatial fluctuations have been shown to inhibit elongation and alignment [243, 244].

A number of experimental setups have been used to generate different types of shear force [245, 246]. Parallel plate flow chambers generate uniaxial shear simply and controllably, but care must be taken to account for entrance length and the variation of

shear across the transverse direction in the channel. The cone and plate apparatus gives nearly uniform tangential shear field when operated at moderate to low speeds [247]. An obstruction can be placed in either flow channel to create recirculation and reattachment zone with spatial gradients of shear. Oscillatory or pulsatile flow can be created in either apparatus with special pumps and drive motors. A disadvantage of both is that only one experiment can be performed at a time, which may cause long time requirements for large arrays of experiments. Orbital shakers, on the other hand, can be used to investigate many cases simultaneously.

To the best of the author's knowledge, there is a lack of studies utilizing cyclic shear stress on osteoblast. In this part, the effect of oscillatory shear stress produced by orbital shaker is presented.

7.2 Methodology

7.2.1 Cell culture and preparation

To prepare cell culture medium, alpha minimum essential medium (α-MEM) supplemented with 9% fetal bovine serum (FBS) and 1% penicillin-streptomycin (Pen Strep) were purchased from Gibco. Each vial of OBs was plated on Petri dishes with 100 mm diameters and incubated at 37°C in a humidified 5% CO_2/95% air atmosphere in an osteogenic medium. Cells were monitored and the medium was changed at every 2–3 days. When the dishes reached 80% confluent, the adherent OBs were harvested as follows: cells were washed twice with Hank's balanced salt solution, treated with 2 consecutive applications of trypsin/EDTA for 3–5 min each at room temperature and

washed with the growth medium. The total cell number of 20,000 was added to the well of the 24 well cell culture plate with flat bottom.

7.2.2 Shear stress applications

Different magnitudes of rotational speeds (i.e. 50, 100, 150 and 200 rpm) were applied to cells by using orbital shaker (Innova 2000; New Brunswick scientific, Edison, NJ).

Two main groups with respect to the time gap between cell seeding and applying shear stress were examined. In the first category, shear stress was applied immediately after cell seeding while in the other group the cells were subjected to the mechanical stimulation after 20 min of cell seeding. For each group, triplicate samples were examined. For each of the mentioned group, the experiment was carried out for both without shear stress application (control) and after 6, 24 and 48 hours of shear stress exposure. In other words, the effects of oscillatory mechanical stimulation and time gap before applying the shear stress exposed on bone cell were investigated in three time points.

Orbital shakers can be used to investigate the effect of oscillatory shear stress on the bottom of the orbiting dish. Shear generated by an orbital shaker has been previously described [248]:

$$\tau = a\sqrt{\rho.\mu.(2\pi f)^3}$$

Where τ is the maximum shear stress on the bottom of the dish, a is the radius of orbit, ρ is the fluid density, μ is the fluid viscosity, and f is the frequency of rotation (round/sec). We assume cell culture medium has fluid properties similar to water.

Therefore, viscosity is 8.94×10^{-4} Pa.s and the density is $1000\,kg/m^3$. The radius of orbit was measured to be 19 mm. It has been shown that although some other parameters like dish geometry, effects of gravity and fluid volume have not been incorporated in the equation. A comparison with the model solved using computational fluid dynamics method showed an acceptable accuracy for small dimensional circular dishes. This equation is the solution for the scalar quantity of shear stress in an extension of stoke second problem to orbital motion of an infinite width plate under a layer of fluid with height much larger than the viscous boundary layer thickness.

7.2.3 Viability assay, microscopy and image analysis

Live/dead cell assay was utilized to identify cells their total spread area. By using this assay, cells were characterized by immunofluoresent staining of live cells (Calcein-AM, Invitrogen) as green color and dead cells (Ethidium homodimer, Invitrogen) as red color. Images of cells were captured with an Olympus FSX-100 fluorescence microscope at 4X magnification.

Total cell areas for each well plate were measured by using ImageJ software. For the accurate measurement purpose, each well was divided into three areas (Figure 7-1); the most outer part of the well area defined as a strip with 2 mm thickness (Edge) or 75%-100% of the total dish radius. The middle part was a strip with the thickness of 4 mm (Periphery) from 25%-75% of the total dish radius, and the inner circle with 4 mm radius.

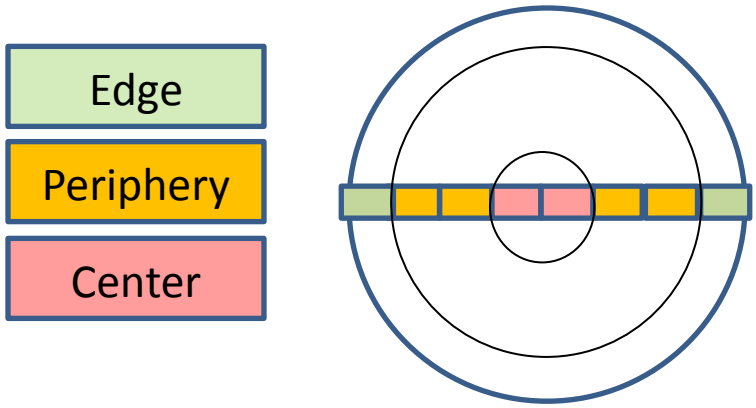

Figure 7-1: Dividing well to different areas for Live/Dead cell assay.

Eight images were captured along the well diameter and the procedure was repeated three times for each well in distinct direction.

7.3 Result and discussion

In this section, the cells exposed to different magnitude of shear stress are discussed. *At 50 rpm.* The calculated value of shear stress corresponding to 50 rpm speed is 2.25 dynes/cm^2. Considering the results of shear stress exposed after a 20 minute time gap, cells aggregated at the center and edge of the well plate. This is attributed to the magnitude and fluctuation of the shear stress. Theoretically, the shear stress near the well plate walls is zero and a higher percentage of area is covered by cells (Figure 7-2(a)). The number of attached cells was small at the periphery region where the shear stress was maximum and the fluctuation is highest (Figure 7-2(b)). In addition, the center region has

highest number of attached cells due to the cell migration from edge and periphery areas (Figure 7-2(c)).

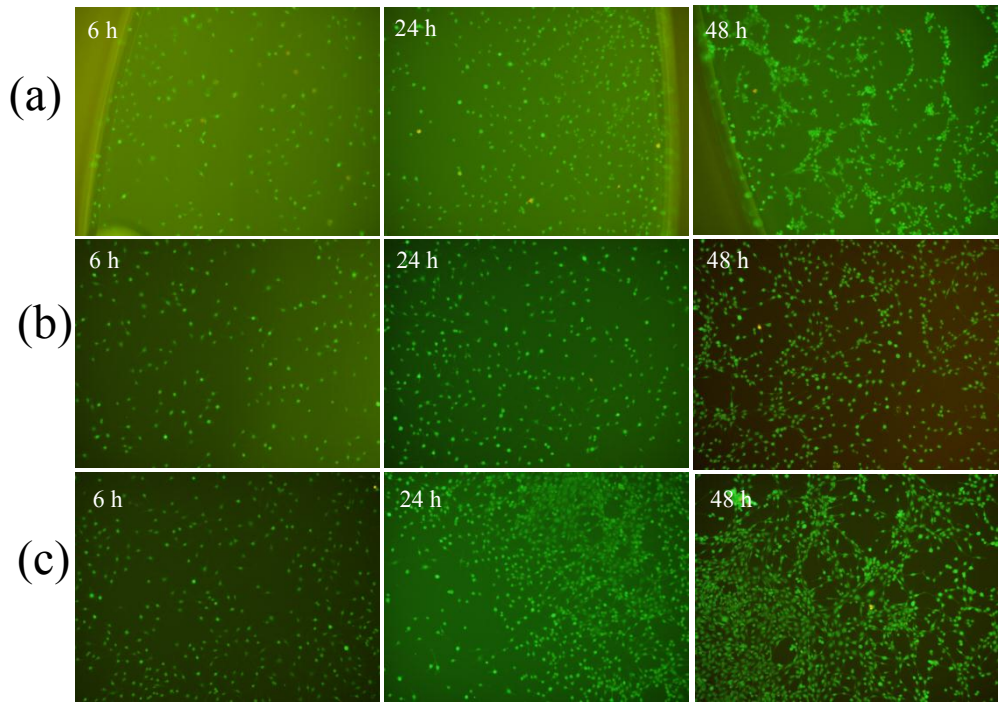

Figure 7-2: Cell attachment and spreading on different well plate regions and time points at 50 rpm speed and with 20 min time gap. (a) At edge, (b) At periphery and (c) Center.

Although this phenomenon was observed for all time points, the effect of oscillatory shear stress was not significant in total cell area which is a scale of the total number of attached and spread cells (Figure 7-3(a) and (c)). On the other hand, a higher fraction of dish area was covered by cells at the center and edge regions showing the immigration of cells due to the shear force (Figure 7-3(b)). Comparatively, a small percentage of total area was covered by cells at the periphery region.

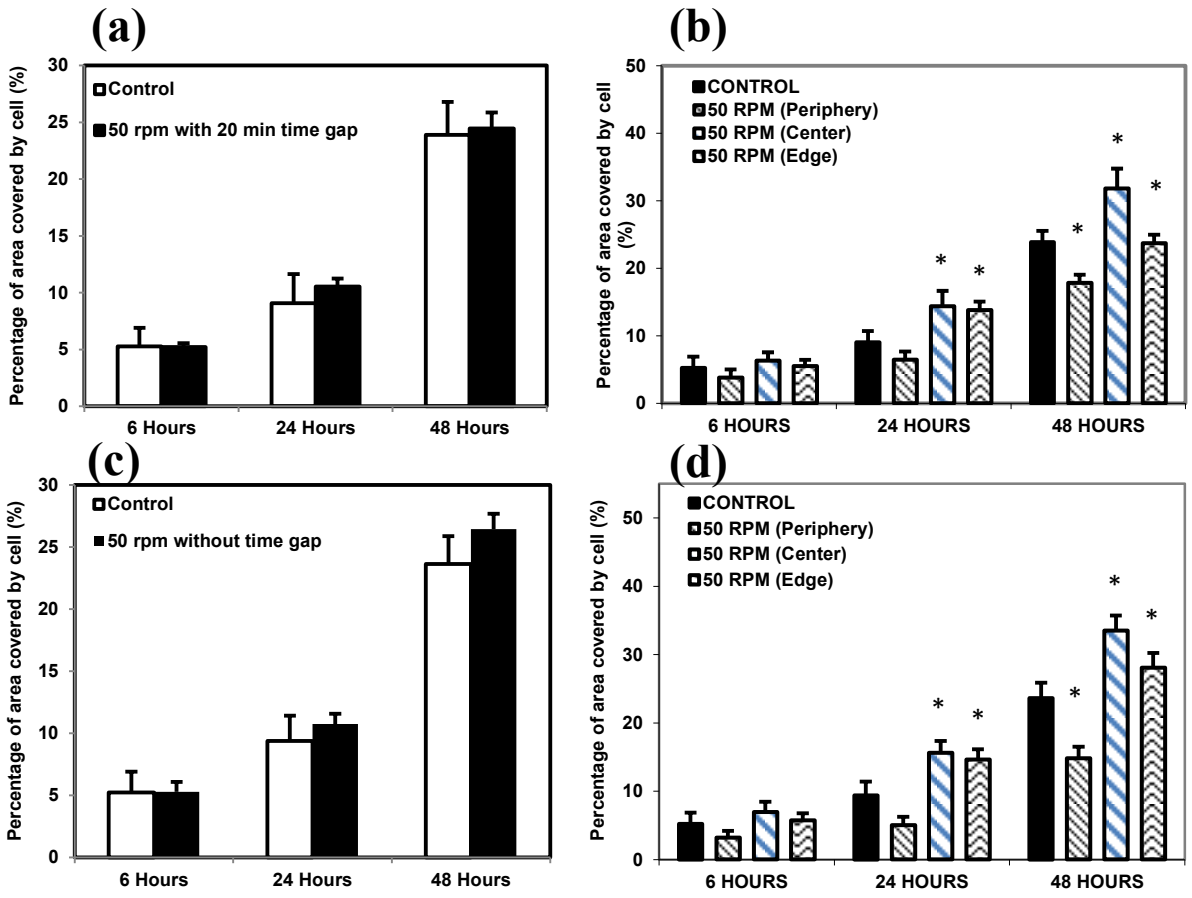

Figure 7-3: The effect of shear stress on (a) Total percentage of area covered by cells, (b) Percentage of area covered by cells in different well plate regions at 50 rpm with 20 min time gap. (c) Total percentage of area covered by cells, (d) Percentage of area covered by cells in different well plate regions at 50 rpm without time gap. * denotes the significant difference from control samples.

The same behavior was observed for all the selected time points. For example, after 6 hours shear stress exposure, the total areas covered by cells were 3.8%, 6.3% and 5.5% of the total captured image for the periphery, center and edge region while the average area of the images from various well regions was 5.3%. No significant difference was

observed for the 6 hours time point. However, at higher time points the differences between the areas covered by cells was more significant. The overall result shows although the magnitude of exposed shear stress was small the majority of cells did not extend extra cellular matrix and vanculin protein to attach to the well substrate. Cells were migrated to the regions with lowest applied shear stress.

Samples without the time gap did not demonstrate a big difference from those with the time gap (Figure 7-3(c) and Figure 7-3(d)). The total number of cells was similar to the control sample in all time points. In addition, visual cell behavior observation showed cell behavior similar to what was seen in the samples with 20 min time gap (Figure 7-2) and therefore, is not shown here. Considering the areas covered by cells in different regions quantitatively, slightly more cells migration to the center of the well plate was observed in comparison with the samples with the 20 min time gap.

At 100 rpm. The theoretical value for shear stress estimated in 100 rpm rotational speed is 6.45 dynes/cm^2. The calculated results are shown in Figure 7-4. In this speed, significant difference was observed between control and other groups of samples after 48 hours. At lower time points, although the percentage of area covered by cells was increased the statistical analysis did not show a significant difference. In addition, after 24 hours of applying shear stress, significantly higher numbers of cells were attached to the center and edge regions of the well plate for both samples with and without the 20 min time gap. Similar to what we observed previously, at 48 hours time point, significant difference was seen between control and periphery region, demonstrating that cells migrated to the center due to the shear force stimulation.

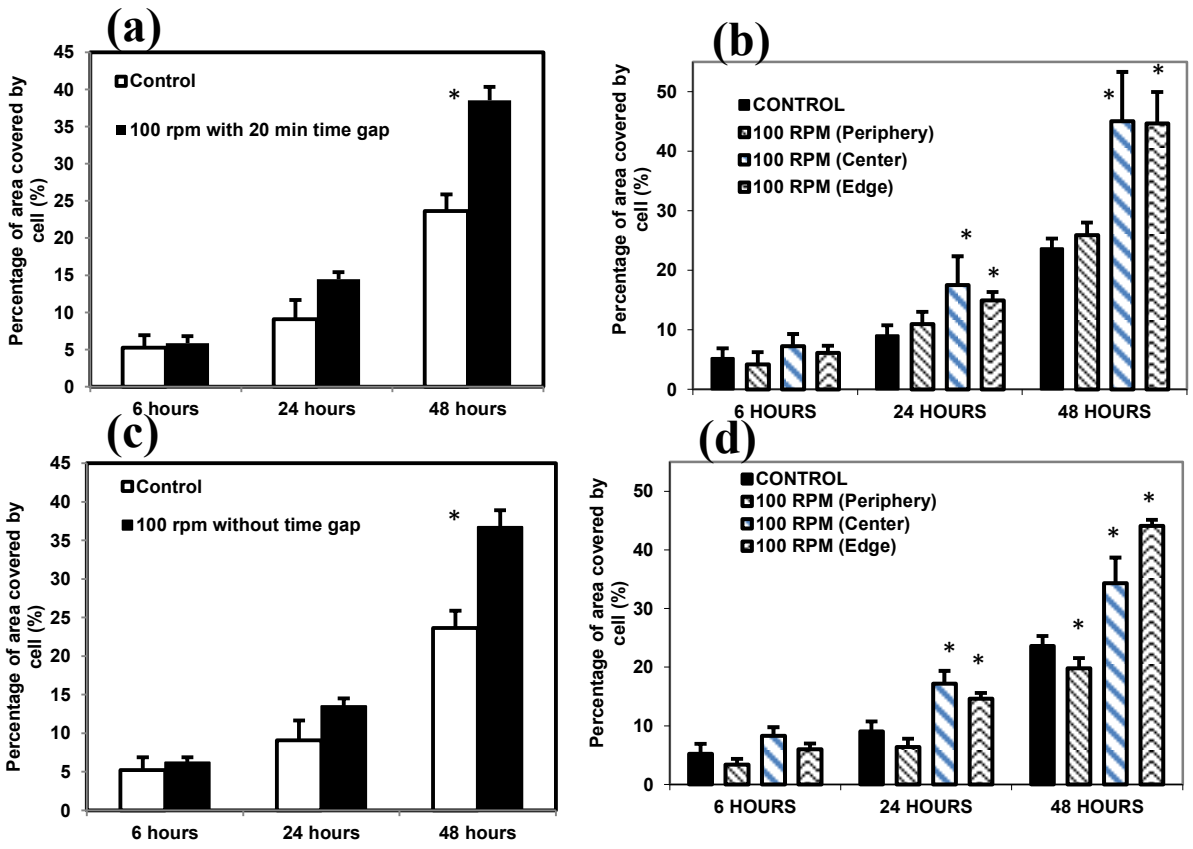

Figure 7-4: The effect of shear stress on (a) Total percentage of area covered by cells, (b) Percentage of area covered by cells in different well plate regions at 100 rpm with 20 min time gap, (c) Total percentage of area covered by cells, (d) Percentage of area covered by cells in different well plate regions at 100 rpm without time gap. * denotes the significant difference from control samples.

At this speed the total percentage of area covered by cells was significantly increased. At the 48 hours time point, for the sample with the 20 min time gap, almost 40% of the total well plate area was covered by attached cells. This value is around 36% for samples without the time gap. This shows that within 20 min, cells started attaching to the surface

and developing vanculine protein for cell attachment. In addition, this time gap helps a higher number of cells to attach.

At 150 rpm. The magnitude of applied shear stress in 150 rpm speed was 11.82 dynes/cm^2. At this rotational speed, the effect of mechanical stimulation was arisen at an earlier time point. As shown in Figure 7-5, after 24 hours a significantly higher percentage of well plate area was covered by cell in comparison with control sample for samples exposed to the shear stress after the 20 min time gap. On the other hand, applying shear stress without the time gap does not provide sufficient time for cells to develop adhesion proteins and therefore, the total number of attached cells is lower in comparison with the samples exposed to shear stress after the 20 min time gap. Interesting phenomena were observed in samples exposed to shear stress without time gap. At this speed cells started aggregating to each other and making bigger spheres with the approximate diameter of few hundred μm. This can be contributed to the higher magnitude of applied shear stress. At this speed cells attached together because they did not settle down on well plate surface due to the high magnitude of shear stress.

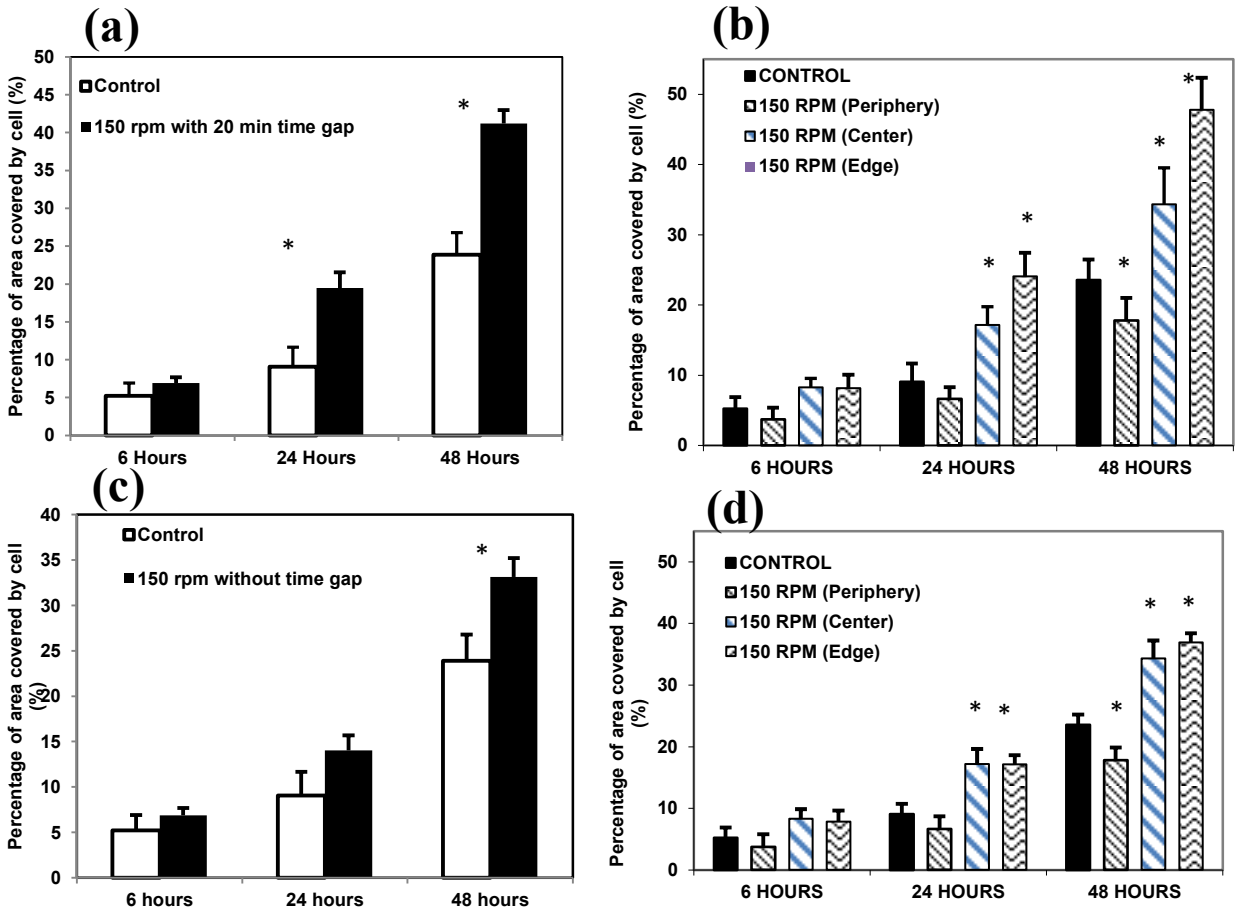

Figure 7-5: The effect of shear stress on (a) Total percentage of area covered by cells, (b) Percentage of area covered by cells in different well plate regions at 150 rpm with 20 min time gap, (c) Total percentage of area covered by cells, (d) Percentage of area covered by cells in different well plate regions at 150 rpm without time gap. * denotes the significant difference from control samples.

At 200 rpm. The magnitude of shear stress in 200 rpm rotational speed was calculated about 18.2 dynes/cm^2. Figure 7-6 shows the results for 200 rpm rotational speed with 20 min waiting. We could not detect any cells attached to the well plate for sample exposed to 200 rpm without the time gap. This is because of the high shear stress induced to the osteoblasts. In addition, in samples with the 20 min time gap, a lower percent of area covered by cell in comparison with 150 rpm, showing 20 min time gap is not enough for cells to attach well and elongate in 200 rpm.

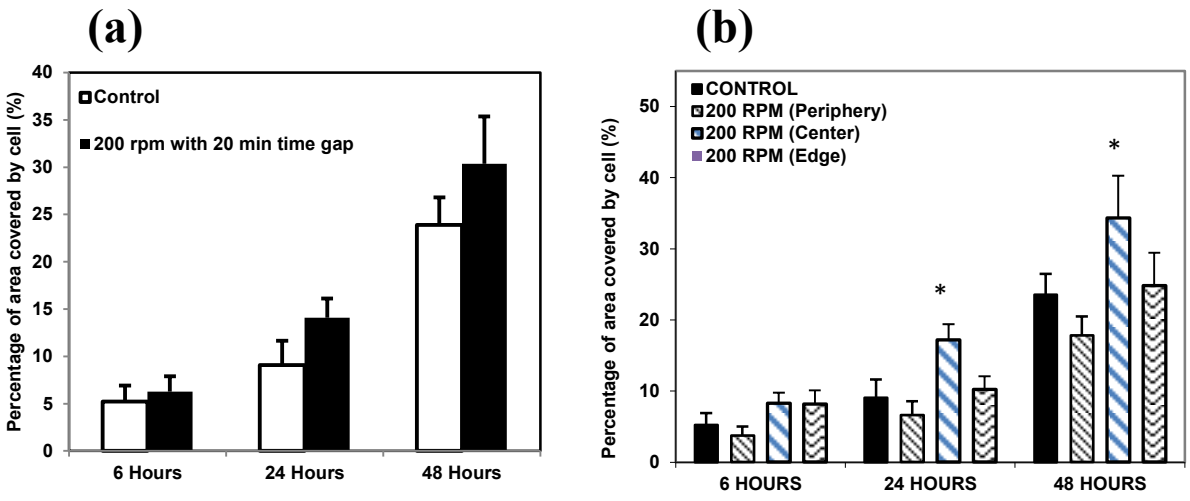

Figure 7-6: The effect of shear stress on (a) Total percentage of area covered by cells, (b) Percentage of area covered by cells in different well plate regions at 200 rpm with 20 min time gap.

7.4 Conclusions

Our obtained results show that similar to endothelial cell lines, osteoblasts are also sensitive to the mechanical stimulation. Small changes in the magnitude of shear stress can greatly affect the cell's response. We have shown that a time gap between cell

seeding and applying mechanical stimulation affects the cells reaction. Waiting for 20 min before applying shear stress increased the number of attached cell in all different rotational speed. In addition, cells do not significantly respond to the low shear stress as we could see at the speed of 50 rpm. This indicates that cells sense threshold for shear stress. On the other hand, applying a high magnitude of shear stress as we did in 200 rpm is not beneficial for cell attachment and elongation. In summary, mechanical stimulation improves cell attachment and proliferation for osteoblasts but rotational speed and time gap between cell seeding and mechanical stimulation should be optimized.

Chapter 8

Conclusions and Future Directions

8.1 Conclusions

The overall primary goal of this project was to investigate the new promising biomaterials with exceptional mechanical and biological properties for tissue engineering. In addition, we combined mechanical engineering science with biology and cell sciences to measure elastic modulus of living cells and investigate the effect of shear stress on osteoblast proliferation and attachment. Statistical analysis was also done mainly using one-way ANOVA

In chapter 2, we applied cross-linking method to improve micro and nano mechanical properties of chitosan film. Nano and micro mechanical testing revealed that having chitosan cross-linked can increase the elastic modulus up to almost 200%. Our results showed the mechanical properties of cross-linked chitosan are more similar to bone.

The effect of ZnO on chitosan films was investigated in chapter 3. Our results showed that having a small percentage of ZnO on chitosan films can improve mechanical properties of the films. However, adding more than 5% of ZnO decreased the cell

viability. In summary, the percentage of ZnO into chitosan should be optimized based on desired mechanical properties and cell viability.

In chapter 4, the properties of chitosan film incorporated with MWCNT were explored. Small amount of MWCNT has a great influence on mechanical and material properties of chitosan biopolymer. Particularly, adding a small percentage of MWCNT can drastically increase the elastic modulus of chitosan films.

All of the new fabricated biomaterials had some advantages and disadvantages. Table 8-1 summarized the properties of these biomaterials.

Method utilized for improving mechanical properties of chitosan	**Advantages**	**Disadvantages**
Cross-linking using TPP	Easy to fabricate, Drastic improvement in mechanical elastic modulus in micro and nano scale.	Dependency of various parameters such as temperature and time, Brittleness of samples.
Adding ZnO NP's	Inducing higher antibacterial activity into chitosan, improvement in mechanical properties.	Toxicity at higher percentages of ZnO, Brittleness of samples.
Adding MWCNT	Increasing the elastic modulus and surface hardness, increasing the viscosity of chitosan solution, increasing light absorbtion properties, No significant effect on pH. Non toxic effect in higher percentage of MWCNT.	MWCNT is not degradable, Brittleness of samples.

Table 8-1: Advantages and disadvantages of the bio- nanocomposites discussed in this dissertation.

In chapter 5, the conventional method of using AFM was modified to measure cells and biological samples mechanical properties. The presented method does not require any adhesion proteins or specific surface treatment before the experiment. Elastic modulus of two cell lines (amniotic fluid stem cells and osteoblasts) was estimated using Hertz model at different cell regions.

In the next chapter, the effect of graphene on different substrates was examined. Substrates including glass, stainless steel and silicon wafer showed different behavior with and without graphene. Final results showed that having a few nanometers of graphene layer on the substrate could improve the cell attachment and proliferation.

Finally, in chapter 7, the influence of mechanically produced shear stress on osteoblast adhesion and proliferation was investigated. Based on the presented results, a certain magnitude of oscillatory shear stress is beneficial for cell adhesion and proliferation. Another important factor is the time gap between cell seeding and applying mechanical stimulation. In order to get the best rate of cell adhesion, optimization should be performed.

8.2 Future directions

The concept of fabricating bio- nanocomposites with improved mechanical and material properties of tissue engineering has been proposed in this dissertation. In addition, the effect of oscillatory shear stress on osteoblast and mechanical properties of cells was investigated.

New bio- nano composites can be explored in future works. In this dissertation we mainly used nano particles and tubes as reinforcement of chitosan matrix. This can be expanded to fibers as reinforcement and other biopolymer or even cements as a matrix. In addition, *in vivo* study should be performed to finalize the usage of proposed biomaterials in the human body.

The method presented in chapter 5 for measuring cell mechanical properties can be repeated for other well-known cells to compare with other measuring procedures and validate the proposed method.

Mechanical stimulation can be applied to biomaterials seeded with cells in bioreactors to increase the cell proliferation and attachment. In addition, other cell lines can be examined to investigate the effects of mechanical stimulation on cell behavior.

References

1. O'Brien, F.J., *Biomaterials & scaffolds for tissue engineering.* Materials Today, 2011. **14**(3): p. 88-95.
2. Hench, L.L., *Biomaterials: a forecast for the future.* Biomaterials, 1998. **19**(16): p. 1419-1423.
3. Salgado, A.J., O.P. Coutinho, and R.L. Reis, *Bone tissue engineering: state of the art and future trends.* Macromolecular bioscience, 2004. **4**(8): p. 743-765.
4. Caruthers, S.D., S.A. Wickline, and G.M. Lanza, *Nanotechnological applications in medicine.* Current opinion in Biotechnology, 2007. **18**(1): p. 26-30.
5. Engel, E., et al., *Nanotechnology in regenerative medicine: the materials side.* Trends in biotechnology, 2008. **26**(1): p. 39-47.
6. Ravi Kumar, M.N., *A review of chitin and chitosan applications.* Reactive and functional polymers, 2000. **46**(1): p. 1-27.
7. Jayakumar, R., et al., *Biomedical applications of chitin and chitosan based nanomaterials—A short review.* Carbohydrate Polymers, 2010. **82**(2): p. 227-232.
8. Jayasuriya, A.C. and A. Bhat, *Optimization of scaled-up chitosan microparticles for bone regeneration.* Biomedical Materials, 2009. **4**(5): p. 055006.

9. Anal, A.K. and W.F. Stevens, *Chitosan–alginate multilayer beads for controlled release of ampicillin.* International journal of pharmaceutics, 2005. **290**(1): p. 45-54.

10. Jayasuriya, A.C. and A. Bhat, *Mesenchymal stem cell function on hybrid organic/inorganic microparticles in vitro.* Journal of Tissue Engineering and Regenerative Medicine, 2010. **4**(5): p. 340-348.

11. Wang, S., et al., *Biopolymer chitosan/montmorillonite nanocomposites: preparation and characterization.* Polymer Degradation and Stability, 2005. **90**(1): p. 123-131.

12. Caner, C., P. Vergano, and J. Wiles, *Chitosan film mechanical and permeation properties as affected by acid, plasticizer, and storage.* Journal of Food Science, 1998. **63**(6): p. 1049-1053.

13. Richert, L., et al., *Elasticity of native and cross-linked polyelectrolyte multilayer films.* Biomacromolecules, 2004. **5**(5): p. 1908-1916.

14. Lekka, M., *Atomic force microscopy: A tip for diagnosing cancer.* Nature Nanotechnology, 2012. **7**(11): p. 691-692.

15. Cross, S.E., et al., *Nanomechanical analysis of cells from cancer patients.* Nature Nanotechnology, 2007. **2**(12): p. 780-783.

16. Bao, G. and S. Suresh, *Cell and molecular mechanics of biological materials.* Nature Materials, 2003. **2**(11): p. 715-25.

17. Allison, D.P., et al., *Atomic force microscopy of biological samples.* Wiley Interdiscip Rev Nanomed Nanobiotechnol, 2010. **2**(6): p. 618-634.

18. Jayasuriya, A.C. and N.A. Ebraheim, *Evaluation of bone matrix and demineralized bone matrix incorporated PLGA matrices for bone repair.* Journal of Materials Science: Materials in Medicine, 2009. **20**(8): p. 1637-1644.

19. Casuso, I., F. Rico, and S. Scheuring, *Biological AFM: where we come from – where we are – where we may go.* Journal of Molecular Recognition, 2011. **24**(3): p. 406-413.

20. Aryaei, A. and A.C. Jayasuriya, *Mechanical properties of human amniotic fluid stem cells using nanoindentation.* Journal of Biomechanics, 2013. **46**(9): p. 1524-1530.

21. Wan, Q., et al., *Fabrication and ethanol sensing characteristics of ZnO nanowire gas sensors.* Applied Physics Letters, 2004. **84**(18): p. 3654-3656.

22. Hanley, C., et al., *Preferential killing of cancer cells and activated human T cells using ZnO nanoparticles.* Nanotechnology, 2008. **19**(29): p. 295103.

23. Colon, G., B.C. Ward, and T.J. Webster, *Increased osteoblast and decreased Staphylococcus epidermidis functions on nanophase ZnO and TiO2.* Journal of Biomedical Materials Research, Part A, 2006. **78A**(3): p. 595-604.

24. Padmavathy, N. and R. Vijayaraghavan, *Enhanced bioactivity of ZnO nanoparticles—an antimicrobial study.* Science and Technology of Advanced Materials, 2008. **9**(3): p. 035004.

25. Aruoja, V., et al., *Toxicity of nanoparticles of CuO, ZnO and TiO2 to microalgae Pseudokirchneriella subcapitata.* Science of The Total Environment, 2009. **407**(4): p. 1461-1468.

26. Heng, B., et al., *Cytotoxicity of zinc oxide (ZnO) nanoparticles is influenced by cell density and culture format.* Archives of Toxicology, 2011. **85**(6): p. 695-704.

27. Yan, D., et al., *Cellular Compatibility of Biomineralized ZnO Nanoparticles Based on Prokaryotic and Eukaryotic Systems.* Langmuir, 2011. **27**(21): p. 13206-13211.

28. Han, Y., et al., *Effect of nano-oxide concentration on the mechanical properties of a maxillofacial silicone elastomer.* The Journal of Prosthetic Dentistry, 2008. **100**(6): p. 465-473.

29. Liu, H. and T.J. Webster, *Mechanical properties of dispersed ceramic nanoparticles in polymer composites for orthopedic applications.* International Journal of Nanomedicine, 2010. **5**: p. 299.

30. Alexandre, M. and P. Dubois, *Polymer-layered silicate nanocomposites: preparation, properties and uses of a new class of materials.* Materials Science and Engineering: R: Reports, 2000. **28**(1): p. 1-63.

31. Sinha Ray, S. and M. Okamoto, *Polymer/layered silicate nanocomposites: a review from preparation to processing.* Progress in polymer science, 2003. **28**(11): p. 1539-1641.

32. Nettles, D.L., S.H. Elder, and J.A. Gilbert, *Potential use of chitosan as a cell scaffold material for cartilage tissue engineering.* Tissue engineering, 2002. **8**(6): p. 1009-1016.

33. Jayasuriya, A.C. and S. Kibbe, *Rapid biomineralization of chitosan microparticles to apply in bone regeneration.* Journal of Materials Science: Materials in Medicine, 2010. **21**(2): p. 393-398.

34. Soleimanpour, A.M., A.H. Jayatissa, and G. Sumanasekera, *Surface and gas sensing properties of nanocrystalline nickel oxide thin films.* Applied Surface Science, 2013. **276**: p. 291-297.

35. Desai, K. and H. Park, *Effect of manufacturing parameters on the characteristics of vitamin C encapsulated tripolyphosphate-chitosan microspheres prepared by spray-drying.* Journal of microencapsulation, 2006. **23**(1): p. 91-103.

36. Stulzer, H.K., et al., *Evaluation of cross-linked chitosan microparticles containing acyclovir obtained by spray-drying.* Materials Science and Engineering: C, 2009. **29**(2): p. 387-392.

37. Co, C.C., Y.-C. Wang, and C.-C. Ho, *Biocompatible micropatterning of two different cell types.* Journal of the American Chemical Society, 2005. **127**(6): p. 1598-1599.

38. Oliver, W.C. and G.M. Pharr, *An improved technique for determining hardness and elastic modulus using load and displacement sensing indentation experiments.* Journal of Materials Research, 1992. **7**(6): p. 1564-1583.

39. Nowicki, M., et al., *Nanoscale mechanical properties of polymers irradiated by UV.* Polymer, 2003. **44**(21): p. 6599-6606.

40. Donnelly, E., et al., *Effects of surface roughness and maximum load on the mechanical properties of cancellous bone measured by nanoindentation.* Journal of Biomedical Materials Research Part A, 2006. **77**(2): p. 426-435.

41. Misran, M., *Surface investigation of chitosan film with fatty acid monolayers.* Maejo International Journal of Science and Technology, 2009. **3**.

42. Jayasuriya, A.C., et al., *Acceleration of biomimetic mineralization to apply in bone regeneration.* Biomedical Materials, 2008. **3**(1): p. 015003.

43. Reynaud, C., et al., *Quantitative determination of Young's modulus on a biphase polymer system using atomic force microscopy.* Surface and interface analysis, 2000. **30**(1): p. 185-189.

44. Arpornmaeklong, P., et al., *Growth and differentiation of mouse osteoblasts on chitosan–collagen sponges.* International journal of oral and maxillofacial surgery, 2007. **36**(4): p. 328-337.

45. Jayasuriya, A.C. and A. Bhat, *Fabrication and characterization of novel hybrid organic/inorganic microparticles to apply in bone regeneration.* Journal of Biomedical Materials Research Part A, 2010. **93**(4): p. 1280-1288.

46. Rho, J.-Y., T.Y. Tsui, and G.M. Pharr, *Elastic properties of human cortical and trabecular lamellar bone measured by nanoindentation.* Biomaterials, 1997. **18**(20): p. 1325-1330.

47. Qian, L., et al., *Comparison of nano-indentation hardness to microhardness.* Surface and Coatings Technology, 2005. **195**(2): p. 264-271.

48. Swadener, J., E. George, and G. Pharr, *The correlation of the indentation size effect measured with indenters of various shapes.* Journal of the Mechanics and Physics of Solids, 2002. **50**(4): p. 681-694.

49. Domke, J. and M. Radmacher, *Measuring the elastic properties of thin polymer films with the atomic force microscope.* Langmuir, 1998. **14**(12): p. 3320-3325.

50. Qian, L., et al., *Comparison of nano-indentation hardness to microhardness.* Surface and Coatings Technology, 2005. **195**(2–3): p. 264-271.

51. Kato, Y., H. Onishi, and Y. Machida, *Application of Chitin and Chitosan Derivatives in the Pharmaceutical Field.* Current Pharmaceutical Biotechnology, 2003. **4**(5): p. 303-309.

52. Seol, Y.-J., et al., *Chitosan sponges as tissue engineering scaffolds for bone formation.* Biotechnology Letters, 2004. **26**(13): p. 1037-1041.

53. Di Martino, A., M. Sittinger, and M.V. Risbud, *Chitosan: A versatile biopolymer for orthopaedic tissue-engineering.* Biomaterials, 2005. **26**(30): p. 5983-5990.

54. Li, Z., et al., *Chitosan–alginate hybrid scaffolds for bone tissue engineering.* Biomaterials, 2005. **26**(18): p. 3919-3928.

55. Bhat, A., et al., *Evaluation of cross-linked chitosan microparticles for bone regeneration.* Journal of Tissue Engineering and Regenerative Medicine, 2010. **4**(7): p. 532-542.

56. Kim, I.Y., et al., *Chitosan and its derivatives for tissue engineering applications.* Biotechnology Advances, 2008. **26**(1): p. 1-21.

57. Zainol, I., H.M. Akil, and A. Mastor, *Effect of γ-irradiation on the physical and mechanical properties of chitosan powder.* Materials Science and Engineering C, 2009. **29**(1): p. 292-297.

58. Kumar, P., et al., *Preparation and characterization of novel β-chitin/nanosilver composite scaffolds for wound dressing applications.* Carbohydrate Polymers, 2010. **80**(3): p. 761-767.

59. Aryaei, A., A.H. Jayatissa, and A.C. Jayasuriya, *Nano and micro mechanical properties of uncross-linked and cross-linked chitosan films.* Journal of the Mechanical Behavior of Biomedical Materials, 2012. **5**(1): p. 82-89.

60. Djurišić, A.B., et al., *ZnO nanostructures: growth, properties and applications.* Journal of Materials Chemistry, 2012. **22**(14): p. 6526-6535.

61. Du, W.-L., et al., *Antibacterial activity of chitosan tripolyphosphate nanoparticles loaded with various metal ions.* Carbohydrate Polymers, 2009. **75**(3): p. 385-389.

62. Wang, S.F., et al., *Preparation and mechanical properties of chitosan/carbon nanotubes composites.* Biomacromolecules, 2005. **6**(6): p. 3067-3072.

63. Song, J., et al., *Synthesis of Novel Flower-Like Zn (OH) F via a Microwave-Assisted Ionic Liquid Route and Transformation into Nanoporous ZnO by Heat Treatment.* Nanoscale Research Letters, 2009. **4**(12): p. 1512-1516.

64. Vasconcelos, H.L., et al., *Chitosan crosslinked with a metal complexing agent: Synthesis, characterization and copper (II) ions adsorption.* Reactive and Functional Polymers, 2008. **68**(2): p. 572-579.

65. Orrego, C., et al., *Novel chitosan membranes as support for lipases immobilization: Characterization aspects.* Carbohydrate Polymers, 2010. **79**(1): p. 9-16.

66. Choopun, S., et al., *Zinc oxide nanobelts by RF sputtering for ethanol sensor.* Physica E: Low-dimensional Systems and Nanostructures, 2007. **39**(1): p. 53-56.

67. Deligianni, D.D., et al., *Effect of surface roughness of hydroxyapatite on human bone marrow cell adhesion, proliferation, differentiation and detachment strength.* Biomaterials, 2000. **22**(1): p. 87-96.

68. Oliver, W.C. and G.M. Pharr, *An improved technique for determining hardness and elastic modulus using load and displacement sensing indentation experiments.* Journal of Materials Research, 1992. **7**(6): p. 1564-1583

69. Donnelly, E., et al., *Effects of surface roughness and maximum load on the mechanical properties of cancellous bone measured by nanoindentation.* Journal of Biomedical Materials Research, Part A, 2006. **77**(2): p. 426-435.

70. Hu, G., Y. Ma, and B. Wang, *Mechanical properties and morphology of nylon 11/tetrapod-shaped zinc oxide whisker composite.* Materials Science and Engineering A, 2009. **504**(1–2): p. 8-12.

71. Wacharawichanant, S., et al., *Effect of particle sizes of zinc oxide on mechanical, thermal and morphological properties of polyoxymethylene/zinc oxide nanocomposites.* Polymer Testing, 2008. **27**(8): p. 971-976.

72. Chandler, H., *Hardness Testing*. Second ed. 1999: ASM International.

73. Li, Z., et al., *Cellular Level Biocompatibility and Biosafety of ZnO Nanowires.* The Journal of Physical Chemistry C, 2008. **112**(51): p. 20114-20117.

74. Yang, X., et al., *Real-Time Investigation of Acute Toxicity of ZnO Nanoparticles on Human Lung Epithelia with Hopping Probe Ion Conductance Microscopy.* Chemical Research in Toxicology, 2012. **25**(2): p. 297-304.

75. Kubota, Y., et al., *Photokilling of T-24 human bladder cancer cells with titanium dioxide.* Br J Cancer, 1994. **70**(6): p. 1107-1111.

76. Deng, X., et al., *Nanosized zinc oxide particles induce neural stem cell apoptosis.* Nanotechnology, 2009. **20**(11): p. 115101.

77. Yang, H., et al., *Comparative study of cytotoxicity, oxidative stress and genotoxicity induced by four typical nanomaterials: the role of particle size, shape and composition.* Journal of Applied Toxicology, 2009. **29**(1): p. 69-78.

78. Li, S.-C. and Y.-N. Li, *Mechanical and antibacterial properties of modified nano-ZnO/high-density polyethylene composite films with a low doped content of nano-ZnO.* Journal of Applied Polymer Science, 2010. **116**(5): p. 2965-2969.

79. Jayasuriya, A.C., A. Aryaei, and A.H. Jayatissa, *ZnO nanoparticles induced effects on nanomechanical behavior and cell viability of chitosan films.* Materials Science and Engineering: C, 2013. **33**(7): p. 3688-3696.

80. Mohanty, A., M. Misra, and G. Hinrichsen, *Biofibres, biodegradable polymers and biocomposites: An overview.* Macromolecular Materials and Engineering, 2000. **276**(1): p. 1-24.

81. MacDonald, R.A., et al., *Collagen–carbon nanotube composite materials as scaffolds in tissue engineering.* Journal of Biomedical Materials Research Part A, 2005. **74**(3): p. 489-496.

82. Iijima, S., *Helical microtubules of graphitic carbon.* letters to nature, 1991. **354**(6348): p. 56-58.

83. Shokrieh, M. and R. Rafiee, *A review of the mechanical properties of isolated carbon nanotubes and carbon nanotube composites.* Mechanics of Composite Materials, 2010. **46**(2): p. 155-172.

84. Balandin, A.A., *Thermal properties of graphene and nanostructured carbon materials.* Nature materials, 2011. **10**(8): p. 569-581.

85. MacDonald, R.A., et al., *Carbon nanotubes increase the electrical conductivity of fibroblast-seeded collagen hydrogels.* Acta biomaterialia, 2008. **4**(6): p. 1583-1592.

86. Agarwal, S., et al., *Interfacing live cells with nanocarbon substrates.* Langmuir, 2010. **26**(4): p. 2244-2247.

87. Misra, S.K., et al., *Characterization of carbon nanotube (MWCNT) containing P (3HB)/bioactive glass composites for tissue engineering applications.* Acta biomaterialia, 2010. **6**(3): p. 735-742.

88. Tercero, J.E., et al., *Effect of carbon nanotube and aluminum oxide addition on plasma-sprayed hydroxyapatite coating's mechanical properties and biocompatibility.* Materials Science and Engineering: C, 2009. **29**(7): p. 2195-2202.

89. Lobo, A., et al., *Cell viability and adhesion on as grown multi-wall carbon nanotube films.* Materials Science and Engineering: C, 2008. **28**(2): p. 264-269.

90. Harrison, B.S. and A. Atala, *Carbon nanotube applications for tissue engineering.* Biomaterials, 2007. **28**(2): p. 344-353.

91. Shin, S.R., et al., *Carbon nanotube reinforced hybrid microgels as scaffold materials for cell encapsulation.* ACS nano, 2011. **6**(1): p. 362-372.

92. Abarrategi, A., et al., *Multiwall carbon nanotube scaffolds for tissue engineering purposes.* Biomaterials, 2008. **29**(1): p. 94-102.

93. Price, R.L., et al., *Selective bone cell adhesion on formulations containing carbon nanofibers.* Biomaterials, 2003. **24**(11): p. 1877-1887.

94. Koh, L.B., I. Rodriguez, and S.S. Venkatraman, *A novel nanostructured poly (lactic-co-glycolic-acid)–multi-walled carbon nanotube composite for blood-contacting applications: Thrombogenicity studies.* Acta biomaterialia, 2009. **5**(9): p. 3411-3422.

95. Aryaei, A., A.H. Jayatissa, and A.C. Jayasuriya, *The effect of graphene substrate on osteoblast cell adhesion and proliferation.* Journal of Biomedical Materials Research Part A, 2013.

96. Zhang, M., A. Smith, and W. Gorski, *Carbon nanotube-chitosan system for electrochemical sensing based on dehydrogenase enzymes.* Analytical chemistry, 2004. **76**(17): p. 5045-5050.

97. Nardecchia, S., et al., *Modulating the cytocompatibility of tridimensional carbon nanotube-based scadffolds.* J. Mater. Chem. B, 2013: p. 3064-3072.

98. Chenite, A., et al., *Novel injectable neutral solutions of chitosan form biodegradable gels in situ.* Biomaterials, 2000. **21**(21): p. 2155-2161.

99. Park, D.J., et al., *Injectable bone using chitosan-alginate gel/mesenchymal stem cells/BMP-2 composites.* Journal of Cranio-Maxillofacial Surgery, 2005. **33**(1): p. 50-54.

100. Zhou, G., et al., *A novel pulsed drug-delivery system: polyelectrolyte layer-by-layer coating of chitosan–alginate microgels.* International journal of nanomedicine, 2013. **8**: p. 877-887.

101. Lau, C., M.J. Cooney, and P. Atanassov, *Conductive Macroporous Composite Chitosan− Carbon Nanotube Scaffolds.* Langmuir, 2008. **24**(13): p. 7004-7010.

102. Thompson, B.C., et al., *Carbon nanotube biogels.* Carbon, 2009. **47**(5): p. 1282-1291.

103. Liu, Y.-L., W.-H. Chen, and Y.-H. Chang, *Preparation and properties of chitosan/carbon nanotube nanocomposites using poly (styrene sulfonic acid)-modified CNTs.* Carbohydrate Polymers, 2009. **76**(2): p. 232-238.

104. Carson, L., et al., *Synthesis and characterization of chitosan–carbon nanotube composites.* Materials Letters, 2009. **63**(6–7): p. 617-620.

105. Fraczek, A., et al., *Comparative in vivo biocompatibility study of single-and multi-wall carbon nanotubes.* Acta biomaterialia, 2008. **4**(6): p. 1593-1602.

106. Matsuoka, M., et al., *Strong adhesion of Saos-2 cells to multi-walled carbon nanotubes.* Materials Science and Engineering B, 2010. **173**(1): p. 182-186.

107. Lynam, C., W. Grosse, and G.G. Wallace, *Carbon-nanotube biofiber microelectrodes.* Journal of The Electrochemical Society, 2009. **156**(7): p. 117-121.

108. Dreifke, M.B., N.A. Ebraheim, and A.C. Jayasuriya, *Investigation of potential injectable polymeric biomaterials for bone regeneration.* Journal of Biomedical Materials Research Part A, 2013(8): p. 2436-2447.

109. Bohner, M. and G. Baroud, *Injectability of calcium phosphate pastes.* Biomaterials, 2005. **26**(13): p. 1553-1563.

110. Tseng, S.-H., T.J. Palathinkal, and N.-H. Tai, *Nondestructive purification of single-walled carbon nanotube rope through a battery-induced ignition and chemical solution approach.* Carbon, 2010. **48**(8): p. 2159-2168.

111. Aryaei, A., A.H. Jayatissa, and A.C. Jayasuriya, *Mechanical and biological properties of chitosan/carbon nanotube nanocomposite films.* Journal of Biomedical Materials Research Part A, 2013.

112. Wang, S.-F., et al., *Preparation and mechanical properties of chitosan/carbon nanotubes composites.* Biomacromolecules, 2005. **6**(6): p. 3067-3072.

113. Spinks, G.M., et al., *Mechanical properties of chitosan/CNT microfibers obtained with improved dispersion.* Sensors and Actuators B: Chemical, 2006. **115**(2): p. 678-684.

114. Badaire, S., et al., *Liquid crystals of DNA-stabilized carbon nanotubes.* Advanced Materials, 2005. **17**(13): p. 1673-1676.

115. Saito, H., R. Tabeta, and K. Ogawa, *High-resolution solid-state carbon-13 NMR study of chitosan and its salts with acids: conformational characterization of polymorphs and helical structures as viewed from the conformation-dependent carbon-13 chemical shifts.* Macromolecules, 1987. **20**(10): p. 2424-2430.

116. Rhim, J.W., et al., *Preparation and characterization of chitosan-based nanocomposite films with antimicrobial activity.* Journal of agricultural and food chemistry, 2006. **54**(16): p. 5814-5822.

117. Govindan, S., et al., *Synthesis and characterization of chitosan–silver nanocomposite.* Applied Nanoscience, 2012. **2**: p. 1-5.

118. Stylianakis, M.M., J.A. Mikroyannidis, and E. Kymakis, *A facile, covalent modification of single-wall carbon nanotubes by thiophene for use in organic photovoltaic cells.* Solar Energy Materials and Solar Cells, 2010. **94**(2): p. 267-274.

119. Ng, S., et al., *Single wall carbon nanotube paper as anode for lithium-ion battery.* Electrochimica acta, 2005. **51**(1): p. 23-28.

120. Wu, Z., et al., *Preparation and characterization of chitosan-grafted multiwalled carbon nanotubes and their electrochemical properties.* Carbon, 2007. **45**(6): p. 1212-1218.

121. Bahr, J.L., et al., *Dissolution of small diameter single-wall carbon nanotubes in organic solvents?* Chemical Communications, 2001(2): p. 193-194.

122. Tang, C., et al., *Wet-grinding assisted ultrasonic dispersion of pristine multi-walled carbon nanotubes (MWCNTs) in chitosan solution.* Colloids and Surfaces B: Biointerfaces, 2011. **86**(1): p. 189-197.

123. Smith, E., G. Dent, and J. Wiley, *Modern Raman spectroscopy: a practical approach*. 2005, England: J. Wiley Hoboken, NJ.

124. Mai, T.T.T., et al., *Chitosan and O-carboxymethyl chitosan modified Fe3O4 for hyperthermic treatment.* Advances in Natural Sciences: Nanoscience and Nanotechnology, 2012. **3**(1): p. 015006.

125. Graupner, R., *Raman spectroscopy of covalently functionalized single-wall carbon nanotubes.* Journal of Raman Spectroscopy, 2007. **38**(6): p. 673-683.

126. Dresselhaus, M., et al., *Raman spectroscopy on isolated single wall carbon nanotubes.* Carbon, 2002. **40**(12): p. 2043-2061.

127. Dresselhaus, M.S., et al., *Raman spectroscopy of carbon nanotubes.* Physics Reports, 2005. **409**(2): p. 47-99.

128. Liu, Y., et al., *Cation-Controlled Aqueous Dispersions of Alginic-Acid-Wrapped Multi-Walled Carbon Nanotubes.* Small, 2006. **2**(7): p. 874-878.

129. Sinani, V.A., et al., *Aqueous dispersions of single-wall and multiwall carbon nanotubes with designed amphiphilic polycations.* Journal of the American Chemical Society, 2005. **127**(10): p. 3463-3472.

130. Jang, J.H., et al., *pH/temperature sensitive chitosan-g-(PA-PEG) aqueous solutions as new thermogelling systems.* Journal of Materials Chemistry, 2011. **21**(14): p. 5484-5491.

131. Baroud, G. and A. Schleyer, *Biomechanics of cement injection in vertebroplasty*. Balloon Kyphoplasty, ed. S. Becker and M. Ogon. 2008, Austria: Springer Wien NewYork. 23.

132. Rungseevijitprapa, W. and R. Bodmeier, *Injectability of biodegradable in situ forming microparticle systems (ISM).* european journal of pharmaceutical sciences, 2009. **36**(4): p. 524-531.

133. Chen, L., et al., *Synthesis and characterization of chitosan–multiwalled carbon nanotubes/hydroxyapatite nanocomposites for bone tissue engineering.* Journal of Materials Science: Materials in Medicine, 2013: p. 1-9.

134. Saha, R. and W.D. Nix, *Effects of the substrate on the determination of thin film mechanical properties by nanoindentation.* Acta Materialia, 2002. **50**(1): p. 23-38.

135. Treacy, M., T. Ebbesen, and J. Gibson, *Exceptionally high Young's modulus observed for individual carbon nanotubes.* Letters to Nature, 1996. **381**: p. 678-680.

136. Czarnecki, J.S., K. Lafdi, and P.A. Tsonis, *A novel approach to control growth, orientation, and shape of human osteoblasts.* Tissue Engineering Part A, 2008. **14**(2): p. 255-265.

137. Brandão, M.M., et al., *Optical tweezers for measuring red blood cell elasticity: application to the study of drug response in sickle cell disease.* European Journal of Haematology, 2003. **70**(4): p. 207-211.

138. Suresh, S., *Mechanical response of human red blood cells in health and disease : Some structure-property-function relationships.* Journal of Materials Research, 2006. **21**(8): p. 1871-1877.

139. Simon, A., et al., *Heterogeneous cell mechanical properties: an atomic force microscopy study.* Cellular and Molecular Biology, 2004. **50**(3): p. 255-266.

140. Lim, C., E. Zhou, and S. Quek, *Mechanical models for living cells—a review.* Journal of Biomechanics, 2006. **39**(2): p. 195-216.

141. Quist, A.P. and R. Lal, *Characterization of Nanoscale Biological Systems: Multimodal Atomic Force Microscopy for Nanoimaging, Nanomechanics, and Biomolecular Interactions*, in *Nanotechnology for Biology and Medicine At the Building Block Level*, A.S. Gabriel and P. Vladimir, Editors. 2012, Springer New York. p. 45-68.

142. Kirmizis, D. and S. Logothetidis, *Atomic force microscopy probing in the measurement of cell mechanics.* International Journal of Nanomedicine, 2010. **5**: p. 137-145.

143. Wu, X., et al., *Application of Atomic Force Microscopy Measurements on Cardiovascular Cells Cardiovascular Development*, X. Peng and M. Antonyak, Editors. 2012, Humana Press. p. 229-244.

144. Hertz, H., *Ueber die Berührung fester elastischer Körper.* Journal für die reine und angewandte Mathematik (Crelle's Journal), 1882. **1882**(92): p. 156-171.

145. Sneddon, I.N., *The relation between load and penetration in the axisymmetric boussinesq problem for a punch of arbitrary profile.* International Journal of Engineering Science, 1965. **3**(1): p. 47-57.

146. Weisenhorn, A.L., et al., *Deformation and height anomaly of soft surfaces studied with an AFM.* Nanotechnology, 1993. **4**(2): p. 106-113.

147. Darling, E.M., et al., *Viscoelastic properties of human mesenchymally-derived stem cells and primary osteoblasts, chondrocytes, and adipocytes.* Journal of Biomechanics, 2008. **41**(2): p. 454-464.

148. Siegel, N., et al., *Human amniotic fluid stem cells: a new perspective.* Amino Acids, 2008. **35**(2): p. 291-293.

149. Rodrigues, M.T., et al., *Amniotic Fluid-Derived Stem Cells as a Cell Source for Bone Tissue Engineering.* Tissue Engineering Part A, 2012.

150. Rodrigues, M.T., et al., *The effect of differentiation stage of amniotic fluid stem cells on bone regeneration.* Biomaterials, 2012. **33**: p. 9.

151. Siegel, N., et al., *Stem cells in amniotic fluid as new tools to study human genetic diseases.* Stem Cell Reviews and Reports, 2007. **3**(4): p. 256-264.

152. Cananzi, M., A. Atala, and P. De Coppi, *Stem cells derived from amniotic fluid: new potentials in regenerative medicine.* Reproductive biomedicine online, 2009. **18**: p. 17-27.

153. Joo, S., et al., *Amniotic fluid-derived stem cells in regenerative medicine research.* Archives of Pharmacal Research, 2012. **35**(2): p. 271-280.

154. Skardal, A., et al., *Substrate Elasticity Controls Cell Proliferation, Surface Marker Expression and Motile Phenotype in Amniotic Fluid-Derived Stem Cells.* Journal of the Mechanical Behavior of Biomedical Materials, 2012.

155. Charras, G.T. and M.A. Horton, *Determination of cellular strains by combined atomic force microscopy and finite element modeling.* Biophysical Journal, 2002. **83**(2): p. 858-879.

156. Charm, G., P. Lehenkari, and M. Horton, *Chapter 8 Biotechnological applications of atomic force microscopy*, in *Methods in Cell Biology*, H.J.K.H. Bhanu P. Jena, Editor. 2002, Academic Press. p. 171-191.

157. Fung, C.K.M., et al., *Investigation of human keratinocyte cell adhesion using atomic force microscopy.* Nanomedicine: Nanotechnology, Biology and Medicine, 2010. **6**(1): p. 191-200.

158. Costa, K.D., *Imaging and probing cell mechanical properties with the atomic force microscope*, in *Methods in Molecular Medicine*, D.J.M.B.T. Taatjes, Editor. 2006. p. 331-361.

159. Vié, V., et al., *Tapping-mode atomic force microscopy on intact cells: optimal adjustment of tapping conditions by using the deflection signal.* Ultramicroscopy, 2000. **82**(1–4): p. 279-288.

160. Costa, K.D., A.J. Sim, and F.C.P. Yin, *Non-Hertzian Approach to Analyzing Mechanical Properties of Endothelial Cells Probed by Atomic Force Microscopy.* Journal of Biomechanical Engineering, 2006. **128**(2): p. 176-184.

161. Rotsch, C. and M. Radmacher, *Drug-Induced Changes of Cytoskeletal Structure and Mechanics in Fibroblasts: An Atomic Force Microscopy Study.* Biophysical Journal, 2000. **78**(1): p. 520-535.

162. Zhu, Y., et al., *Determination of mechanical properties of soft tissue scaffolds by atomic force microscopy nanoindentation.* Journal of Biomechanics, 2011. **44**(13): p. 2356-2361.

163. Simon, A. and M.C. Durrieu, *Strategies and results of atomic force microscopy in the study of cellular adhesion.* Micron, 2006. **37**(1): p. 1-13.

164. Jena, B.P. and J.K.H. Hörber, *Atomic force microscopy in cell biology*. Vol. 68. 2002: Academic Pr.

165. Basson, C.T., et al., *Differential modulation of vascular cell integrin and extracellular matrix expression in vitro by TGF-B1 correlates with reciprocal effects on cell migration+.* Journal of cellular physiology, 1992. **153**(1): p. 118-128.

166. Bourdoulous, S., et al., *Fibronectin Matrix Regulates Activation of RHO and CDC42 GTPases and Cell Cycle Progression.* The Journal of Cell Biology, 1998. **143**(1): p. 267-276.

167. Favre, M., et al., *Parallel AFM imaging and force spectroscopy using two-dimensional probe arrays for applications in cell biology.* Journal of Molecular Recognition, 2011. **24**(3): p. 446-452.

168. Simon, A., et al., *Characterization of dynamic cellular adhesion of osteoblasts using atomic force microscopy.* Cytometry A, 2003. **54**(1): p. 36-47.

169. Chen, Q., et al., *AFM Studies of Cellular Mechanics during Osteogenic Differentiation of Human Amniotic Fluid-derived Stem Cells.* Analytical Sciences, 2010. **26**(10): p. 1033-1037.

170. Titushkin, I. and M. Cho, *Modulation of Cellular Mechanics during Osteogenic Differentiation of Human Mesenchymal Stem Cells.* Biophysical Journal, 2007. **93**(10): p. 3693-3702.

171. Kelly, G.M., et al., *Bone cell elasticity and morphology changes during the cell cycle.* Journal of Biomechanics, 2011. **44**(8): p. 1484-1490.

172. Costa, K.D., *Single-cell elastography: probing for disease with the atomic force microscope.* Disease markers, 2003. **19**(2-3): p. 139-54.

173. Kim, J., et al., *Human amniotic fluid-derived stem cells have characteristics of multipotent stem cells.* Cell Proliferation, 2007. **40**(1): p. 75-90.

174. Kolambkar, Y.M., et al., *Colonization and osteogenic differentiation of different stem cell sources on electrospun nanofiber meshes.* Tissue Engineering Part A, 2010. **16**(10): p. 3219-3230.

175. Haga, H., et al., *Elasticity mapping of living fibroblasts by AFM and immunofluorescence observation of the cytoskeleton.* Ultramicroscopy, 2000. **82**(1–4): p. 253-258.

176. Goldsbury, C.S., S. Scheuring, and L. Kreplak, *Introduction to Atomic Force Microscopy (AFM) in Biology*, in *Current Protocols in Protein Science*. 2001, John Wiley & Sons, Inc.

177. Zitzler, L., S. Herminghaus, and F. Mugele, *Capillary forces in tapping mode atomic force microscopy.* Physical Review B, 2002. **66**(15): p. 155436.

178. Jung, Y.G., et al., *Evaluation of elastic modulus and hardness of thin films by nanoindentation.* Journal of Materials Research, 2004. **19**(10): p. 3076-3080

179. Mathur, A.B., et al., *Endothelial, cardiac muscle and skeletal muscle exhibit different viscous and elastic properties as determined by atomic force microscopy.* Journal of Biomechanics, 2001. **34**(12): p. 1545-1553.

180. Sirghi, L., et al., *Probing elasticity and adhesion of live cells by atomic force microscopy indentation.* European Biophysics Journal, 2008. **37**(6): p. 935-945.

181. Agnihotri, A. and C.A. Siedlecki, *Adhesion mode atomic force microscopy study of dual component protein films.* Ultramicroscopy, 2005. **102**(4): p. 257-268.

182. Sen, S., S. Subramanian, and D.E. Discher, *Indentation and Adhesive Probing of a Cell Membrane with AFM: Theoretical Model and Experiments.* Biophysical Journal, 2005. **89**(5): p. 3203-3213.

183. Charras, G.T., P.P. Lehenkari, and M.A. Horton, *Atomic force microscopy can be used to mechanically stimulate osteoblasts and evaluate cellular strain distributions.* Ultramicroscopy, 2001. **86**(1-2): p. 85-95.

184. Svaldo Lanero, T., et al., *Mechanical properties of single living cells encapsulated in polyelectrolyte matrixes.* Journal of Biotechnology, 2006. **124**(4): p. 723-731.

185. Kagiwada, H., et al., *The mechanical properties of a cell, as determined by its actin cytoskeleton, are important for nanoneedle insertion into a living cell.* Cytoskeleton, 2010. **67**(8): p. 496-503.

186. Yourek, G., M.A. Hussain, and J.J. Mao, *Cytoskeletal changes of mesenchymal stem cells during differentiation.* ASAIO Journal, 2007. **53**(2): p. 219-228.

187. Collinsworth, A.M., et al., *Apparent elastic modulus and hysteresis of skeletal muscle cells throughout differentiation.* American Journal of Physiology-Cell Physiology, 2002. **283**(4): p. C1219-C1227.

188. Takai, E., et al., *Osteoblast elastic modulus measured by atomic force microscopy is substrate dependent.* Annals of Biomedical Engineering, 2005. **33**(7): p. 963-971.

189. Darling, E., S. Zauscher, and F. Guilak, *Viscoelastic properties of zonal articular chondrocytes measured by atomic force microscopy.* Osteoarthritis and Cartilage, 2006. **14**(6): p. 571-579.

190. Ruiz, J.P., et al., *The effect of nicotine on the mechanical properties of mesenchymal stem cells.* Cell Health and Cytoskeleton, 2012. **4**: p. 29-35.

191. Nikkhah, M., et al., *Evaluation of the influence of growth medium composition on cell elasticity.* Journal of Biomechanics, 2011. **44**(4): p. 762-766.

192. Darling, E.M., et al., *A thin-layer model for viscoelastic, stress-relaxation testing of cells using atomic force microscopy: do cell properties reflect metastatic potential?* Biophysical Journal, 2007. **92**(5): p. 1784-1791.

193. Pogoda, K., et al., *Depth-sensing analysis of cytoskeleton organization based on AFM data.* European Biophysics Journal, 2012: p. 1-9.

194. Lekka, M., et al., *Cancer cell recognition–Mechanical phenotype.* Micron, 2012.

195. Ng, L., et al., *Nanomechanical properties of individual chondrocytes and their developing growth factor-stimulated pericellular matrix.* Journal of Biomechanics, 2007. **40**(5): p. 1011-1023.

196. Rao, C.N.R., et al., *Graphene: The New Two-Dimensional Nanomaterial.* Angewandte Chemie, International Edition, 2009. **48**(42): p. 7752-7777.

197. Geim, A.K., *Graphene: status and prospects.* Science, 2009. **324**(5934): p. 1530-1534.

198. Zhu, Y., et al., *Graphene and graphene oxide: synthesis, properties, and applications.* Advanced Materials, 2010. **22**(35): p. 3906-3924.

199. Schedin, F., et al., *Detection of individual gas molecules adsorbed on graphene.* Nature materials, 2007. **6**(9): p. 652-655.

200. Li, X., et al., *Large-area synthesis of high-quality and uniform graphene films on copper foils.* Science, 2009. **324**(5932): p. 1312-1314.

201. Shen, H., et al., *Biomedical applications of graphene.* Theranostics, 2012. **2**(3): p. 283.

202. Mohanty, N. and V. Berry, *Graphene-based single-bacterium resolution biodevice and DNA transistor: interfacing graphene derivatives with nanoscale and microscale biocomponents.* Nano Letters, 2008. **8**(12): p. 4469-4476.

203. Feng, L. and Z. Liu, *Graphene in biomedicine: opportunities and challenges.* Nanomedicine, 2011. **6**(2): p. 317-324.

204. Wang, Y., et al., *Graphene and graphene oxide: biofunctionalization and applications in biotechnology.* Trends in biotechnology, 2011. **29**(5): p. 205-212.

205. Kim, H., et al., *Graphene Oxide–Polyethylenimine Nanoconstruct as a Gene Delivery Vector and Bioimaging Tool.* Bioconjugate Chemistry, 2011. **22**(12): p. 2558-2567.

206. He, S., et al., *A graphene nanoprobe for rapid, sensitive, and multicolor fluorescent DNA analysis.* Advanced Functional Materials, 2010. **20**(3): p. 453-459.

207. Akhavan, O. and E. Ghaderi, *Toxicity of graphene and graphene oxide nanowalls against bacteria.* ACS Nano, 2010. **4**(10): p. 5731-5736.

208. Yang, K., et al., *Behavior and Toxicity of Graphene and Its Functionalized Derivatives in Biological Systems.* Small, 2013. **9**: p. 1492–1503.

209. Kalbacova, M., et al., *Graphene substrates promote adherence of human osteoblasts and mesenchymal stromal cells.* Carbon, 2010. **48**(15): p. 4323-4329.

210. Yang, M., J. Yao, and Y. Duan, *Graphene and its derivatives for cell biotechnology.* Analyst, 2012. **138**: p. 72-86.

211. Park, S.Y., et al., *Enhanced differentiation of human neural stem cells into neurons on graphene.* Advanced Materials, 2011. **23**(36): p. H263-H267.

212. Akhavan, O., et al., *Genotoxicity of graphene nanoribbons in human mesenchymal stem cells.* Carbon, 2013. **54**: p. 419-431.

213. Chang, Y., et al., *In vitro toxicity evaluation of graphene oxide on A549 cells.* Toxicology letters, 2011. **200**(3): p. 201-210.

214. Wang, K., et al., *Biocompatibility of graphene oxide.* Nanoscale Res. Lett, 2011. **6**(8): p. 1-8.

215. Kalbacova, M., A. Broz, and M. Kalbac, *Influence of the fetal bovine serum proteins on the growth of human osteoblast cells on graphene.* Journal of Biomedical Materials Research, Part A, 2012. **100A**: p. 3001-3007.

216. Verdanova, M., et al., *Influence of oxygen and hydrogen treated graphene on cell adhesion in the presence or absence of fetal bovine serum.* Physica Status Solidi B, 2012. **249**(12): p. 2503-2506.

217. Ryoo, S.R., et al., *Behaviors of NIH-3T3 fibroblasts on graphene/carbon nanotubes: proliferation, focal adhesion, and gene transfection studies.* ACS Nano, 2010. **4**(11): p. 6587-6598.

218. Lim, H.N., et al., *Fabrication and characterization of graphene hydrogel via hydrothermal approach as a scaffold for preliminary study of cell growth.* International journal of nanomedicine, 2011. **6**: p. 1817-1823.

219. Nayak, T.R., et al., *Graphene for controlled and accelerated osteogenic differentiation of human mesenchymal stem cells.* ACS Nano, 2011. **5**(6): p. 4670-4678.

220. Seif-Naraghi, S.B. and K.L. Christman, *Tissue Engineering and the Role of Biomaterial Scaffolds*, in *Resident Stem Cells and Regenerative Therapy*. 2012. p. 43.

221. Sidorov, A.N., et al., *A surface-enhanced Raman spectroscopy study of thin graphene sheets functionalized with gold and silver nanostructures by seed-mediated growth.* Carbon, 2012. **50**(2): p. 699-705.

222. Gautam, M. and A.H. Jayatissa, *Detection of organic vapors by graphene films functionalized with metallic nanoparticles.* Journal of Applied Physics, 2012. **112**(11): p. 114326.

223. Gautam, M. and A.H. Jayatissa, *Adsorption kinetics of ammonia sensing by graphene films decorated with platinum nanoparticles.* Journal of Applied Physics, 2012. **111**(9): p. 094317.

224. Ferrari, A., et al., *Raman spectrum of graphene and graphene layers.* Physical Review Letters, 2006. **97**(18): p. 187401.

225. Suk, J.W., et al., *Transfer of CVD-grown monolayer graphene onto arbitrary substrates.* ACS Nano, 2011. **5**(9): p. 6916-6924.

226. Novoselov, K., et al., *Two-dimensional gas of massless Dirac fermions in graphene.* Nature, 2005. **438**(7065): p. 197-200.

227. Reina, A., et al., *Large area, few-layer graphene films on arbitrary substrates by chemical vapor deposition.* Nano Letters, 2008. **9**(1): p. 30-35.

228. Müller, R., et al., *Surface engineering of stainless steel materials by covalent collagen immobilization to improve implant biocompatibility.* Biomaterials, 2005. **26**(34): p. 6962-6972.

229. Ponsonnet, L., et al., *Relationship between surface properties (roughness, wettability) of titanium and titanium alloys and cell behaviour.* Materials Science and Engineering: C, 2003. **23**(4): p. 551-560.

230. Deligianni, D., et al., *Effect of surface roughness of the titanium alloy Ti–6Al–4V on human bone marrow cell response and on protein adsorption.* Biomaterials, 2001. **22**(11): p. 1241-1251.

231. Discher, D.E., P. Janmey, and Y. Wang, *Tissue cells feel and respond to the stiffness of their substrate.* Science, 2005. **310**(5751): p. 1139-1143.

232. Engler, A.J., et al., *Matrix elasticity directs stem cell lineage specification.* Cell, 2006. **126**(4): p. 677-689.

233. Palchesko, R.N., et al., *Development of polydimethylsiloxane substrates with tunable elastic modulus to study cell mechanobiology in muscle and nerve.* PloS one, 2012. **7**(12): p. e51499.

234. Shi, X., et al., *Regulating Cellular Behavior on Few-Layer Reduced Graphene Oxide Films with Well Controlled Reduction States.* Advanced Functional Materials, 2012. **22**: p. 751–759.

235. Akasaka, T., et al., *Thin films of single-walled carbon nanotubes promote human osteoblastic cells (Saos-2) proliferation in low serum concentrations.* Materials Science and Engineering: C, 2010. **30**(3): p. 391-399.

236. Yamaguchi, T., Y. Yamamoto, and H. Liu, *Computational mechanical model studies on the spontaneous emergent morphogenesis of the cultured endothelial cells.* Journal of Biomechanics, 2000. **33**(1): p. 115-126.

237. Chakraborty, A., et al., *Effects of biaxial oscillatory shear stress on endothelial cell proliferation and morphology.* Biotechnology and bioengineering, 2012. **109**(3): p. 695-707.

238. Maul, T.M., et al., *Mechanical stimuli differentially control stem cell behavior: morphology, proliferation, and differentiation.* Biomechanics and modeling in mechanobiology, 2011. **10**(6): p. 939-953.

239. Inoguchi, H., et al., *The effect of gradually graded shear stress on the morphological integrity of a huvec-seeded compliant small-diameter vascular graft.* Biomaterials, 2007. **28**(3): p. 486-495.

240. Chotard-Ghodsnia, R., et al., *Morphological analysis of tumor cell/endothelial cell interactions under shear flow.* Journal of Biomechanics, 2007. **40**(2): p. 335-344.

241. Sato, M. and T. Ohashi, *Biorheological views of endothelial cell responses to mechanical stimuli.* Biorheology, 2005. **42**(6): p. 421-441.

242. Obi, S., et al., *Fluid shear stress induces differentiation of circulating phenotype endothelial progenitor cells.* American Journal of Physiology-Cell Physiology, 2012. **303**(6): p. C595-C606.

243. Dardik, A., et al., *Differential effects of orbital and laminar shear stress on endothelial cells.* Journal of vascular surgery, 2005. **41**(5): p. 869-880.

244. Chollet, C., et al., *Impact of Peptide Micropatterning on Endothelial Cell Actin Remodeling for Cell Alignment under Shear Stress.* Macromolecular bioscience, 2012. **12**(12): p. 1648-1659.

245. Berson, R.E., M.R. Purcell, and M.K. Sharp, *Computationally determined shear on cells grown in orbiting culture dishes*, in *Oxygen Transport to Tissue XXIX*. 2008, Springer. p. 189-198.

246. Yourek, G., et al., *Shear stress induces osteogenic differentiation of human mesenchymal stem cells.* Regenerative medicine, 2010. **5**(5): p. 713-724.

247. Ando, J. and K. Yamamoto, *Effects of shear stress and stretch on endothelial function.* Antioxidants & redox signaling, 2011. **15**(5): p. 1389-1403.

248. Ley, K., et al., *Shear-dependent inhibition of granulocyte adhesion to cultured endothelium by dextran sulfate.* Blood, 1989. **73**(5): p. 1324-1330.

Appendix A

Nowadays, the common method which is used to find elastic modulus from nanoindentation is based on the Oliver-Pharr theory [68]. This method is widely used by scientists.

Important quantities in this method are as follows: The maximum indentation depth $h_{\max}$ includes elastic and plastic deformation. The depth at which the applied force becomes zero upon unloading is called h_f, the depth h_c is the contact depth at which the cross sectional area A_c is taken to calculate hardness and indentation modulus. The nanohardness of the sample H_N is determined using the formula:

$$H_N = \frac{F_{\max}}{A_c(h_c)}, \tag{A.1}$$

Where $F_{\max}$ is the maximum applied load and A_c is the cross sectional area corresponding to the depth h_c. The determination of the contact depth h_c is given by:

$$h_c = h_{\max} - 0.75\frac{F_{\max}}{S}, \tag{A.2}$$

Where S is the contact stiffness:

$$S = \frac{dF}{dh} \tag{A.3}$$

with $\frac{dF}{dh}$ being the slope of the unloading curve at the initial point of unloading. The reduced Young's indentation modulus E_r is a measure of the elastic properties of the tip sample system and can be calculated from the load-depth curves according to the formula:

$$E_r = \frac{1}{2}\sqrt{\frac{\pi}{A_c}}S \tag{A.4}$$

For elastically deformable indentors, the reduced modulus E_r can be generalized and is defined as:

$$\frac{1}{E_r} = \frac{1-\upsilon_s^2}{E_s} + \frac{1-\upsilon_t^2}{E_t}, \tag{A.5}$$

Where E_s and υ_s are the indentation modulus and Poisson ratio of the sample, E_t and υ_t are the indentation modulus and Poisson ratio of the indenter tip. Since E_t is much higher than E_s the value of E_r will hardly differ from E_s.

For the indents at nano scale, the remaining area is difficult to be measured with the traditional optical microscopy because of a resolution that is too low. According to the probe geometry, the area as a function of depth can be expressed as:

$$A_c(h_c) = 2.62h_c^2 \tag{A.6}$$

List of Journal publications derived from this dissertation:

1. **A. Aryaei,** Ahalapitiya H. Jayatissa, A. Champa. Jayasuriya, "Mechanical and biological properties of chitosan/carbon nanotube nanocomposite films", Journal of Biomedical Materials Research - Part A. (In Press)

2. **A. Aryaei,** Ahalapitiya H. Jayatissa, A. Champa Jayasuriya, "The effect of graphene substrate on osteoblast adhesion and proliferation", Journal of Biomedical materials Research - Part A. (In Press)

3. A. Champa Jayasuriya, **A. Aryaei**, Ahalapitiya H. Jayatissa, "ZnO nanoparticles induced effects on nanomechanical behavior and cell viability of chitosan films", Journal of Material Science and Engineering C 2013, 33: 3688-3696.

4. **A. Aryaei,** A. Champa Jayasuriya, "Mechanical properties of human amniotic fluid stem cells using nanoindentation", Journal of Biomechanics 2013, 46: 1524–1530.

5. **A. Aryaei,** Ahalapitiya H. Jayatissa, A. Champa Jayasuriya, "Nano and micro mechanical properties of uncross-linked and cross-linked chitosan films", Journal of the Mechanical Behavior of Biomedical Materials 2012, 5: 82–89.

List of conference presentations and proceedings:

1. **A. Aryaei,** Ahalapitiya H. Jayatissa, A. Champa Jayasuriya, Osteoblast function on carbon based nanoparticle substrates, Second International Conference on Advanced Materials, Energy and Environments, August 8-9, 2013, Yokohama, Japan

2. **A. Aryaei,** Ahalapitiya H. Jayatissa, M. Gautam, A. Champa Jayasuriya, Graphene coated substrates for cell attachment and proliferation, Society of Biomaterials meeting, April 10-13, 2013, Boston, MA, USA.

3. **A. Aryaei,** Ahalapitiya H. Jayatissa, A. Champa Jayasuriya, Methods to find the nanomechanical properties of biological and biomaterial samples, The First International Conference on Materials, Energy and Environment, May 9-11, 2012, Toledo, OH, USA.

4. **A. Aryaei,** A. Champa Jayasuriya, Study of effect of Zinc Oxide nanoparticles on mechanical properties of chitosan matrices using AFM, TERMIS annual meeting, December 11-14, 2011, Houston, TX, USA.

5. **A. Aryaei,** A. Champa Jayasuriya, Methods to estimate cell elastic modulus, ASME-IMECE annual meeting, November 21-25, 2013, San Diego, CA, USA.